Characterization of Ultra-Deeply Buried Middle Triassic Leikoupo Marine Carbonate Petroleum System (!) in the Western Sichuan Depression, China

Tengjiao Sun[a,d,i], Xiaoping Luo[a,i*], Wentian Mi[b,f,i*], Adam Woods[b], Domenico Chiarella[c], Hairuo Qing[a,d,i*], Yongsheng Ma[a,e,i], Xueling Kou[e], Zhongmin Shen[a,i], Guosheng Xu[a,i], Haifeng Yuan[a,i], Jiaju Liang[a,i], Fanghao Xu[a,d,i], Hao Wang[a,d,i], Xiaoxing Gong[a,g,i], Jian Luo[a,c,i], Tingfu Jin[a,h,i], Xiaowei Lv[a,e,i]

[a] College of Energy Resource, Chengdu University of Technology, Chengdu, Sichuan, 610059, China;

[b] Department of Geological Sciences, California State University, Fullerton, Ca 92834-6850, USA;

[c] Clastic Sedimentology Investigation (CSI), Department of Earth Sciences, Royal Holloway University of London, Egham, Surrey, TW200EX, UK;

[d] Department of Geology, University of Regina, Regina, Saskatchewan, S4S0A2, Canada;

[e] China Exploration Company, SINOPEC, Sichuan, 610041, China;

[f] School of Mines, Inner Mongolia University of Technology, Hohhot, 010051, China;

[g] Geologic Exploration & Development Research Institute, Chuan Qing Drilling Co., Ltd., CNPC, Chengdu, 610051, China;

[h] Guizhou University of Engineering Science, Bijie, Guizhou, 551700, China;

[i] Institute of Sedimentary Geology & State Key Laboratory of Oil and Gas Reservoir Geology and Exploration, Chengdu, Sichuan, 610059, China.

[*]Corresponding authors e-mail: lxpcdut@163.com; miwentian1982@163.com; Hairuo.Qing@gmail.com

Abstract

Ultra-deeply buried (>5000 m) marine carbonate reservoirs have gradually become important exploration targets. This research focuses on providing an understanding of the basic elements of the ultra-deeply buried Middle Triassic Leikoupo marine carbonate petroleum system within the Western Sichuan Depression, China. Comprehensive analyses of organic geochemistry, natural gas, and C–H–He–Ne–Ar isotope compositions suggest that the reservoir is charged with compound gases from four source rock units including the Permian Longtan, Middle Triassic Leikoupo, Late Triassic Maantang and Xiaotangzi formations. Approximately a 50-m thick outcrop and 100-m length of drilling cores were examined in detail, and 108 samples were collected from six different exploration wells in order to conduct petrographic and petrophysical analyses. Thin-section and scanning electron microscope (SEM) observations, helium porosity and permeability measurements, mercury injection capillary pressure (MICP) analysis, and wire-line logging (5,500–6,900 m) indicate that the reservoir lithologies include argillaceous algal

limestones, dolograinstones, crystalline dolostones, and microbially-derived stromatolitic and thrombolitic dolostones. Reservoir properties exhibit extreme heterogeneity due to different paleogeographic environmental controls and mutual interactions between constructive (e.g., epigenetic paleo-karstification, burial dissolution, structural movement, pressure-solution and dolomitization) and destructive (e.g., physical/chemical compaction, cementation, infilling, recrystallization, and replacement) diagenetic processes. An unconformity-related epigenetic karstification zone was identified in the uppermost fourth member of the Leikoupo Formation, which has developed secondary solution-enhanced pores, vugs, and holes that resulted in higher porosity (1.8–14.2%) and permeability (0.2–7.7 mD). The homogeneity and tightness of the reservoir increases with depth below the unconformity, and it is characterized by primary intergranular and intracrystalline pores, solution pores, fractures, stylolites, and micropores with a lower helium porosity (0.6–4.1%) and permeability (0.003–125.2 mD). Regional seals consist of the Late Triassic Xujiahe Formation, comprised of ~300 m of mudstones that are overlain by ~5,000-m thick of Jurassic to Quaternary continental argillaceous overburden rocks. Effective traps are dominated by a combination of structural-stratigraphic types. Paleo-reservoir crude oil cracking, wet-gases, and dry-gases from three successive hydrocarbon generation processes supplied the sufficient hydrocarbon resources. The homogenization temperatures of the hydrocarbon-associated aqueous fluid inclusions range from 98–130 °C and 130–171 °C, which suggests hydrocarbon charging occurred between 220–170 Ma and 130–90 Ma, respectively. One-dimensional basin evolution models combined with structural geologic and seismic profiles across wells PZ1-XQS1-CK1-XCS1-TS1 show that hydrocarbon migration and entrapment mainly occurred via the unconformity and interconnected fault-fracture networks with migration and charging driven by formation overpressure, abnormal fluid flow pressure, and buoyancy forces during the Indosinian and Yanshanian orogenies, with experiencing additional transformation occurring during the Himalayan orogeny. The predicted estimated reserves reached ~300 × 10^9 m^3. The results provide excellent scientific implications for similar sedimentary basin studies, it is believed that abundant analogous deeply buried marine carbonate hydrocarbon resources yet to be discovered in China and elsewhere worldwide in the near future.

Keywords: Ultra-deeply buried, Middle Triassic Leikoupo Formation, Marine carbonate, Petroleum system, Western Sichuan Depression, China

1 Introduction

Marine carbonates are among the most important hydrocarbon reservoirs and contain up to 60% of the world's oil and gas reserves (Bagrintseva, 2015). Many giant and supergiant carbonate reservoirs likely have production lifetimes greater than 50 years, and most of the world's larger commercial oil or natural gas fields are located in the Middle East, North America, Europe, and Asia regions (Garland et al., 2012; Katz and Everett, 2016; Wang et al., 2017; Li et al., 2018; Xu et al., 2019; Medici et al., 2021; Pontes et al., 2021). The availability and cost of crude oil and natural gases (as well as other fossil fuels) for use as both fuel and as a raw material for manufacturing are important factors for determining future exploration and development (Whiticar, 1994; Neilson et al., 1998; Katz and Ehret, 2000; Ehrenberg and Nadeau and, 2005; Magoon et al., 2005; Peters et al., 2006). Relative to shallower (usual depth of 0–4,500 m) petroleum reservoirs or systems, advancements in petroleum exploration theories and modern techniques have enabled improved exploration and drilling operations for highly buried targets (Liu and Katz, 2016; Hao, 2022). Interest in these deep and/or ultra-deeply buried petroleum systems at depth standards of 4,500–5,000 m and > 5,000 m, respectively is growing (Magoon and Dow, 1994; Mancini et al., 2008; Akinlua, 2012; Garland et al., 2012; Li et al., 2018; Zhu et al., 2018).

Owing to its tectono-sedimentary environment and excellent oil/gas potential, the Sichuan Basin, together with the Ordos and Tarim basins, are considered to be one of the most prospected hydrocarbon exploration areas in China (Zhao et al., 1996; Guo et al., 2014; Katz and Everett, 2016; Liu et al., 2016b; Liu et al., 2017; Wu et al., 2017a; Craig et al., 2018) (Fig. 1A). Natural gas from the Sichuan Basin in China has been utilized by humans as far back as the ancient pre-Qin to Han dynasty (approximately BC 250~AD 220); as such, it is likely among the earliest regions in the world to have provided such resources (Fuller, 1919; Liu, 1981). To date, at least seven developed petroleum systems have been identified within gas-bearing stratigraphic interval combinations of the basin, from the Sinian/Edicarian (Sn) to the Quaternary (Q) (Ma et al., 2007; Zhang et al., 2007; Hao et al., 2008; Zhao et al., 2011; Feng et al., 2016; Li et al., 2019; Liu et al., 2021a) (Figs. 1B, 2, 3).

Hydrocarbons in the Western Sichuan Depression and other areas have been continuously and incrementally exploited since the 1940s, and resulting in the discovery of large-scale reservoirs such as those within: (i) the Late Triassic Xujiahe Formation (T_3x) to Jurassic (J) continental siliciclastic rocks, which includes unconventional petroleum systems such as tight sandstone or shale-based reservoirs with proven gas reserve volumes of 500~700 × 10^9 m^3 within the Xinchang, Hexinchang, Dayi, Pingluoba and Gongxi gas fields (Yang and Zhu, 2013; Katz and Lin, 2014; Katz and Arango, 2018; Ma et al., 2019; Guo et al., 2021; Zhu et al., 2021); and (ii) marine carbonate petroleum systems of the Puguang (with a proven original in-place gas reserve volume of 350 × 10^9 m^3), the giant Yuanba Gas Field (estimated gas reserve volume of ~500 × 10^9 m^3), Xinchang (proven gas reserve volume of 121.12 × 10^9 m^3), the Zhongba Gas Fields (proven gas reserve volume of 8.630 × 10^9 m^3), and the Hewanchang gas-bearing structures, which possess significant amounts of accumulated commercial hydrocarbons is also present (Ma et al., 2007; Huang et al., 2011; Xu et al., 2013; Li et al., 2016; Wu et al., 2017a; Ma et al., 2019; Guo, 2020; Cai et al., 2021;). Currently, more than 38 exploration wells have reached the Middle Triassic Leikoupo Formation (T_2l), providing fundamental subsurface information about the geology of the Western Sichuan Depression and associated hydrocarbons (Wang et al., 2008; Zeng et al., 2008; Chen et al., 2013; Ning et al., 2015; Tian et al., 2018; Wang et al., 2018) (Fig. 2). It is important, however, to gain a better understanding of the component units of the Western Sichuan Depression, specifically the core region occupied by the marine carbonates of the Middle Triassic Leikoupo

Formation (T_2l), as hydrocarbon production beneath the Longmenshan Plateau has recently expanded and become an increasingly important area for academic research and commercial gas exploration and exploitation (Lash and Engelder, 2011; Xu et al., 2011, 2013; Li et al., 2017; Wu et al., 2017b; Ghalayini et al., 2018; Zhu et al., 2018) (Fig. 1 and Fig. 2).

Numerous studies have extensively discussed the regional geology, stratigraphy, lithology, tectonic evolution, paleo-sedimentary environments, paleo-geography, geochemistry, and the elements of the petroleum systems of the Western Sichuan Depression (Hu et al., 2008; Hakim et al., 2012; Xu et al., 2015; Mani, 2016; Sachse et al., 2016; Sun et al., 2017; Wang et al., 2022) (Fig. 1B). The Sichuan Basin was dominated by marine sediments from the Sinian (≈Edicarian) to the Middle Triassic. Subsequently, the paleo-depositional environment transitioned from a marine carbonates evaporative-restricted platform to fluvial-lacustrine continental facies in the Middle–Late Triassic (Ruppel and Ward, 2013; Xu et al., 2015; Feng et al., 2016; Feng et al., 2017) (Figs. 3, 4, 5). Research studies performed by Xu et al. (2011, 2013), Xie et al. (2015) and Sun et al. (2020) have suggested that the deeply buried natural gases comprising higher methane and hydrogen mixed gas components, which are mainly thermogenic, originated from multiple sets of potential source rocks from the Permian to Middle–Late Triassic strata. Additionally, Song et al. (2013) and Sun (2020) reported three sets of marine source rocks that could produce hydrocarbons based on the types and distributions of effective source rocks and the geographical extent of the petroleum systems, including: (i) dark algal-rich dolomites of the Middle

Triassic Leikoupo Formation; (ii) gray, muddy limestones of the Late Triassic Maantang Formation; and, (iii) dark mudstones and shales of the Late Triassic Xiaotangzi Formation (Bei and Yang, 1980; Whiticar et al., 1994; Shen et al., 2008; Feng et al., 2013; Qin et al., 2016; Su et al., 2022). The period between the 1940s and the 1980s witnessed the discovery of these above mentioned highly productive gas reservoirs that resulted from the fracture-dissolution of pore spaces (Feng et al., 2013; Tang et al., 2013; Hackley and Karlsen, 2014; Meng et al., 2015; Tian et al., 2018). These reservoirs are specifically located in the Middle Triassic Leikoupo Formation （T_2l） and a portion of the Late Triassic Maantang Formation (T_3m), and they consist of oolitic dolomites, algal dolomites, dolograinstones, and limestones deposited within a platform-margin environment (Xu et al., 2011, 2013; Chen et al., 2018). Feng et al. (2015, 2016, 2017) provided petrographic analysis of the deeply buried hydrothermal dolomite reservoir, clarified the source and migration patterns of the hydrothermal fluids, and described the replacive dolomitization mechanism within the Precambrian and Middle Permian Qixia Formation dolomite reservoirs of the neighboring Moxi gas field, which is located in the center of the Sichuan Basin (Fig. 1). Additionally, Jiang et al. (2018a, b, c, 2019) reported the multiphase dolomitization and associated diagenesis, and its impact on the microbialite-dominated reservoir found within the Middle Triassic Leikoupo Formation in the Longgang and Pengzhou gas fields areas.

The Western Sichuan Depression is structurally complex and hosts a convoluted network of traps and faults. The dominant structures in the region are oriented in a

NE–SW direction and have been identified as being primarily structural and stratigraphic traps, or a combination of both (Li et al., 2009; Meng et al., 2015; Osorno and Rangel, 2015; Sun et al., 2017) (Figs. 1, 2, 3, and 4). The multistage deep-seated faults and fractures were formed as the result of local tectonics, and they probably served as migration pathways for oil and gas, as well as for the flow of diagenetic fluids (Jiang et al., 2018a, b, c; Chi et al., 2022). The widely distributed Late Triassic Xujiahe (T_3x) Formation to Quaternary (Q) rock is comprised of continental argillaceous sediments that are more than 5,000 m thick, and they effectively act as seals and overburden rocks for the natural gas reservoirs (Zhang et al., 2007; Xu et al., 2013; Meng et al., 2015; He et al., 2017) (Fig. 3).

However, although exploration activities and investigations of the hydrocarbon potential of the Western Sichuan Depression have been ongoing for many years, limited comprehensive studies are available on the full petroleum system components and formation mechanisms of the ultra-deeply buried marine carbonates of the Middle Triassic Leikoupo Formation (T_2l) (note: the philosophical concept of petroleum system used in this study was defined by the work of Magoon et al. (1994, 2001, 2005), Peters et al. (2006), Hill et al. (2007), Katz et al. (2016)). Therefore, the current research focuses on improving our understanding of a completely ultra-deeply buried marine carbonate petroleum system by providing multidisciplinary integrated information about the organic geochemical, petrophysical, and geophysical elements that were essential for hydrocarbon accumulation in the Western Sichuan Depression. Specifically, this study has four fundamental aims: (i) to systematically determine the origin of hydrocarbon gases, summarize the geochemical characteristics of the effective source rocks, and resolve the hydrocarbon generation potential; (ii) to evaluate the petrophysical quality and quantity of the carbonate reservoirs, establish the evolution of diagenetic processes, and determine the main controlling factors; (iii) to determine the efficiency of the seals, overburden rocks, and traps; and (iv) to construct a general evolutionary history model of the Western Sichuan Depression, including hydrocarbon generation, migration, charging and accumulation processes. Meeting such aims will provide a detailed understanding of the Middle Triassic Leikoupo marine carbonate petroleum system, which could provide a fresh perspective for future evaluation and exploration of the hydrocarbon potential in the study area, or in sedimentary basins with similar geological conditions that are found throughout the world.

2 Geological Background

2.1 Geological composition and tectonic evolution

The intracratonic Sichuan Basin is located on the western margin of the southwest China block (Lu, 1989; Tian, 1990; Feng et al., 2016; Feng et al., 2017; Zhang et al., 2018; Liu et al., 2021a) (Fig. 1A). The Western Sichuan Depression is situated in the western part of the Sichuan Basin (102°–106° E, 28°40′–32°40′ N), and covers approximately area of 400,000 km^2 (Li et al., 2009; Hu et al., 2012; Zhu et al., 2015; Jiang et al., 2018a; Liu et al., 2021b) (Fig. 1A and B). The Western Sichuan Depression belongs to the frontal thrust–fold belt of the Sichuan Basin foreland district, and is tectonically bounded by the Longmenshan fold belt to the northwest, the Micangshan uplift to the north, the Emeishan–Liangshan fold belt to the southwest, and the flat belt in the central of the Sichuan Basin to the southeast. There is also a series of major N–S trending thrust belts within the area (Ning et al., 2015; Liu et al., 2016a; Li et al., 2017; Craig et al., 2018; Li et al., 2019; Wang et al., 2021) (Fig. 1B). Superimposed petroliferous basins in western China have regularly experienced complex tectonic movement events and multiple depositional histories since the Proterozoic (Li et al., 2014; Wang et al., 2014; Meng et al., 2015; Jin et al., 2017; Wang et al., 2017; Liu et al., 2021a). Based on its structural characteristics and deformation style, the Sichuan Basin has been inferred to be a Late Mesozoic foreland basin overlying a Sinian to Middle Mesozoic passive margin, and has experienced six primary phases of episodic deformation, basin development, and deposition (Ma et al., 2007; Liu et al., 2016a; Wu et al., 2017b; Ma et al., 2019). The tectonic events chiefly include the following orogenies: Yangtze (Pre-Sinian–Early Sinian: 850–320), Caledonian (Late Sinian–Silurian: ~320 Ma), Hercynian (Devonian–Permian: 225–205 Ma), Indosinian (Triassic: 205–195 Ma), Yanshanian (Jurassic to Cretaceous: ~140 Ma), and Himalayan (Tertiary–Quaternary: 80–3 Ma) (Hao et al., 2008; Liu et al., 2016a; Feng et al., 2017; Qin et al., 2018) (Fig. 3 and Fig. 4). Overall, the Western Sichuan Depression underwent subsidence and uplift prior to the Indosinian tectonic movements, and has been subjected to large-scale lateral compression since the Late Indosinian tectonic deformation (Hao et al., 2008; Xu et al., 2012) (Fig. 4).

More specifically, the Jinning tectonic movement consolidated the basement of the Yangtze Craton at the end of the Meso-Proterozoic (Ma et al., 2007; Tang, 2013; Jiang et al., 2014; Liu et al., 2021b) (Fig. 3). This was followed by numerous subsidence and regional uplift events that continued until the Himalayan orogeny. The tectonic and geological history of the Sichuan Basin can thus be summarized as follows: (i) the Tongwan tectonic movement at the end of the Sinian caused uplift and erosion that resulted in the development of an unconformity between the Late Sinian and Early Cambrian (Guo, 2020; Cai et al., 2021; Guo et al., 2021; Zhu et al., 2021; Wang et al., 2022). (ii) The Caledonian tectonic movement resulted in the northeast trending Leshan–Longnvsi paleo-uplift, which formed in the central Sichuan Basin at the end of the Silurian (Zhang et al., 2018; Liu et al., 2021a). (iii) The Yunnan tectonic movement at the end of the Carboniferous and the Dongwu movement at the end of the Early Permian caused uplift and erosion, respectively (Fig. 3). (iv) The Early Indosinian tectonic movement led to uplift and erosion that were caused by lateral compression from the Tethys plate toward the southwest and the Pacific plate toward the southeast during the latest Middle Triassic. A carbonate and evaporative-restricted platform developed because of this compression, and the rhomboid-shaped Sichuan Basin began forming (Ma et al., 2007; Xu et al., 2011; Zhang et al., 2018; Rangkey, 2020; Liu et al., 2021a) (Fig. 3 and Fig. 4). (v) The Late Indosinian tectonic movement caused rapid uplift of the western basin boundary at the end of the Triassic, whereas the Late Yanshanian tectonic movement led to the formation of a NE–SW trending fold in the eastern part of the basin. (vi) Strong lateral compression occurred during the Himalayan tectonic movement; the western, eastern, and northern boundaries of the Sichuan Basin uplifted rapidly, and a complete bruchfalten zone developed in the eastern part of the basin, which resulted in the present-day structural pattern (Xu and Zhao, 2010; Guo et al., 2014; Li et al., 2015; Qin et al., 2018; Liu et al., 2021a) (Fig. 3 and Fig. 4).

2.2 Stratigraphic overview

The regional stratigraphy of the Western Sichuan Depression was first defined in 1934, and it was subsequently modified by Chen et al. (1994), Meng et al. (2015), Xie et al. (2015), Li et al. (2017), and Liu et al. 2021. The basement is composed of stable and hard metamorphic rocks of the pre-Sinian Huodiya Group and Jinningnian magmatic rocks (Fig. 3 and Fig. 4). The basements are overlain by 6,000–12,000 m thick Late Sinian (Z_2) to Middle Triassic (T_2) continental and marine deposits, and these are further overlain by 2,000–6,000 m thick Late Triassic (T_3) to Quaternary (Q) continental deposits (Zhang et al., 2007; Li et al., 2015; Feng et al., 2017; Ma et al., 2019) (Fig. 3 and Fig. 4).

The Sinian (Sn) deposits were the first to develop above the Yangtze basement. The Early Sinian Doushantuo Formation (Sn_{1ds}) consists of 0–300 m thick of siliceous piedmont and fluvial deposits to the southwest, volcanoclastic materials to the west, and fluvial to offshore clastic rocks and shales or muds deposits to the southeast. The Late Sinian Dengying Formation (Sn_{2dy}) consists of 300–470 m thick of shallow-marine to offshore dolomite deposits (Guo et al., 2014; Zhao et al., 2014; Feng et al., 2017; Li et al., 2019) (Fig. 3 and Fig. 4). Cambrian–Silurian (Є–S) strata were deposited in an open to restricted platform. The Early Cambrian ($Є_1$) consists of 300–700 m thick black shales, siltstones, and muddy limestones, and the Late Cambrian ($Є_{2\text{-}3}$) consists of 200–700 m of dolostone interbedded with thin horizons of anhydrite (He et al., 2017). The Ordovician (O) strata consists of limestones, muddy limestones, and siltstones, with a thickness of 0–350 m. The Early Silurian (S_1) strata consists of ~150 m thick black shales, and the Middle Silurian (S_2) strata are comprised of black siltstones and mudstones (Ma et al., 2007; Jiang et al., 2014; Ma et al., 2019). Devonian (D) deposits are found only in the western part of the basin, are several meters thick, and mainly composed of quartz sandstone. Carboniferous (C) deposits are found in the eastern part of the basin, and are made up of dolostones that developed on tidal flats within a restricted platform. The Early Permian Maokou Formation (P_1m) was deposited on an open platform, and it consists of 200–450 m thick limestones interbedded with thin shales and muddy limestones. The Late Permian Longtan Formation (P_2l) developed in a continental–marine transitional environment in the southwestern part of the basin, and consists of ~50 m thick mudstones interbedded with coal; while the Wujiaping Formation (P_2w) (note: the P_2l/P_2w formations formed in simultaneously geological period but are named differently by researchers) was deposited in a restricted embayment in the northeastern part of the basin, and it is composed of ~100 m thick of marine mudstones and muddy limestones (Hao et al., 2008; Ma et al., 2019; Liu et al., 2021a). The Late Permian Changxing Formation (P_2ch) developed on a carbonate platform, and is composed of 100–150 m thick of limestones and dolostones. The Early Triassic

Feixianguan Formation (T_1f) was deposited on a shallow platform consisting of 300–400 m thick limestones and dolostones (Jiang et al., 2014; Jiang et al., 2018a), and the Early Triassic Jialingjiang (T_1j) Formation and Leikoupo (T_2l) Formation developed on a restricted and evaporative platform; both formations are made up of anhydrites and multiple cyclical dolomites and limestones, and reaching a total thickness range of 500–700 m and 400–1000 m, respectively (Jin et al., 2017; Liu et al., 2017; Liu et al., 2021a). Of these, the Leikoupo Formation (T_2l) is the main focus of this study, and it can be subdivided into four members: T_2l^1, T_2l^2, T_2l^3, and T_2l^4 (Jiang et al., 2018b) (Fig. 5). Following deposition of the Leikoupo Formation, a regional unconformity was formed by approximately 10 Ma of regional general erosion and karstification, which led to the development of breccias (Jiang et al., 2019). The subsequent Late Triassic Maantang Formation (T_3m) consists of a 10–30 m thick limestone deposit that is sometimes referred to as the Tianjingshan Formation (T_3t). The Xiaotangzi Formation (T_3xt) consists of black shales and siltstones with a thickness of 10 to 100 m that were deposited in a marine bay environment, and the timing of deposition is approximately equivalent to that of the first member of the Xujiahe Formation (T_3x^1) (Bei and Yang, 1980; Tang et al., 2013; Jiang et al., 2014; Liu et al., 2016a; Yang et al., 2016).

The Late Triassic Xujiahe Formation (T_3x) was deposited in a lacustrine delta and continental (fluvial) environments, and it consists of 250–3,000 m thick of sandstones, mudstones, and thin coal seams that are usually subdivided into six members (Liu et al., 2016a; Qin et al., 2018; Zhu et al., 2021). The Cretaceous (K) strata consist of approximately 2,000 m of conglomerates, whereas the Jurassic Ziliujing (J_1z), Shaximiao (J_2s), Suining (J_2sn), and Penglaizhen (J_3p) formations consist of 1,800–5,600 m of mudstones, sandstones, and conglomerates (Zhang et al., 2007; Liu et al., 2016b; Qin et al., 2018; Liu et al., 2021a). The upper strata of the basin is composed of Quaternary (Q) deposits with a thickness of approximately 70 m. These deposits consist of red mudstones, siltstones, sandstones, and locally unconsolidated conglomerates (Li et al., 2015; Ma et al., 2019). The generalized stratigraphic column, tectono-stratigraphic relationships, and the distribution of the rock units from the Sinian to the Quaternary are presented in Figs. 1B, 3, 4, and 5.

2.3 Petroleum geochemistry

Source rocks are the foundation of materials for oil and gas generation. Organic geochemical analyses contribute to sedimentary basin analysis by providing analytical data for the identification and assessment of source rocks (Peters and Cassa, 1994; Katz et al., 2008; Yin et al., 2011; Hakimi, 2012; Sachse et al., 2016; Liu et al., 2017a; Zhu et al., 2018). The potential for ultra-deep hydrocarbon exploration depends on the existence, quality, and quantity of source rocks (Magoon and Dow, 1994; Magoon et al., 2001; Ling et al., 2019; Hu et al., 2020; Sun et al., 2020; Su et al., 2022; Wang et al., 2022). To gain further geochemical insights into the mature source rock intervals described above, which are assumed for the Western Sichuan Depression, the origin of hydrocarbon gases were analyzed and the effective source rock units according to evaluation criteria were systematically correlated (Table 1).

2.3.1 Origin of hydrocarbon gases

Previous studies focusing on gas-source rock correlations have chiefly examined the gas samples produced in the gas fields adjacent to the Middle Triassic Leikoupo Formation (T_2l), including the Zhongba gas field, and the Hewangchang, Pengzhou, Yazihe, and Xinchang gas structures in the Western Sichuan Depression (Peters et al., 2005; Magoon et al., 2006; Wang et al., 2008; Huang et al., 2011; Feng et al., 2013; Liao et al., 2013; Wang et al., 2018). Results obtained from such examinations have indicated that the major gas components are methane (87.24%–98.79%), ethane (0.24%–0.39%), and propane (0.01%–0.73%), which generally exist together with an elevated variable hydrogen sulfide (H_2S) concentration of approximately 0.68%–9.97% (Jiang et al., 2018; Su et al., 2022). Carbon and hydrogen stable isotopes ($\delta^{13}C_{CH4}$: −32.0‰ to −32.8‰; $\delta^{13}C_2H_6$: −30.0‰ to −34.2‰; $\delta^{13}C_3H_8$: −26.5‰; δD_1: −140‰ to −145‰) are indicative of oil-associated gases that have a mixed thermogenic origin, and are primarily sourced from Type II mixed with partial Type III kerogen (Whiticar et al., 1994; Sun et al., 2020; Su et al., 2022). The He–Ne–Ar noble gas isotopic compositions are as follows: low ^4He 24.70 × 10^{-6} to 179.00 × 10^{-6} and low ratios of $^3He/^4He$: 0.01 to 0.02; ^{20}Ne ranging from 0.13 × 10^{-6} to 3.05 × 10^{-6}, $^4He/^{20}Ne$: 60.75 to 745.20; ^{40}Ar ranging from 106.50 × 10^{-6} to 1429.00 × 10^{-6}, $^4He/^{20}Ar$: 0.13 to 1.68; and $^{40}Ar/^{36}Ar$: 296.80 to 326.10. These features with the $^3He/^4He$ versus $^4He/^{20}Ne$, and $^3He/^4He$ versus $^{40}Ar/^{36}Ar$ classification plots suggest that the gases originated from organic matter deposits derived from the sedimentary crust instead of having an abiogenic origin related to the mantle or lower crust (Schoell, 1983; Whiticar et al., 1994; Hill et al., 2007; Katz et al., 2008; Kotarba and Nagao, 2008; Sun et al., 2020; Su et al., 2022). Together, the source rock characteristics, natural gas components, carbon and hydrogen isotopes, the results of He-Ne-Ar isotope comparisons, and the hydrocarbon generation processes, indicate that the gases most likely originated from the organic-rich intervals of the underlying Permian Longtan/Wujiaping Formation (P_2l/P_2w), which is comprised of dark-gray marl, coal, and carbonaceous shale source rocks, and contains a contribution from the algal-rich carbonate source rocks of the interior self-sourcing Leikoupo (T_2l) and Maantang (T_3m) formations (Sun et al., 2020). These gases simultaneously mixed with gases from the siliciclastic source rocks of the Xiaotangzi Formation (T_3xt) that directly overlie the Leikoupo (T_2l) and Maantang (T_3m) formations (Katz and Ehret, 2000; Katz et al., 2008; Xu et al., 2012, 2013; Liao et al., 2013; Meng et al., 2015; Liu et al., 2020; Su et al., 2022).

2.3.2 Source rock characteristics

2.3.2.1 Late Permian Longtan/Wujiaping Formation (P_2l/P_2w)

Outcrops and subsurface materials from the Upper Permian Longtan/Wujiaping Formation (P_2l/P_2w) consist of dark-gray muddy limestones, coals, carbonaceous shales, siliceous rocks and siliceous mudstones (Guo et al., 2018; Wang et al., 2021). The gammacerane/C_{30}hopane ratios of the P_2l/P_2w range from 0.2 to 0.3, Pr/Ph ranges from 0.80 to 1.50 (average: 0.90), and the odd-even alkane predominance indices (OEP) range from 0.98 to 1.64 (average: ~1.14). Additionally, the $\delta^{13}C_{PDB}$ (‰) ranges between −26.7‰ and −28.7‰ (average: −27.5‰). These characteristic combinations roughly reflect that the P_2l/P_2w was formed in an anoxic to oxidizing low-energy marine–continental transitional environment (Feng et al., 2015). TOC values range from 0.50 wt. % to 18.37 wt. % (average: 3.23 wt. %), chloroform bitumen "A" from 10,000–460,000 ppm (average: 270,000 ppm), TOC hydrogen index (HI) varies from 0.23–10.24 mgHC/g, T-max: 480–520 °C (Chen et al., 2018); and %Ro ranges from 1.0% to 3.0%. The stratum contains Type II and III kerogen, and it has a stratigraphic thickness of 30 m to 120 m. Therefore, P_2l/P_2w could be classified as a good to excellent source rock (Zhang et al., 2007; Hao et al., 2008; Qin et al., 2016; Chen et al., 2018; Guo et al., 2018; Ma et al., 2019; Sun et al., 2020) (Fig. 3) (Table 1).

2.3.2.2 Middle Triassic Leikoupo Formation (T_2l)

The characteristics of this unit include high gammacerane/C_{30}hopane ratios ranging from 0.08 to 0.41, Pr/Ph ranging from 0.33 to 0.94 (average: 0.76), OEP ranging from 0.91 to 1.06 (average: ~1.00), $\delta^{13}C_{PDB}$ (‰) ranging between −26.6‰ and −23.6‰ (average: −26.0‰), and $\delta D_{Kerogen}$ values varying from −132‰ to −58‰, with an average of −99‰. Overall, these data reflect deposition in a hypersaline environment characterized by high salinity and water stratification. The salty environment with lower sulfate was beneficial for preserving and transforming the organic matter of the source rocks, and the kerogen mainly originated from marine organisms, including phytoplankton, zooplankton, and bacteria (Bei and Yang, 1980; Yin et al., 2011; Karakitsios, 2013; Guo et al., 2014; Wang et al., 2018; Wood et al., 2019) (Fig. 5). Lithologically, T_2l is predominantly a dark, algal-rich dolomite, with a

TOC range of 0.20–1.30 wt. % (average: 0.36 wt.%), chloroform bitumen "A" of 4,200–708,600 ppm (average: 62,700 ppm), TOC hydrogen index (HI) of 48.90–296.40 mgHC/g, T-max of 462–554 °C, and % EqvRo of 1.20% to 1.50% (calculated by the reflectance of solid bitumen) (Hao et al., 2008; Sun et al., 2020). Organic matter within T_2l is comprised of Type II or III kerogen, and the unit has a thickness of approximately 384 m. This formation could be classified as a fair to good source rock (Katz, 1995; Zhang et al., 2007; Xu et al., 2013; Qin et al., 2016; Li et al., 2017; Sun et al., 2020; Su et al., 2022) (Fig. 3 and Fig. 5) (Table 1).

2.3.2.3 Late Triassic Maantang Formation (T_3m)

The gammacerane/C_{30}hopane ratios of the stratum range from 0.14 to 0.20, Pr/Ph ranges from 0.44 to 0.55 (average: 0.50), and OEP ranges from 0.96 to 1.04 (average: ~1.00). Overall, these data reflect deposition on a carbonate ramp that included marine–continental facies (Fig. 5). The gray, and muddy limestones of the Late Triassic Maantang Formation (T_3m) have a TOC value ranging from 0.20 – 0.33 wt. % TOC, with an average TOC value of 0.23 wt.%, chloroform bitumen "A" of 4,700–10,500 ppm (average: 7,100 ppm), TOC HI index ranging from 10.0–18.10 mgHC/g, T-max of 513–565 °C, %Ro in the range of 1.0% to 1.3%, and the dominant kerogen type is Type II; the stratum has a thickness of 10 m. The T_3m formation could be classified as a poor to fair source rock (Katz, 1995; Ye, 2003; Sun et al., 2020; Su et al., 2022) (Fig.3 and Fig. 5) (Table 1).

2.3.2.4 Late Triassic Xiaotangzi Formation (T_3xt)

The gammacerane/C_{30}hopane ratios of this stratum range from 0.10 to 0.21, Pr/Ph ranges from 0.41 to 0.87 (average: 0.72), OEP ranges from 0.97 to 1.07 (average: 1.01). These data indicate that the source rock was deposited in an occluded bay that contained marine–continental transitional facies (Fig. 5). The dark mudstone and shale of the Late Triassic Xiaotangzi Formation (T_3xt), has a TOC value of 0.53–0.95 wt. % with an average TOC of 0.80 wt.%, chloroform bitumen "A" of 6,700–70,900 ppm (average: 20,700 ppm), a TOC HI index of 4.68–20.31 mg HC/g, T-max of 475–582 °C, a %Ro of 1.2% to 1.3%, the dominant kerogen is Type III, and the stratum has a thickness of 82 m. The T_3xt could thus be classified as a moderate source rock (Ye, 2003; Shen et al., 2008; Sun et al., 2020) (Fig.3 and Fig. 5) (Table 1).

3 Sample Collection and Analytical Methods

3.1 Sample collection

The present study involved conducting analyses of new multidisciplinary datasets that included detail observations of fresh outcrops with a thickness of 50 m, petrologic examination of cores with a total length of 100 m, and lithologic analyses of 108 reservoir samples collected from six scientific and exploration wells: YS1, PZ1, XQS1, CK1, XCS1 and TS1 (Fig. 2). Simultaneously, the organic geochemistry was analyzed of samples that included 73 rock cuttings, the composition of four natural gas samples, carbon and hydrogen isotopes, and the He-Ne-Ar isotopes of five noble gases (see the detailed analysis dataset and source rock to gas correlations published in Sun et al., 2020 (Fig. 5) (Table 1)). The porosity and permeability were interpreted by wire-line logging at a depth of 5,500 m to 6,900 m collected from wells PZ1, XQS1, CK1, XCS1, and TS1. Additionally, two seismic profile records acquired from the Library of China Exploration Company, SINOPEC, Chengdu were interpreted (Fig. 5) (Supplemental Material 1, 2 and 3).

In total, 83 representative carbonate reservoir core samples were collected from wells YS1, CK1, PZ1, and TS1 (Fig. 2). These samples belonged to various intervals of the Middle Triassic Leikoupo Formation (T_2l), and were used to evaluate conventional petrophysical parameters of the reservoir rocks (i.e., petrographic characteristics of the reservoir, structure and texture of the reservoir, and physical properties, including conventional helium porosity and permeability, and the mercury injection capillary pressure [MICP]). The burial depths of the samples ranged from 5,741.80 m to 6,612.40 m. Details of the stratigraphic locations, rock types, and petrographic characteristics are provided in Supplemental Material 1 and 2.

Another set of 25 representative core samples were collected from the carbonate intervals of the Middle Triassic Leikoupo Formation (T_2l) that were found in four exploration wells, including YS1, PZ1, XQS1, and XCS1 (Fig. 2). Each sample was described using thin-section and scanning electron microscope (SEM) petrographic observations, analyses of fluid inclusions within calcite and dolomite cements, and measurements of micro-thermometric homogenization temperatures. Burial depths of the core samples ranged from 5,764.00 m to 6,179.80 m and the specific stratigraphic locations of the samples are provided in Supplemental Material 4.

3.2 Analytical methods

3.2.1 Thin-section and SEM observations

Lithofacies and microporosity characteristics were determined from polished thin sections of carbonates cut from core plugs using a polarizing microscope and SEM housed at the Petroleum Geology and Engineering Laboratory of the State Key Laboratory of Oil and Gas Reservoir Geology and Exploration, Chengdu University of Technology (CDUT), China. Eighty-three thin sections were cut from 2 cm × 2 cm samples and impregnated with red S or blue epoxy resin to petrographically classify the samples and determine the type of pore space (Baker et al., 2000; Blazevic et al., 2009; Fu and Qing, 2011; Al-Aasm and Crowe, 2018; Loucks and Dutton, 2019; Woods et al., 2019; Li et al., 2019). The thin sections were qualitatively described and classified using the conventional carbonate rock and pore-space type classifications provided by Dunham (1962) and Lokier and Al Junaibi (2016). Optical microscopy using a Leica DM4500P (Leica Company, DE) was conducted to observe the petrographic characteristics of each thin section in order to determine and quantify mineral compositions and contents, and establish the diagenetic evolution and relative timing of these events (Jordan and Wilson, 1994; Wilson et al., 2007; Regnet et al., 2019). A field-emission environmental SEM Quanta 250 FEG (FEI Company, USA) was used to examine the selected samples and provide information about the mineral microstructure and pore-space system geometry that could not be distinguished using a polarizing microscope. The preparation for SEM analysis consisted of embedding the sample in a holder or device and then polishing to achieve a flat cross section, milling it using a high-energy argon ion beam, coating the sample surface with a conductive carbon film, and then observing it with the SEM (Jordan and Wilson, 1994; Baker et al., 2000; Erdman et al., 2006; Higgs et al., 2007; Guo et al., 2019; Wu et al., 2019).

3.2.2 Porosity and permeability measurements

For a sedimentary rock to be a suitable reservoir unit, it must be both porous and permeable. In this respect, porosity is represented by the amount of relative pore spaces in a rock, and permeability is associated with the ability of a rock to transmit fluid flow (Alsharhan, 2003; Sonnenberg and Pramudito, 2009; Akintunde, 2014; Lai et al., 2015; Katz and Arango, 2018). Conventional core plug porosity and permeability (helium) data were obtained for 83 samples using standard laboratory measurements obtained on 1.5-inch diameter standard core plugs at the Special Petrophysics Laboratory of the State Key Laboratory of Oil and Gas Reservoir Geology and Exploration, CDUT, China. The analyses were conducted using an automated core measurement system CMS-300 (Core Laboratories Inc., USA), which combines a porosimeter and permeameter in one instrument to enable measurement of both porosity and permeability to be determined (Alsharhan, 2003; Sonnenberg and Pramudito, 2009; Gomez et al., 2010; Akintunde, 2014; Li et al., 2015; Fang et al., 2016; Jiang et al., 2018a). Furthermore, porosity and permeability were quantitatively extrapolated using wire-line logging data interpretation via the Interactive Petrophysics Software developed by Senergy (GB) Limited, UK to ensure a precise comparison and comprehensive evaluation of the reservoir petrophysical properties and pore systems (Al-hasani et al., 2018; Ahmed et al., 2018; Ali et al., 2019; Hu et al., 2019; Marek, 2019) (Table 2).

3.2.3 Mercury injection capillary pressure (MICP) analyses

MICP is a widely used indirect method for measuring pore and throat size distributions (Okoli et al., 2015; Hu et al., 2019; Wu et al., 2019; Hu et al., 2020; Wen et al., 2023). MICP analyses were conducted using a Micromeritics Poresizer 9320 (Micromeritics Instruments Corporation, USA) at the Special Petrophysics Laboratory of the State Key Laboratory of Oil and Gas Reservoir Geology and Exploration, CDUT, China. A total of 42 samples with masses between 4.75 g and 5.25 g, were crushed (−1.4 mm mesh size) and analyzed. The equivalent pore radius was calculated according to the capillary pressure using the Washburn equation:

$$P_c = \frac{-2\gamma_{Hg}\, Cos\theta_{Hg}}{r} \quad (1)$$

where P_c ranges from 0 to 200 MPa, interfacial tension, r_{Hg} = 485 mN/m, and the wetting angle, θ_{Hg} = 130° (Sutton, et al., 2004; Schmitt et al., 2013; Hu et al., 2017; Hu et al., 2020). All core plugs were first cleaned thoroughly with ethanol to remove all traces of oil, dried under vacuum at more than 105 °C for 3 h, and then equilibrated for 5 h at room temperature before analysis. The samples were subsequently placed into the head of a dilatometer, which was then installed into a mercury intrusion instrument and slowly filled with mercury under a low pressure. The mercury molecules gradually migrated into small pores with an increase in the test pressure from 0.5 MPa to 200 MPa, enabling detailed information to be collected from the micropore regions (Schmitt et al., 2013; Guo et al., 2019; Wu et al., 2019; Hu et al., 2020). The pore-throat size distribution was derived from data points along the capillary pressure curves, and the pore-throat diameter median and standard deviation were calculated. The sorting coefficient (S_p) represents the standard deviation of the porosity throat size of sample, which directly reflects the concentration of porosity pore distribution, and is given by the statistical formula

$$S_p=\frac{\Psi 84-\Psi 16}{4}+\frac{\Psi 95-\Psi 5}{6.6} \tag{2}$$

The skewness (S_{kp}) represents the asymmetry of the pore-throat size distribution, and is given by the statistical formula

$$S_{kp}=\frac{\Psi 84+\Psi 16-2\Psi 50}{2(\Psi 84-\Psi 16)}+\frac{\Psi 95+\Psi 5-2\Psi 50}{2(\Psi 95-\Psi 5)} \tag{3}$$

where Ψi represents the value of i% for every Ψ corresponding to the normal probability mercury saturation curve. Porosity and permeability (Hg) were also determined by MICP analysis (Schmitt et al., 2013; Zhang et al., 2016; Huang et al., 2017) (Table 2 and Supplemental Material 2).

3.3.4 Fluid inclusions analyses

Twenty-five fluid inclusion samples were examined at the Fluid Inclusion Laboratory of the Analytical Laboratory, Research Institute of Uranium Geology, Beijing, China. Each core sample was prepared as a thick, doubly polished section, with a thickness of approximately 60 μm. All samples were first observed under a microscope to determine the petrography of fluid inclusions (Hu et al., 2012; Figueiredo e Silva et al., 2013; Jiang et al., 2014; Mansurbeg et al., 2016; Lu et al., 2017; Sachan et al., 2017). Subsequently, the homogenization temperatures (T_h) of aqueous fluid inclusions that co-existing with the hydrocarbon fluid inclusions were measured and segregated from the liquid-dominated ones that had relatively low vapor percentages (Al-Aasm and Crowe, 2018; Al-Aasm et al., 2018). The reservoir burial and thermal evolution histories were also determined and used to characterize the timing and periods of hydrocarbon charging (Lu et al., 2017; Sachan et al., 2017). A detailed petrographic analysis of the fluid inclusions was conducted using a ZEISS AXIO Imager A1m microscope that transmitted white light and provided an ultraviolet excitation light source. The microthermometry of oil and aqueous fluid inclusions was measured using a Linkam THMS-G600 (Linkam Scientific Instruments Limited, UK) during the heating–freezing stage and followed the standard procedures. The heating and freezing rates were set up to 10 °C /min during the initial runs but then reduced to 1 °C/min when close to phase transformations. The temperature measurement was approximately ±1 °C (Chi et al., 2012; Figueiredo e Silva et al., 2013; Jiang et al., 2014; Zhu et al., 2015b; Lu et al., 2017; Shen et al., 2017).

4 Results

4.1 Reservoir petrography

The combination analyses of sedimentary structures, textures, the petrography of field outcrops, drilling core observations, thin sections, and SEM imagery observations provided detailed reservoir information that was compiled for each of the four members of the Middle Triassic Leikoupo Formation (T_2l) in the Western Sichuan Depression (Fig. 6, Fig. 7-1, 2, and Fig. 8-1, 2) (Table 3).

T_2l^1 Member of the Leikoupo Formation: the lithology consists mainly of dense thin-bedded argillaceous dolomite, microcrystalline to finely crystalline dolomite, and medium to coarse crystalline saddle dolomite (Fig. 6A and Fig. 7-1L). Typical diagenetic phenomena include hydrothermal pyritization, celestite precipitation, and dolomitization (Fig. 9).

T_2l^2 Member of the Leikoupo Formation: the stratum comprises fine-grained argillaceous limestone, granular dolomite, arenaceous dolomudstone, dolomitic breccias and oolitic dolograinstone, micritic- to finely-crystalline muddy limestone, crystalline packstone, and fine- to coarse-grained ferruginous limestone (Figs. 7-1G, H, I, K and N). The main diagenetic phenomena include epigenetic karstification, recrystallization, pressure-solution, infilling (e.g., pyritization, calcite precipitation, celestite growth, and silicification), fracturing and faulting (Fig. 9).

T_2l^3 Member of the Leikoupo Formation: the lithologies that comprise this member include: algal dolomite, microbially-derived dolomudstone, thrombolitic dolomite, flat to undulate, laminated and fenestrae stromatolitic dolomite, fine-crystalline sandy dolomite, and microcrystalline gypsum-bearing dolomite (Fig. 7-1J, O). Common diagenetic phenomena include calcite cementation, chemical compaction (stylolites), and dolomitization (Fig. 9).

T_2l^4 Member of the Leikoupo Formation: the stratum is comprised of gray calcarenite packstones, dark-gray to gray micritic limestone, dark-gray dolomite, and dark-gray microcrystalline dolomicrite that are intercalated with white gypsum interbeds. Breccias are abundant and occur in both the dolostone and limestone intervals (Figs. 3, 5, 6, Figs. 7-1A-F and M, Fig. 7-2, and Fig. 8-1, 2). Frequently observed diagenetic phenomena include epigenetic karstification and the partial infilling of dissolution pore spaces with silica, celestite, gypsum, and calcite cements (Figs. 7-2G, I, J, Fig. 8-2, and Fig. 9).

4.2 Reservoir pore-space system

The macropore classification in this study mainly follows that of Choquette and Pray (1979), and micropores were determined based on the methods of Lucia and Loucks (2013) and Jiang et al. (2019). The Middle Triassic Leikoupo Formation carbonate reservoir contains several different types of primary and secondary pore spaces. The types of macropores (>10 μm) are as follows: (a) solution-enlarged pores, vugs, holes and cavities, (b) intraparticle pores, (c) intercrystalline pores, (d) interparticle pores, (e) intergranular pores, (f) fractures, (g) stylolites, and (h) micropores (<10 μm). Most of the primary pore space characteristics have been modified by post-depositional diagenetic processes. Different types of reservoir pore spaces are connected to each other through pore throats, and they combine to form effective three-dimensional networks. The pore types are described in detail as follows:

a. Solution-enhanced pores, vugs, holes and cavities: pores in the dolostone reservoirs are dominated by secondary solution-enlarged interparticle pores that are found in most petrologic types and fall into three main occurrences. The first type is characterized by solution-enlarged micropores with sizes commonly ranging between 200 μm and 1000 μm; some pore-filling material and dust are found on the dissolution-affected grain surfaces, or they have grown around euhedral dolomite crystals (Fig. 6F, Figs. 7-2B, G, H, I, J, and Fig. 8-1A, C). The second type is characterized by solution vugs with sizes ranging from 2 mm to 500 mm. Solution vugs formed during the burial stage and subsequently expanded along pre-existing porosity and fracture zones (Figs. 6B, D, E and Fig. 7-2B). The third type is characterized by solution holes and karst cavities with sizes usually larger than 500 mm. They have commonly developed along structural joints, stylolites, and other types of fractures that are particularly associated with unconformities that developed due to paleo-karstification. Solution-enhanced pores, vugs, and holes are easily observed in drilling cores, thin sections, and in outcrops (Fig. 6B, E and Fig. 8-2).

b. Interparticle pores: interparticle pores are commonly observed in grainstone units within the dolostone reservoir, which comprises mainly microbial clots and peloids in the study interval (Fig. 7-1D, F and Fig. 7-2H). Although widespread, this pore type is not dominant, and it does not contribute significantly to the present-day porosity of the reservoirs. Interparticle pores range in size from 20 μm to 100 μm, and are commonly associated with dolomite solution-enhanced vugs.

c. Intercrystalline pores: intercrystalline pores are commonly observed in dolomudstone in the T_2l^{3-4} (Fig. 7-1J, O). This pore type represents only a small proportion of the total porosity. Intercrystalline pores occur either as isolated pore spaces or in association with solution micropores, and they range in size from approximately 10 μm to 50 μm and are occluded by calcite and quartz cement in places (Fig. 7-1B, E, Figs.7-2A, D, F, and Figs. 8-1A, F, G, H).

d. Intraparticle pores: fabric-destructive dolomite within the dolostone reservoir consists mainly of dolomitized ooid grains with abundant intraparticle pores. Dolomite cement commonly grows into the interparticle pore spaces on top of ooid grains, with calcite cement mostly occupying the rest of the interparticle pore space. (Fig. 7-1D, E).

e. Intergranular pores: these pores are commonly formed due to dolomitization, and dolomite pores may also be affected by late-stage crystal growth, such as hydrothermal dolomitization and saddle dolomites that are formed in the open sutures (Fig. 8-1H and Fig. 7-2C, E).

f. Fractures: fractures are commonly associated with structural activity. They play a dual role within the reservoir, and acting as both an effective storage space and an oil and gas infiltration channel (Al-Aasm and Crowe, 2018). There are three fracture types in the first to fourth members of the Leikoupo Formation: (1)

Microfractures (generally with widths of less than 20 μm) are commonly present in both the limestone and dolostone intervals of the $T_2l^{1\text{-}4}$ strata, including within brecciated zones. The formation of microfractures appears to be the final fracturing event that occurred in these reservoirs because they crosscut all of the diagenetic minerals, previous fractures, carbonate host rocks, and breccias (Figs.7-1E, F, L, G and Fig. 7-2E, I). Micro-fractures were observed under SEM in association with a small number of solution micropores (Fig. 8-1B, D). (2) Macro-fractures (generally with widths ranging from 20 μm to 1 mm) within the stratum likely underwent at least three phases of structural fracture development. Fracture type I are filled with calcite, whereas fracture type II are not filled but they interweave with fracture type I and are commonly found in association with secondary minerals, such as calcite, pyrite, celestite, gypsum, iron minerals, and dolomite that completely or partially fill the fractures. Fracture type III are microfractures filled with calcite cement, and they crosscut fracture type I and II (Fig. 7-1H). They form a series of mutually connective linear channels that operate as an effective complex fracture network system (Figs. 6A, F, G, Fig. 7-1I, J, and Fig. 7-2H). (3) Cracks: cracks (> 1mm) that expanded due to corrosion were then partially filled with dolomite, calcite, and gypsum, and these can act as good oil and gases reservoir spaces and migration channels. The effective storage space of the study area comprises mainly unfilled cracks, solution holes, and other secondary pores. Representative cracks are shown in Fig. 6A and Fig. 17.

g. Stylolites: stylolites are associated with pressure-solution and are non-structural joints that likely account for primary porosity. They are more commonly observed in the middle to upper intervals of the Leikoupo Formation (T_2l^{2-4}). Residual bitumen, pyrobitumen, clay minerals, and organic matter stains occur as infillings along the stylolites (Figs. 7-1O, M and N).

h. Micropores: Micropores appear to occur widely in the microbially-derived dolomudstones. This pore type generally has two main occurrences: it predominantly occurs as intragranular micropores that are commonly associated with intercrystalline pores, solution-enlarged pores, and vugs. These micropores were identified with using SEM and their pore sizes are generally less than 10 μm (Fig. 7-2D and Figs. 8A, B, C, G). The less commonly occurrence type of micropores developed along microfractures (Fig. 6G).

4.3 Porosity and permeability

Helium was used to measure the porosity and permeability in core plugs (the first member of the Leikoupo Formation was not tested due to a lack of samples). The following results were obtained for porosity and permeability, respectively, in the remaining members: 0.6% to 2.6% (average: 1.5%), and 0.004 mD to 125.2 mD (average: 11.0 mD) in the second member of the Leikoupo Formation (T_2l^2) (n = 26); 1.4% to 4.1% (average: 2.2%), and 0.003 mD to 15.0 mD (average: 1.5 mD) in the third member of the Leikoupo Formation (T_2l^3) (n = 28); 1.3% to 3.7% (average: 2.1%) and 0.02 mD to 9.2 mD (average: 0.8 mD) in the lower fourth member of the Leikoupo Formation (T_2l^{1-4b}), which is located below the epigenetic karstification zone (n = 16) (Fig. 8-2 and Fig. 10-1) (Supplemental Material 1). In the nearby unconformity-related karstification zone, in which the paleo-karst is strongly developed in the uppermost fourth member of the Leikoupo Formation (T_2l^{4a}) (n = 13), porosity (measured by helium in drilling core) ranges from 1.8 to 14.2% (average: 6.0%), and permeability ranges from 0.2 to 7.7 mD (average: 3.4 mD) (Figs. 6, 7, 8-2, 10-2) (Supplemental Material 1).

Interpretations from wire-line logging from well CK1 showed the following porosity and permeability results, respectively: from 2.3% to 5.8%, and 0.01 mD to 0.4 mD in the first member of the Leikoupo Formation (T_2l^1), with a net pay reservoir thickness of 38.8 m; 2.3% to 4.5% and 0.01 mD to 0.6 mD in the second member of the Leikoupo Formation (T_2l^2), with a net pay reservoir thickness of 30.5 m; 2.3% to 8.5%, 0.01 mD to 12.0 mD in the third member of the Leikoupo Formation (T_2l^3), with a net pay reservoir thickness of 85.1 m; 4.3% to 8.0% and 0.09 mD to 1.0 mD in the fourth member of the Leikoupo Formation (T_2l^4), with a net pay reservoir thickness of 28.3 m. These records are summarized in Figs. 6, 7, 8-1, 2, Fig. 9, Fig. 10-3, and Supplemental Material 3.

4.4 Mercury injection capillary pressure

The MICP analyses (as above the first member of Leikoupo Formation (T_2l^1) could not be analyzed due to a lack of samples) indicated the following respective porosity and permeability values: 0.2% to 1.2% and 0.004 mD to 33.0 mD for the second member of the Leikoupo Formation (T_2l^2) (n = 14), with a sorting coefficient ranging from 0.2 to 1.8, skewness ranging from −5.5 to −1.2, and a pore structure related to medium coarse to fine pore-throat sizes; 1.1% to 2.3% and 0.003 mD to 15.0 mD for the third member of the Leikoupo Formation (T_2l^3) (n = 16), with a sorting coefficient ranging between 0.9 and 1.9, skewness from −0.7 to 0.5, and a pore structure related to medium coarse to fine pore-throat sizes; 0.9% to 1.6% and 0.02 mD and 9.2 mD for the fourth member of the Leikoupo Formation (T_2l^4) (n = 12), with a sorting coefficient ranging from 0.8 to 2.8, skewness ranging from −2.1 to −0.4, and a pore structure that is dominated by coarse to large throats (Fig. 11 and Fig. 12) (Supplemental Material 2). The other relevant reservoir parameters (including capillary pressure, mercury saturation, and pore-throat radius distributions) determined by MICP for well CK1 are shown in Fig. 12 and Supplemental Material 2.

4.5 Fluid inclusion petrography and homogenization temperatures

4.5.1 Fluid inclusion petrography

The petrography of representative core samples from the fourth member of the Leikoupo Formation (T_2l^4) (Wells PZ1, XQS1, and XCS1) includes dolomicrites, fine-crystalline dolomites, white calcite veins, and marl containing calcite veins (Supplemental Material 4). Transmitted-light photomicrographs of fluid inclusions from these three wells show that the microfractures in most samples are filled with abundant dark-brown bitumen and light-brown, medium-light crude oil that exhibits strong light-blue fluorescence (Fig. 13A). Two generations of minerals infill the microfractures, including early-stage dolomites and late-stage calcite cements. Texturally, the coexistence of two types (Types I and II) of hydrocarbon and another type (Type III) of saline aqueous fluid inclusion populations, which are observed as follows:

Type I contains dark brown liquid hydrocarbon inclusions. The frequency of grains containing oil inclusions (GOI) is greater than 20%, and they are primarily distributed within the early dolomite cement infillings (Fig. 13A and B).

Type II contains brown to dark-gray gas (±60%) and/or liquid (±40%) single/two-phase hydrocarbon inclusions with a grouped distribution in the later-stage generated calcite infillings of fractures and holes. The GOI is greater than 20%, which implies that the hydrocarbons accumulated after fracture formation and calcite cement growth (Figs. 13A, B, and E). The amount of Type II inclusions dominant over than Type I inclusions.

Type III saline aqueous fluid inclusions are two-phase inclusions (V_{CO2}+L_{H2O}) that occur in dolomite or calcite cements near fractures and holes. Vapor/liquid volume ratios for the majority of the inclusions are <5%. The size of these fluid inclusions is small (diameter varying from 1 μm to 14 μm, with an average of approximately 2–5 μm) and they are regular in shape (Figs. 13B, C, D, and F) (Supplemental Material 4).

4.5.2 Fluid inclusion microthermometry

Microthermometry reveals compositional variations in the inclusions resulting from aqueous-carbonic to aqueous processes; the analyses were conducted on minerals in the dolomite and calcite cements. A total of 149 saline aqueous fluid inclusions (Type III) were measured from random populations. Saline aqueous fluid inclusions commonly accompany oil and gas inclusions, and thus the two were usually found grouped together (Figs. 13B, C, D, and F). The measured homogenization temperatures (T_h) ranged from 98 °C to 171 °C, and were divided into two groups: 98–130 °C and 130–171 °C. The specific thermometric measurement results are shown in Fig. 14 and summarized in Supplemental Material 4.

5 Discussion

5.1 Reservoir diagenetic evolution; comprehensive evaluation of quality and quantity; and main factors controlling formation

5.1.1 Diagenetic processes associated with reservoir evolution

The Middle Triassic Leikoupo Formation (T_2l) natural gas reservoir is characterized by its great burial depth of 5,500–8,000 m, and thus falls under the definition criteria of an ultra-deep reservoir. (Fu and Qing, 2010; Li et al., 2015) (Figs. 8-2, 16, 17). Compare to carbonate deposits experiencing shallow burial depths conditions, the properties of ultra-deeply buried carbonate reservoirs vary laterally, and they are often strongly heterogeneous because of complicated diagenetic processes that substantially modify the pore systems (Neilson et al., 1998; Machel and Lonnee, 2002; Garland et al., 2012; Feng et al., 2015; Jin et al., 2017; Wei et al., 2017; Atchley et al., 2018). Despite this observation, there are several productive carbonate reservoirs where specific diagenetic processes have preserved or enhanced the primary porosity, and/or created secondary porosity (Rosales et al., 2018). The overall diagenetic history of the Middle Triassic Leikoupo Formation (T_2l) can be divided into near-surface syn-depositional, early shallow-to-moderate burial, and late deep burial three diagenetic stages (Fig. 9). The transitions between these different stages were gradual, and some diagenetic events may have occurred across multiple stages (Wilson et al., 2007; Fu et al., 2008). However, all of the diagenetic processes observed in samples from the study wells must have occurred within a burial environment from ~60 °C to 200 °C (Fig. 9 and Fig. 16). Diagenetic events were identified for this study based on detailed field and core observations, as well as thin section and SEM analyses. Accordingly, the complex diagenetic processes that improved the porosity and/or permeability of the petroleum reservoirs can be classified as being constructive, whereas those that reduced the porosity and/or permeability of are classified as being destructive (Fig. 6, Fig. 7-1, 2 and Fig. 8-1, 2), and these are elaborated on in the following subsections. Additionally, the paragenetic sequences, relative timing, and evolutionary degree (weak/strong) of the diagenetic events and pore-forming processes were qualitatively or quantitatively determined from the petrographic relationships and frequency of diagenetic features or phenomena appearing in samples; and these are summarized in Fig. 9 (Chen et al., 2013; Mansurbeg et al., 2016; Feng et al., 2017; Tang et al., 2022).

5.1.1.1 Constructive diagenesis

Constructive diagenetic processes primarily include epigenetic paleo-karstification, burial dissolution, structural movements, pressure-solution (stylolites), and dolomitization, which are described below:

(1) Epigenetic paleo-karstification: Paleo-karstification has a favorable influence on reservoirs and improves reservoir quality. An effective reservoir exhibits an intense stratal distribution near an unconformity-related paleo-karst zone, with a paleotopograhy ranging from 10 m to 200 m, that mainly related to the upper most fourth member of Leikoupo Formation (T_2l^{4a}) (Jordan and Wilson, 1994; Chen et al., 2016; Liu et al., 2016a; Wang et al., 2018; Li et al., 2019; Pontes et al., 2021) (Fig. 9 and Fig. 15) (Table 3). The amount of dissolution mainly depends on how long the sediments were exposed to CO_2-enriched waters containing organic acids (Jordan and Wilson, 1994; Lai et al., 2015; Li et al., 2019). Direct evidence of epigenetic paleo-karstification includes solution-collapse breccias, dissolution-enhanced pores, vugs, holes, and caves (Qing and Nimegeers, 2008) (Figs. 6, 7-1, 7-2, and 8-2).

(2) Burial dissolution: Burial dissolution was the key factor in the development of carbonate reservoirs within the Middle Triassic Leikoupo Formation (T_2l), and it is interpreted to have occurred periodically during the Yanshanian and Himalayan tectonic periods (Fu et al., 2008; Shen et al., 2017). Many researchers have proposed that fluid-rock interactions in the deeply- or ultra-deeply burial dissolution of carbonates could have been induced by different geological processes, such as: (a) bacterial sulfate reduction (BSR) in relatively shallow burial diagenetic settings at lower temperatures of less than 60~80 °C, because above this temperature range, almost all sulfate-reducing microbes cease to metabolize. The BSR activity played an important role in driving the dissolution of sulfate rocks (e.g. anhydrite, gypsum) and

H_2S production, supporting the pyrite and calcite cementation formed and the development of hypogenic karst in the weathering crust (Machel, 2001; Saller et al., 2014); (b) thermochemical sulphate reduction (TSR) that occurs in relatively deep burial diagenetic environments under higher temperatures ranging between 110 and 200 °C. The products of TSR and BSR are similar, TSR reaction facilitate the cotinouous deep dissolution and locally enhance the porosity of reservior (Fig. 7-1) (Machel, 2001; Saller et al., 2014; Jiang et al., 2018); and (c) hydrocarbon generation in source rocks involving CO_2, H_2S, elemental sulfur, or organic acid-rich fluids, which thus generates secondary dissolution pores that have an overall positive effect on reservoir quality (Lai et al., 2015; Wei et al., 2017; Jiang et al., 2018a, b; Tian et al., 2018; Hao, 2022; Li and Cai, 2022). The Middle Triassic Leikoupo carbonate reservoir was modified by mesogenetic dissolution and hydrothermal karstification, where dissolution creates a spectrum of voids (ranging in scale from vugs to caves) that are known to be good quality reservoirs (Jiang et al., 2018a; Tian et al., 2018; Fernández-Ibáñez et al., 2019) (Figs. 6, 7-1, 7-2, 8-1, 2 and 9).

(3) Structural movements: During the Late Indosinian paleo-uplift and Yanshanian tectonic movements, regional crustal compressive stresses squeezed the older, deeply-buried rocks. Anticlinal structures, faults, and various fractures, cracks, and micropores were thus formed, which allowed the percolation of hydrocarbons and dissolution fluids via migration channels, the expansion of the hydrocarbon reservoir space, and improved pore interconnectivity, thus enhancing reservoir quality (Hakimi et al., 2012; Tang, 2013; Chen et al., 2016; Al-Aasm and Crowe, 2018; Pontes et al.,

2021; Tang et al., 2022) (Fig. 7-1H, I).

(4) Pressure-solution (stylolites): The Leikoupo Formation (T_2l) is predominantly horizontal or shallow-dipping; stylolites are roughly parallel to bedding and the dissolution seams are often filled with clay minerals, bitumen, and/or organic matter that was mostly deposited during the syn-depositional to shallow-moderate burial stages (Fig. 7-1N and Fig. 9). Sutures and micro-dissolution seams produced by chemical compaction can serve as a conduit for fluid movement, and dissolution joints can serve as oil and gas migration channels (Lønøy, 2006; Jiang et al., 2014; Jiang et al., 2018c). In the study area, dissolution seams and channels post-date the formation of replacive dolomite crystals that were affected by pressure-solution. Stylolitic surfaces contain concentrations of bitumen and scattered dolomite rhomboids, and open stylolite-related microfractures and tension gashes occur adjacent to stylolites (Lønøy, 2006; Al-Aasm et al., 2018; Rosales et al., 2018; Jiang et al., 2021).

(5) Dolomitization: Dolomitization may generate, preserve, or destroy part of the pore spaces associated with macroporosity, and mostly of that associated with microporosity present within host rocks. This process is controlled by the fabric and texture of the host rock being replaced, and the extent depends on the rate, nature, and volume of dolomitizing fluids passing through carbonate sediments (Fu and Qing, 2010; Jiang et al., 2014; Liu et al., 2016a; Jiang et al., 2018a; Jiang et al., 2021; Hao, 2022). In the study area, the observed multiphase dolomite-forming mechanisms include the following: (a) syngenetic or para-syngenetic seepage/reflux of mesohaline

water or seawater in the near-surface syn-depositional stage (Jiang et al., 2018a, c); (b) dolomitization via the mixing of waters during the shallow to moderate burial stage, at temperatures ranging from 80 ˚C to 140 ˚C, which occurred due to the influx of high salinity water that was most likely derived from the overlying formation (Jiang et al., 2016; Jiang et al., 2018a; Hao, 2022); and (c) hydrothermal replacive dolomitization (likely recorded by saddle-shaped dolomite) in the late deeply burial stage, where the fluid source was formed from regional deeply basement-rooted hydrothermal activity zones (140–170 ˚C). The fluids then migrated and were distributed in and around deep-seated thrust-nappe faults, which are structural fractures detected on seismic sections and inferred in the sketch model (Machel and Lonnee, 2002; Guo et al., 2016; Feng et al., 2016; Feng et al., 2017; Al-Aasm and Crowe, 2018; Jiang et al., 2018a; Jiang et al., 2019) (Figs. 7-1, 9, 15, 17). Extensive oil and bitumen inclusions exist in the early diagenetic or burial diagenetic dolomites, which suggests that these dolomites formed before oil charging and bitumen formation (Jiang et al., 2014; Hao, 2022) (Fig. 13).

5.1.1.2 Destructive diagenesis

Compared to carbonate minerals buried to shallow-depth reservoirs, ultra-deep carbonate reservoirs are generally more chemically reactive. The processes involved in their alteration include compaction, cementation, recrystallization, infilling, and replacement:

(1) Compaction: Compaction processes include the mechanical breakage of

grains, particularly elongated allochems (such as larger benthic foraminifera) and chemical suturing along grain contacts, which results in the precipitation of authigenic cements in pore spaces (Ehrenberg and Nadeau, 2005; Wilson et al., 2007; Hakimi et al., 2012; Al-Aasm and Crowe, 2018; Chi et al., 2022). These features are formed during the syn-depositional to shallow–moderate burial stages, and they are developed at depths of approximately 500–1,000 m, where the correlated stylolitization commences in limestones (Wilson et al., 2007; Shen et al., 2017) (Fig. 9). As the burial depth increases, the primary porosity of carbonates decreases and losses are significantly as a consequence of mechanical and chemical compaction (Wei et al., 2017; Jiang et al., 2018c) (Fig. 9).

(2) Calcite cementation: The nucleation and growth of calcite crystals within pore spaces (Fig. 7-1 and Fig. 9). Previous studies have suggested that pressure dissolution is a contributor, or a major causal factor, in calcite cementation during burial diagenesis (Jordan and Wilson, 1994; Neilson et al., 1998; Ehrenberg and Nadeau, 2005; Fu et al., 2008; Hakimi et al., 2012). Cement growth tends to close the gaps between grains, thereby reducing permeability. Pore spaces can be completely filled by cement, which results in lithification of the sediment and a reduction in both porosity and permeability.

(3) Recrystallization: Recrystallization causes in situ formation of new crystal structures that retain the original chemical composition. Dolomite and calcite minerals that undergo recrystallization cause pore-space reductions (Fig. 7-1 and Fig. 9).

(4) Infilling: Infilling in channels is caused by gypsum growth or the

precipitation of pyrite, silica, and/or celestite from hydrothermal fluids or iron mineralization, acidity and Si-rich residual pore water, and/or clay minerals within the matrix (Qing and Nimegeers, 2008; Jiang et al., 2021; Liu et al., 2021b; Li and Cai, 2022) (Fig. 7-1, 2). Solid bitumens commonly occur as infillings in intergranular pores within fractures or at sites of pressure dissolution sites. These bitumens are insoluble in organic solvents and are considered to be pyrobitumen generated at high thermal maturity. The partially solid bitumen in the marine carbonate reservoirs of the Xinchang gas field in the Middle Triassic Leikoupo Formation (T_2l) appear to occur most abundantly in zones with high porosity and permeability, which suggests they are the result of *in situ* crude oil cracking, rather than gas-induced de-asphalting that occurs during the deep burial stage (Hao et al., 2008; Liu et al., 2021b; Hao, 2022). Finally, the infilling is greatly limited by the presence of migrating hydrocarbons, and as pores become filled with a less reactive substances, rock-water reactions are restricted to residual water saturation that coats the pore walls with a thin film (Jordan and Wilson, 1994) (Fig. 7-1, 2 and Fig. 9).

(5) Replacement: This process involves the replacement of mineral grains with a different mineral type (for example, pyrite replacing silica and hydrothermal dolomite replacing calcite minerals), which destroys localized secondary porosity (Chen et al., 2013; Al-Aasm and Crowe, 2018; Liu et al., 2021b) (Fig. 7-1, 2 and Fig. 9).

5.1.2 Comprehensive evaluation of quality and quantity of reservoir petrophysical properties

Conducting a comprehensive assessment of the lithology of a reservoir is important for determining and predicting rock properties, reservoir behavior, and estimating the hydrocarbon production (Jordan and Wilson, 1994; Tang et al., 2022). The combination of helium porosity and permeability, wire-line logging analyses, and MICP measurements enable the main carbonate reservoir rock types, and the microporosity and microstructure to be determined, and the pore structure parameters to be calculated. The results of carbonate rock reservoir property studies have indicated that the carbonate rocks of the Leikoupo Formation are largely heterogeneous. Conventional core plug (helium/MICP) and wire-line logging have yielded different porosity and permeability values (the latter is generally higher) for the same strata. This is likely due to the existence of important open macrofractures or connecting apertures that are either not identified or are damaged during the coring process, but, which have major impacts on the flow of media within the formation (Li et al., 2015; Zhao et al., 2015; Tian et al., 2018) (Fig. 8-2 and Figs.10-1, 2 ,3) (Table 2, 3).

A major challenge when evaluating carbonate reservoirs is to understand the relationship between pore type, porosity, and permeability (Lønøy, 2006; Zhao et al., 2015). Results show that the first to the lower fourth members of the Leikoupo Formation (T_2l^{1-4}) are relatively homogenous (Table 3). The relationship between porosity and permeability has a generally positive trend, as illustrated in Figs. 10-1, 2, 3, which indicates a strong log-linear correlation between both the helium and wire-line logging interpretations of porosity and permeability (Lai et al., 2015; Li et al., 2015; Eysa et al., 2016). However, a few samples show lower-porosity with higher-permeability properties, and this is likely attributed to permeability being enhanced by connective fractures (Lai et al., 2015; Li et al., 2015; Chen et al., 2016) (Figs. 10-1, 2, 3).

The MICP curves show that the analyzed samples present a polymodal pore size distribution (Lucia and Loucks, 2013; Li et al., 2015; Hu et al., 2019; Hu et al., 2020) (Fig. 12). The pore structures exhibit medium coarse to fine pore-throat sizes in T_2l^2, medium coarse to fine pore-throat sizes in T_2l^3, and coarse to large throat sizes in T_2l^4. The MICP analysis indicates that the sorting coefficient classifications are good, good to poor, and poor in samples from the T_2l^2, T_2l^3, and T_2l^4, respectively. The capillary pressure curve varies from gentle (T_2l^4 and T_2l^2) to bold skewness (T_2l^3) (Fig. 11).

The optimal reservoirs performance within the Leikoupo Formation (T_2l) are largely well-developed, with high-quality reservoir features displaying that a locally banded distribution. The best-quality reservoir rocks mainly occur within: (1) the well known unconformity related paleo-karst plane in the uppermost fourth member of the Leikoupo Formation (T_2l^{4a}); and, (2) further down below the unconformity in the epigenetic karstification zone, where there is a conventional tight carbonate reservoir in the first to the Lower fourth members of the Leikoupo Formation ($T_2l^{1\text{-}4b}$) (Fig. 8-2). These are described in greater detail as follows:

(1) Unconformity-related paleo-karstification zones generally have high horizontal permeability and are considered to be important exploration targets in the carbonate reservoirs of the Western Sichuan Depression (Li et al., 2015; Wei et al., 2017; Medici et al., 2021; Hao, 2022). A well-established unconformity-related

epigenetic karstification zone mainly occurs within the uppermost fourth member of the Leikoupo Formation (T_2l^{4a}) and predominantly within the natural gas industry testing interval where secondary solution-enhanced pores, vugs, and holes act as the main pore spaces (Fig. 8-2). The pores have high porosity and permeability ranging from 1.8–14.2%, and 0.2–7.7 mD, respectively (Fig. 6, 10-2) (Supplemental Material 1). Parts of the reservoir interval that have relatively low porosity and permeability have likely been affected by mechanical-chemical compaction and subsequent cementation, which increases with burial depth (Lai et al., 2015; Li et al., 2015). This interval within the studied wells can be described as being a medium-to-excellent, Type I–II, high-quality reservoir. The net pay thickness of the reservoir ranges from 10 m to 200 m (Karakitsios, 2013; Eysa et al., 2016) (Fig. 8-2) (Tables 2, 3).

(2) Further down below the unconformity, there is an important reservoir within the first to lower fourth member of Leikoupo Formation ($T_2l^{1\text{-}4b}$) that has not been given adequate focus to date (Zeng et al., 2008; Chen et al., 2013; Karakitsios, 2013; Jiang et al., 2018b). These strata have effective reservoir pore spaces including primary intergranular pores, intracrystalline pores, secondary solution pores, fractures, and stylolites. These reservoirs are typical low-porosity and low-permeability conventional tight carbonate reservoirs with a helium porosity in the range of 0.6–4.0% and permeability in the range of 0.003–125.2 mD (Fig. 7-1, Fig. 8-1, 2, and Fig.10-1) (Table 3). The reservoir properties of various members are summarized as follows: (i) in the first member of the Leikoupo Formation (T_2l^1), the reservoir quality has been evaluated as being poor to good (Type II–III). It consists of fractured marine

carbonates with an average porosity of 13.0% and a net pay thickness of ~40 m (Alsharhan, 2003; Chen et al., 2018; Wang et al., 2018; Li et al., 2019). (ii) In the second member of the Leikoupo Formation (T_2l^2), the reservoir is of medium to good quality (Type II). The reservoirs are heavily fractured and possess karst pore characteristics. Most of the carbonate reservoirs within the second member of the Leikoupo Formation (T_2l^2) are secondary and post-sedimentary by genesis, and their primary reservoir characteristics were lost during their long geological evolution. They have a net pay thickness of ~30 m (Frolov, 2015). (iii) In the third member of the Leikoupo Formation (T_2l^3), the reservoir quality is of good to excellent quality (Type I–II), and it mainly contains intra/intercrystalline pores, stylolite-related fractures, and open fractures, with a net pay thickness of ~90 m. (iv) In the lower fourth member of the Leikoupo Formation (T_2l^4), the reservoir quality has been evaluated as being medium-to-excellent (Type I–II), with a net pay thickness of ~30 m. Secondary, large-scale dolomite solution-enhanced pore-type reservoirs exist in the lower fourth member of Leikoupo Formation (T_2l^4), which provide sufficient storage space (Ma et al., 2007; Hao, 2022) (Fig.8-2, Figs.10-1, 2, 3) (Tables 2, 3).

A comprehensive analysis of data from seismic surveys and drilling wells demonstrates that the Middle Triassic Leikoupo Formation (T_2l) reservoir is spatially distributed in the Xinchang structural zone and the Longmenshan foreland thrust structural belt and is related to the Wenxing-Miangyan and Guanghan-Zhongjiang slopes. The net pay thickness of this reservoirs ranges from 80 m to 120 m, and the favorable area covers approximately 5,280 km^2 (Chen et al., 2013; Fang et al., 2016;

Atchley et al., 2018; Al-Aasm and Crowe, 2018; Ahmed et al., 2018) (Figs. 1, 2, 3, 15, 17) (Table 3).

5.1.3 Main factors controlling reservoir formation

(1) Paleogeography: Depositional environments, facies, and paleoclimate predominantly control the distribution of favorable reservoirs development (Eysa et al., 2016; Feng et al., 2017; Atchley et al., 2018; Rangkey, 2020; Pontes et al., 2021). Most of the reservoirs in the Middle Triassic Leikoupo Formation (T_2l) were formed in a low-energy, well-oxygenated, shallow-sea shelf setting of a carbonate platform, where there was limited evaporation and a lack of tides, but abundant well-developed microorganisms. This resulted in the formation of microbialites, microbial reefs, and oolitic dolomites or dolograinstones within the platform-margin shoals. Meanwhile, the majority rocks comprising the reservoir lack a diversity living creatures of trace fossils, which probably indicates restricted waters or a higher salinity as the result of an arid climate that dominated the depositional setting (Ma et al., 2007; Sonnenberg and Pramudito, 2009; Liu et al., 2016a; Jiang et al., 2018a, b, c) (Figs. 3, 5, 6, and Fig. 7-1, 2).

(2) Epigenetic karstification: Erosion due to paleo-karstification can also enhance the reservoir properties associated with prolonged and aggregated exposure (Feng et al., 2013; Eysa et al., 2016; Pontes et al., 2021). The Luzhou and northeastern edge of the ancient Kaijiang uplifts gradually formed due to the Early Indosinian movement during the Middle to Late Triassic as the seawaters receded

along the eastern margin of the depression, and approximately 10 myr of erosion and karstification resulted in the development of a regional unconformity (Xu et al., 2011). The unconformity-related epigenetic karstification zone, which occurs largely in the uppermost fourth member of Middle Triassic Leikoupo Formation (T_2l), developed a weathering crust and paleo-karstification reservoirs (Liu et al., 2016a) (Figs. 3, 5, 6, 8-1, 2 and 15).

(3) Burial diagenesis: Burial diagenetic events and processes are also among the most important factors influencing reservoir properties (Lai et al., 2015; Makeen et al., 2016; Wei et al., 2017; Rosales et al., 2018). The reservoir quality was affected by a series of constructive and destructive diagenetic processes that occurred in syn-depositional, shallow-moderately burial, and deeply burial diagenetic environments (Figs. 6, 7-1, 2, 8, and 9). The previous discussion demonstrates that dolomitization and sulfate reduction reactions (e.g., BSR and TSR) were predominantly responsible for the formation of solution-enlarged pores, vugs, micropores, and microfractures during deeply burial (Jiang et al., 2018b; Hao, 2022).

(4) Structural movements: During the Indosinian and Yanshanian periods, there was movement of corrosive fluids associated with regional tectonic stresses or other related mechanisms linked to multiple stages of deep-seated strike-slip thrust faulting and fracturing activities along the basement (Jiang et al., 2016; Jiang et al., 2021). These events resulted in the origination and flux of hydrothermal mineral fluids flowing (including oil and gases), as well as structural deformation that could directly increase or decrease rock permeability, which will enhance or impede fluid flow

respectively. Structural movements played a fundamental role in influencing the characteristics of the reservoirs within the Western Sichuan Depression (Guerriero et al., 2013; Tang, 2013; Mansurbeg et al., 2016; Jiang et al, 2018b; Rangkey, 2020; Pontes et al., 2021; Chi et al., 2022) (Figs. 3, 4 and 14).

5.2 Seals, overburden rocks, and traps

5.2.1 Seals

Hydrocarbon preservation conditions are one of the critical factors controlling hydrocarbon exploration (Downey, 1994; Alsharhan, 2003; Zhao et al., 2014; Hu et al., 2018; Jones et al., 2019; Wang et al., 2022). Regional seals (also known as caprocks) in the form of shale or mudstone intervals overlie oil or gas reservoirs. These are geological formations that have extremely low porosity and permeability, and they constitute a barrier against hydrocarbons flowing into the overlying layers. Their sealing behavior and capacity is heavily influenced by unit thickness (Downey, 1994; Demirel, 2004; Schmitt et al., 2013; Shalaby et al., 2013; Frolov, 2015; Meng et al., 2015; Makeen et al., 2016). The ultra-deeply buried Middle Triassic Leikoupo marine carbonate petroleum system is thought to be principally preserved by vertical seals, which are mainly low-permeability pelitic argillaceous continental sediments, including interbedded successions of shale and mudstones of the Late Triassic Xujiahe Formation (T_3x). The thickness of T_3x is highly variable, but reaches 300 m across the region, and the formation displacement pressures range from 10.1 Mpa to 51.2 Mpa. The enclosed hydrocarbon height of the reservoir is approximately

200–1100 m, and the rocks comprising the seal typically experience abnormal overpressure conditions with a pressure coefficient of 1.2 – 2.2 (Downey, 1994; Liu et al., 2016a). Additionally, the multiple bedded evaporate anhydrite interlayers within the Leikoupo Formation (T_2l) may also provide a certain degree of regional sealing ability (Chen et al., 1994; Downey, 1994; Jiang et al., 2014; Jiang et al., 2018a; Li et al., 2022).

5.2.2 Overburden rocks

The overburden rock covers and overlies the three essential petroleum elements: the source, seal, and the reservoir rock (Magoon and Dow, 1994; Magoon et al., 2001). The sealing capacity is further enhanced by the gravity of the huge thickness of continental overburden rocks (~5000 m) in the Western Sichuan Depression, and the amount of overburden pressure has a significant influence on the maturation of source rocks and the transformation of organic matter (Hakimi et al., 2012). These overburden rocks, which include the entire Jurassic (J) to Quaternary (Q) stratigraphic succession, were rapidly deposited in lacustrine environments (Fig. 3). The formation waters were enriched in $CaCl_2$, which created favorable conditions for hydrocarbon entrapment and accumulation (Zhang et al., 2007; Xu et al., 2013; He et al., 2017) (Fig. 16 and Fig. 17). Furthermore, it is of note that among the overburden rock series, the upper source rock intervals of the Late Triassic Xujiahe Formation are an unconventional reservoir with a hydrocarbon concentration sealing ability that enhanced functions of preservation during the formation of the Middle Triassic

Leikoupo Formation petroleum system (Fu et al., 2003).

5.2.3 Traps

The interpretation of seismic reflection profiles reveals complex and variable structural geometries that act as effective traps. The trap types are predominantly structural or stratigraphic, or a combination of the two types (Peters et al., 2005; Magoon et al., 2006; Zhang et al., 2007; Feng et al., 2013; Meng et al., 2015) (Figs. 15 and 17). A reconstruction of the structural evolution of the region shows that the northeast was uplifted sharply, while the southern portion dips gently toward the north (Li et al., 2015) (Figs. 4, 15, 17). The major tectonic events that controlled the development of basin and trap formation occurred from the Middle Triassic (T_2) to the present, and these can be divided into three developmental stages: (1) during the Indosinian tectonic movement (Middle–Late Triassic), the area underwent a large degree of uplift that led to the development of mountain belts; (2) during the Yanshanian tectonic movement: there was significant uplift, hydrocarbon traps gradually developed, natural gas was charged and entrapped; and, (3) during the Himalayan tectonic movement: structural deformation shaped the final geometry of the basin and hydrocarbon (natural gas) resources accumulated in traps (Xu and Zhao, 2010; Beglinger, 2012) (Figs. 3, 4, 15, 16, 17).

5.3 Hydrocarbon generation, migration and charging

5.3.1 Hydrocarbon generation process and resource potential

The proposed evolutionary processes and establishment of the key petroleum system elements in the Western Sichuan Depression relates to the generation, migration, charging, and accumulation of hydrocarbons within traps at multiple stratigraphic levels that were primarily controlled by regional tectonic events (Zhao, 1990; Deming, 1994; Zhang et al., 2008; Katz and Everett, 2016; Liu and Katz, 2016; Sachse et al., 2016; Sun et al., 2017; Craig et al., 2018) (Fig. 16).

Based on regional 1D TSM Basin modeling (software used was a hydrocarbon resource deterministic numerical simulation and assessment system that was developed by SINOPEC) of the histories of subsidence, burial, and thermal evolution, and the acquired kinetic and geochemical data, it can be concluded that the source rocks experienced adequate rapid burial (maximum burial depths of approximately 8,000–10,000 m at ~120 Ma), where maximum temperatures reached approximately 250 °C at ~65 Ma. From approximately 220 Ma to 60 Ma, three major hydrocarbon generation events took place at high temperatures and pressures environment (Deming, 1994; Hao et al., 2008; Liu and Katz, 2016; Sachse et al., 2016; Xu et al., 2017; Sun et al., 2020; Hao, 2022) (Fig. 16): (1) the kerogen began to generate crude oil and accumulate into paleo-reservoirs during early maturity stage (0.5%< Ro < 1.3%), then the gradual increase in geothermal temperatures (160~220 °C) was accompanied by crude oil cracking, which led to formation of gases from pre-existing paleo-reservoirs until residual solid bitumen be left (Hill et al., 2007; Jiang et al., 2018a; Zhu et al., 2020; Hao, 2022) (Fig. 7-1, Fig. 16); (2) wet-gases were produced, and/or the secondary thermal cracking of liquid hydrocarbons into gases occurred in the late maturity stage (1.3 < Ro < 2.0%); (3) dry-gases were directly generated from the kerogen during the advanced maturity stage (Ro > 2.0%). In this respect, a huge chemical reaction occurred that converted the gases from the organic matter within a high temperature and pressure environment, with this occurring in a complex geological structure (Figs. 1, 2, 3, 4). These three successive hydrocarbon generation processes were identified in the study area within multiple sets of source rocks and they enabled sufficient material to be supplied as the foundations of a medium-to-giant gas field accumulation (Peters and Cassa, 1994; Liao et al., 2013; Frolov, 2015; Zheng et al., 2015; Li et al., 2019; Sun et al., 2020) (Fig.16). According to the 3D TSM Basin modeling results of Xu et al. (2013), the natural gas generation intensity of the four source rock units has reached approximately (10–80) $\times 10^8$ m^3/km^2, and the potential resource reserve volume of the Middle Triassic Leikoupo Formation petroleum system is estimated to be 0.9839×10^{12} to 1.201×10^{12} m^3. Therefore, these multiple sets of source rocks have supplied abundant hydrocarbons that enabled a medium-to-giant natural gas field accumulation (Xu et al., 2012; Xu et al., 2017; Liu et al., 2020; Sun et al., 2020).

5.3.2 Hydrocarbon charging and accumulation

Hydrocarbon charging is an episodic but long-lasting process (Jiang et al., 2021). The analysis of saline aqueous fluid inclusions in calcite crystals revealed that the homogenization temperatures can be grouped into two phases: at 98 °C to 130 °C and 130 °C to 171 °C, respectively, which enables the main critical moments of hydrocarbon emplacement history to be constrained. Two main hydrocarbon charging phases occurred, and this is supported by the micro-thermometric data sourced from well CK1 (ranges: 100 °C to 145 °C and 165 °C to 175 °C) and those measured in the Pengzhou, neighboring Zhongba gas field (ranges: 110 °C to 130 °C and 130 °C to 150 °C) in the Western Sichuan Depression (Neilson et al., 1998; Zhang et al., 2007; Qing and Nimegeers, 2008; Hakimi, 2012; Tang et al., 2013; Jiang et al., 2018a; Jiang et al., 2019; Liu et al., 2020) (Fig. 14). Combined with structural geologic and seismic profiles across wells, primary liquid hydrocarbons and early kerogen generating gases accumulated during the first charging stage, which formed a paleo-reservoir during the Indosinian paleo-uplift structural movement from 220 Ma to 170 Ma (Late Triassic–Early Jurassic). In the second charging stage, enormous volumes of crude oil underwent cracking, and kerogen thermogenic gases accumulated continuously during the Yanshanian structural movements from 130 Ma to 90 Ma (Early–Late Cretaceous) (Zhao et al., 1996; Xu et al., 2013; Meng et al., 2015; Xiang et al., 2015; Zheng et al., 2015; Guo et al., 2021) (Figs. 3, 14 and 16). The migration forces were driven by: (i) stratigraphic overpressure (related to sediment compaction); (ii) fluid flow hydrodynamic abnormal pressure (produced during hydrocarbon generation and/or increasing association with TSR) (Chi et al., 2022); and, (iii) buoyancy forces, together with the main reservoir-forming processes, natural gas migration, and accumulation, which mainly taken place within the nearby source rocks (Magoon et al., 2005; Chi et al., 2010; Chen et al., 2013; Lai et al., 2015; Hu et al., 2020; Jiang et al., 2021; Medici et al., 2021; Pang et al., 2021).

Hydrocarbons generated in the Permian and Middle to Late Triassic source rock assemblages were accompanied by hydrothermal fluids (direct evidence includes widely distributed indicator minerals, such as fluorite, pyrite, celestite, sphalerite, and saddle-shaped dolomite) that traveled primarily via: (i) vertical migration along a complex pathway system composed of connective pores with throat channels, in addition to open network fault-fracture flow pathways formed by local tectonic movements (Demaison and Huizinga, 1994; Guerriero et al., 2013; Liu and Katz, 2016; Jiang et al., 2021; Pontes et al., 2021; Chi et al., 2022) (Fig. 7-1, Fig. 17); and (ii) subsequent long-range, low-angle to lateral migration through the paleo-karstification unconformity plane and carrier beds, which enabled efficient accumulation into favorable tectonically altered and other types of effective traps. This enabled the formation of large- or medium-scale commercial petroleum accumulations in the Western Sichuan Depression (Zhang et al., 2005; Cao et al., 2011; Hackley and Karlsen, 2014; Xiang et al., 2015; Baur and Katz, 2018; Nesheim, 2019; Jiang et al., 2021) (Fig. 17). Finally, natural gas accumulation experienced further dynamic adjustment and transformation during Himalayan tectonism, where there was movement into the structural-lithological combination traps of the current enrichment area in slope and uplift zone (Xu and Zhao, 2010; Xu et al., 2013; Zheng et al., 2015; Guo et al., 2021; Hao, 2022) (Figs. 2, 8-2, 17).

The relationship between Middle Triassic Leikoupo petroleum elements, such as source rocks, reservoirs, seals, overburden rocks and traps, and the entire accumulation processes, are summarized in Figs. 15, 16, and 17 (Demaison and Huizinga, 1994; Peters et al., 2006; Magoon et al., 2005; Katz et al., 2016). The estimated reserves calculated from the preliminary study area are determined as being 300×10^9 m^3 (Zeng et al., 2008; Chen et al., 2013; Guo et al., 2021).

In summary, the known ultra-deeply buried Middle Triassic Leikoupo marine carbonate petroleum system (!) possesses great potential, and it is thus an important exploration target within the Western Sichuan Depression. The discovery of hydrocarbons sourced from ultra-deeply buried microbial carbonates associated with paleo-karstification and/or strong structural movements in the study area strengthen the supposition that bound hydrocarbons will be able to be produced from giant carbonate reservoirs. It is crucial that further research and exploration resources are employed within similar deeply or ultra-deeply buried basins in China (e.g. Dengying Formation of the upper Sinian and lower Cambrian of the Tarim Basin) and globally (e.g. Precambrian carbonate of Siberian platform, Mississippian and Permian Formation of the North America, Triassic Khuff and Kanggan formations and Jurassic Arab Formation on the Arabian plate etc.).

6 Conclusions

(1) The analysis of the source rock to gas correlations, carbon and hydrogen isotope and He–Ne–Ar noble gas isotope components show that the Middle Triassic Leikoupo oil-associated gases mainly originated from four source rock units of

sedimentary crust that have the following associated qualities: (i) 30−120 m of carbonaceous interbedded shales and dark gray muddy limestones (Type II−III) of the underlying the Permian Longtan/Wujiaping Formation (good to excellent); (ii) ~384 m of algal-rich self-sourced dolomites (Type II) in the Leikoupo Formation (fair to good); (iii) ~10 m of gray limestones (Type II) in the Maantang Formation (poor to fair); and (iv) ~84 m of shales (Type II−III) in the Xiaotangzi Formation (moderate). The vitrinite reflectance ratio (%Ro: 1.0~3.0%) and T-max (462−582 °C) values suggest that organic matter has reached the main stage of hydrocarbon generation.

(2) The major lithologies that comprise the reservoirs include argillaceous algal dolomites, dolograinstones, crystalline dolostones, limestones, and thrombolitic microbial dolomites. The reservoir properties exhibit extreme heterogeneity due to differences in the paleogeographical setting and mutual interactions between constructive diagenesis (e.g., epigenetic karstification, faulting and fracturing, and dissolution) and destructive diagenesis (e.g., physical or chemical compaction, recrystallization, dolomitization, calcite cementation, replacement, pyritization, celestite precipitation, and infilling).

(3) An unconformity-related epigenetic karstification zone was identified in the uppermost fourth member of Leikoupo Formation. This is well-developed due to secondary solution-enhanced pores, vugs, and holes, which results in higher porosity (1.8–14.2%) and permeability (0.2–7.7mD). Further below the unconformity, the reservoirs are much tighter and characterized by primary intergranular pores, intracrystalline pores, solution pores, fractures, stylolites, and micropores with low

porosity (0.6–4.1%) and permeability (0.003–125.2 mD). The reservoir thickness ranges from 60 m to 180 m and covers an approximate area of 5,280 km^2 based on wire-line logging interpretation and seismic surveys.

(4) The regional seals comprise mudstones of the Late Triassic Xujiahe Formation with a thickness of ~300 m, and their sealing preservation capacity has been further strengthened by the continental facies overburden rocks with thicknesses reaching ~5000 m. Furthermore, the upper source rock interval of the Late Triassic Xujiahe Formation has a hydrocarbon concentration sealing ability and it provides substantial protective functions for hydrocarbon accumulation. Effective traps are dominated by a combination of structural-lithological typing.

(5) One-dimensional modeling of the subsidence, burial, and thermal histories suggest that hydrocarbon generation occurred between 220 Ma and 60 Ma. The kerogen began to generate crude oil and accumulate into paleo-reservoirs during the early maturity stage (0.5% < Ro < 1.3%), then gradually increasing geothermal temperature (160~220 °C) conditions were accompanied by crude oil cracking, which led to the formation of gases from pre-existing paleo-reservoirs. The wet-gases were produced and/or secondary thermal cracking of liquid hydrocarbons into gases occurred during the late maturity stage (1.3% < Ro < 2.0%), whereas the dry-gases were directly generated from kerogen during the advanced maturity stage (Ro > 2.0%). These three successive hydrocarbon generation processes supplied sufficient material for gas field accumulations.

(6) The homogenization temperatures of the hydrocarbon-associated aqueous

fluid inclusions ranged from 98–130 °C and 130–171 °C; these data were combined with structural and seismic profiles across wells PZ1-XQS1-CK1-XCS1-TS1, and a two stage hydrocarbon charging period was interpreted to have occurred from 220–170 Ma and 130–90 Ma, respectively. Formation overpressure, fluid flow hydrodynamic abnormal pressure, and buoyancy forces were effectively coupled to accelerate hydrocarbon migration and accumulations via unconformities and interconnected fault-fracture networks that were developed during the Indosinian and Yanshanian orogenies. The natural gas accumulations experienced further dynamic adjustment and transformation during the ongoing Himalayan orogeny, where the predicted estimated reserves reached ~300×10^9 m^3.

In summary, multidisciplinary approaches were used to characterize the ultra-deeply buried Middle Triassic Leikoupo marine carbonate petroleum system (!). These results not only have a practical application for hydrocarbon resource exploration and compiling exploitation risk assessment strategies, but they are also provide excellent analogous implications for similar sedimentary basin studies in China and elsewhere worldwide. It is believed that there are abundant deeply buried hydrocarbon resources yet to be discovered in future.

Acknowledgements

We would like to express our sincerely gratitude to those hardworking researchers, colleagues and kind friends that could cooperated and supported each others during the COVID-19 worldwide pandemic challenge moment. This research work was jointly financially supported by grants from the Special Key Discipline-Geological Resources and Geological Engineering Scholarship (No. 11000-13Z00703) of Chengdu University of Technology, China, the open funding for the Provenance Analysis of the Paleogene Strata in Nima Basin, Tibet: Constraints on the tectonic uplift from the State Key Laboratory of Oil and Gas Reservoir Geology and Exploration (No. PLC20180504), and Oil and Gas Plays Accumulation and Enrichment Mechanisms in the Sichuan Basin Research Program. We sincerely express our gratitude to China Exploration Company, SINOPEC for providing access to data, sample collections and supporting laboratory facilities as well as for permission to publish this study. We also want to thank for various researchers from in the Sedimentary Laboratory in the Department of Geology of University of Regina; Saskatchewan Geology Survey, Saskatchewan Ministry of Energy and Resource, Canada; College of Geosciences and Technology, Southwest Petroleum University, China for supplying literature and providing their constructive suggestions. This manuscript also has benefited greatly from communication and discussions with Professor Stephen L. Bend, Professor Guoxiang Chi, Chao Yang, Professor Hans G. Machel, Professor Michael A. Abrams, Professor David Leary, Dr. Ziguo Hao, Professor Zuowei Hu, Professor Jingyou He, Professor Zhongtang Su, Professor Weiming Wang, Professor Jingming Song, Professor Kun Li, Professor Yinghui Zuo, Professor Bo Yang, Dr. Yue Hao Ye, Morteza Rabiei, Dr. Siyang Zhang, Dr. Ziye Lu, Dr. Teng Deng, Dr. Jennifer Burton, Dr. Yong Liu, Dr. Hailong Meng, Dr. Zhiyuan Chen, Dr. Haotian Zhang, Dr. Yurui Zhu, Dr. Wenjie Li, Dr. Yuhao Fu, Dr. Chongyang

Xiao, Dr. Zhiyao Xian, Dr. Mabi A.W., Dr. Dongyu Li, Dr. Kuizhou Li, Dr. Yang Liu, Qi Li, Dr. Guoqian Wang, Hang Ying, Jing Li, Miseziha, Tingping Ma, Jun Liu and Dr. Ye Tao. Finally, we sincerely appreciate the journal staff Horscroft, Jennifer Buisan, Joshua Emmanuel Timkang, Fernando Pasicolan had provided research supports warmly, anonymous reviewers and Professor Lei Jiang, Professor Mingyou Feng, Dr. Mengwei Zhao for their extraordinary constructively critical review comments, associate editor Dr. Barry J. Katz from Chevron Energy Technology Company, Houston, Texas, USA, editor Dr. Max Qinhong Hu in University of Texas at Arlington, USA, helped significantly improve and instruct the manuscript.

Captions for figures, tables, and Supplementary material data

Figures

Fig. 1 (A) Location map of the study area (China base map, after China National Bureau of Surveying and Mapping Geographic information. Note: SCSI = South China Sea Islands); (B) Simplified geologic map of the Western Sichuan Depression, China. Structural units: I. Western Sichuan Depression; II. Micangshan uplift; III. Longmenshan fold belt; IV. Emeishan-Liangshan fold belt; V. flat belt in central of the Sichuan Basin (Modified from Chen et al., 1994; Li et al., 2009; Feng et al., 2015; Jiang et al., 2018a; Jiang et al., 2019; Sun et al., 2020).

Fig. 2 Outline location map of structural units and representative producing wells of the Middle Triassic Leikoupo Formation (T_2l) in the Western Sichuan Depression, China. Modified from Xu et al. (2013), Meng et al. (2015), Li et al. (2016), and Su et al. (2020).

Fig. 3 Chart summarizing regional tectonic and stratigraphic history and the main petroleum play elements of the western Sichuan depression, Southwest China (note: Sinian ≈ Ediacarian geological period; sourced from the International Union of Geological Sciences (IUGS)) (Compiled from Zhang et al., 2007; Hao et al., 2008; Zhang et al., 2008; Wang et al., 2014).

Fig. 4 General structural geologic profiles along AA1, which summarize the main thrust–fold belt tectonic reconstructions and the evolution of hydrocarbon accumulation phases that controlled the petroleum system in the Western Sichuan Depression, China (Compiled from Zhang et al., 2008).

Fig. 5 Composite stratigraphic columns with organic geochemical characteristics of source rocks from the Middle–Late Triassic formations sampled from the scientific exploration well CK1 in the Western Sichuan Depression, China (Referenced and slightly modified from Peters and Cassa,1994; Sun et al., 2020).

Fig. 6 (A) Field outcrop photograph of the Middle Triassic Leikoupo Formation (T_2l) in Hanzeng, Jiangyou in the Western Sichuan Depression, showing a predominantly gray, heavily fractured, medium to thick-bedded dolomite; (B) dark-gray, dolomitized limestone with porosity and permeability of 1.8% and 0.2 mD, respectively, T_2l^4, well PZ1, 5,767.37–5,767.46 m; (C) gray dolostone, solution vugs and holes with porosity and permeability of 14.2% and 7.7 mD, respectively, T_2l^4, well PZ1, 5, 818.22–5,818.33 m; (D) gray, microbial dolomite containing solution pores and vugs with a porosity and permeability of 11.4% and 7.4 mD, respectively, T_2l^4, well PZ1, 5, 818.56–5,818.66 m; (E) dolomite with dark bedding and honeycomb-like gray, intercrystalline pores and intercrystalline solution pores, vugs and holes, T_2l^4, well XCS1, 5,730.00 m; (F) silty, stromatolitic arenaceous dolostone with a pancake shape that mainly developed fractures and needle-like solution pores, T_2l^4, well TS1, 5,742.00–5,742.10 m; (G) silty, arenaceous microbial stromatolite dolostones with fractures and micropores, T_2l^4, well TS1, 5,749.60 m.

Fig. 7-1 Photomicrographs of representative thin sections from the Middle Triassic Leikoupo Formation (T_2l), showing typical reservoir lithology and reservoir pore space characteristics (wells YS1, PZ1, XCS1, and CK1). (A) Thrombolitic dolomite, solution pores are located between the thrombolite frameworks, T_2l^4, well YS1, 6,216.22 m; (B) dolomitized thrombolite with intracrystalline pores, T_2l^4, well YS1, 6,227.59 m; (C) dolomitized stromatolite with solution pores partially filled with celestite, T_2l^4, well YS1, 6,224.72 m; (D) interparticle and intraparticle solution pores, T_2l^4, well PZ1, 5,826.20 m; (E) lamellar sandy dolomite with intraparticle pores and microfractures, pore width ranges from 0.05 mm to 0.5 mm, T_2l^4, well PZ1, 5,827.28

m; (F) finely-crystalline, sandy-bearing dolomite with interparticle pores ranging from 0.02 mm to 0.15 mm, T_2l^4, well XCS1, 5,750.00 m; (G) fine-grained argillaceous limestone with bioclasts, granules and sandy grains; microfractures are unfilled, with widths ranging from 0.01 mm to 0.02 mm, T_2l^2, well CK1, 6,610.26 m; (H) micritic limestone with three-stages fracturing: Fracture I types are filled with calcite and ranges from 0.1 to 0.25 mm in width; Fractures II types are unfilled; Fracture III types are microfractures filled with calcite cement and crosscuts the two previous types of fractures; local microfractures and main fractures are interconnected to form an effective reservoir network, T_2l^2, well CK1, 6,388.73 m; (I) bioclastic packstone with sand grains, foraminifera, and radiolaria, average grain size of 0.4 mm. Sample includes two unfilled fractures: the main fractures on the left side of the picture are divergent and crosscut by three microfractures with widths ranging from 0.01 mm to 0.20 mm; the fractures on the right side of the picture are 0.45 mm wide, T_2l^2, well CK1, 6,608.38 m; (J) paleo-karst breccias, dolomite and microcrystalline gypsum; gypsum and calcite veins are associated with dolomitization, T_2l^3, well CK1, 6,215.31 m; (K) fine to coarsely crystalline ferruginous limestone; calcite crystals are euhedral or subhedral with sizes ranging from 0.2 mm to 0.3 mm. Pyrite crystals are square or rectangular; maximum diameter is 1.5 mm, with an average size range from 0.3 to 0.6 mm, T_2l^2, well CK1, 6,383.88 m; (L) celestite and hydrothermal saddle dolomite veins, T_2l^1, well CK1, 6,897.00 m; (M) microcrystalline dolomite containing coarsely crystalline gypsum and stylolites with organic matter, T_2l^4, well CK1, 5,929.24 m; (N) recrystallization along stylolites, T_2l^2, well CK1, 6,392.00 m; (O) micritic limestone with stylolites and hydrothermal dolomite with micro-fractures, T_2l^3, well CK1, 6,224. 84 m.

Fig. 7-2 Photomicrographs of representative thin sections from the Middle Triassic Leikoupo Formation (T_2l^4), showing typical reservoir lithology and reservoir space characteristics (wells TS1 and YS1). (A) Silty calcareous dolostone, with intercrystalline solution pores (+), T_2l^4, well TS1, 5,741.80 m; (B) calcareous, finely-crystalline dolostone with solution pores and vug development (-), T_2l^4, well TS1, 5,743.00 m; (C) calcareous, finely-crystalline dolostone with intergranular solution pores and vugs (+), T_2l^4, well TS1, 5,749.80 m; (D) silty calcareous dolostone that has needle-like, intercrystalline solution micropores, T_2l^4, well TS1, 5,745.00 m; (E) patchy, finely-crystalline dolostone, intergranular solution with micro-fracture pore spaces (+), T_2l^4, well TS1, 5,754.00 m; (F) finely-crystalline dolostone with intercrystalline and solution pore spaces (-), T_2l^4, well TS1, 5,754.20 m; (G) calcareous, finely-crystalline dolostone, solution fractures with partial silica infilling (+), T_2l^4, well TS1, 5,755.40 m; (H) calcareous, finely-crystalline microbial dolostone with solution pores and fractures, and less common interparticle pores (-), T_2l^4, well TS1, 5,756.50 m; (I) microfractures infilled by gypsum (+), T_2l^4, well YS1, 6,191.00 m; (J) solution pore spaces filled with medium-coarse calcite cements or silica in addition to microfractures (+), T_2l^4, well YS1, 6,191.20 m.

Fig. 8-1 Scanning electron microscope images of pore space textures within samples from the Middle Triassic Leikoupo Formation (T_2l). (A) Intercrystalline micropores in dolomite, T_2l^4, well PZ1, 5,814.70 m; (B) solution micropores and micro-fratures with widths ranging from 0.005 mm to 0.02 mm, T_2l^4, well XQS1, 5,900.00 m; (C) intraparticle and intercrystalline solution micropores around euhedral dolomite crystals, T_2l^4, well PZ1, 5,807.70 m; (D) intergranular solution pores (sample surface is unpolished), T_2l^4, well PZ1, 5,830.00 m; (E) microfractures, T_2l^4, well YS1, 6,191.00 m; (F) intercrystalline solution pores among quartz, dolomite, and calcite, T_2l^4, well YS1, ~6,191.20 m; (G) intercrystalline pores and solution micropores, T_2l^4, well YS1, ~6,191.30 m; (H) intergranular and intercrystalline solution pores, T_2l^4, well YS1, 6,191.43 m.

Fig. 8-2: Wire-line logging interpretation across wells PZ1-XQS1-CK1-XCS1-TS1 from the Late Triassic Maantang Formation to the fourth member of Middle Triassic Leikoupo Formation including the unconformity-related epigenetic karstification zone, reservoir features, and natural gas industry testing results (sourced from Southwest Branch Company, SINOPEC).

Fig. 9 Paragenetic sequence of the diagenetic processes of the Middle Triassic Leikoupo Formation (T_2l) in the Western Sichuan Depression, China. The diagram illustrates the three main diagenetic stages that are divided in terms of burial history (Wilson et al., 2007; Chen et al., 2013; Feng et al., 2015; Al-Aasm and Crowe, 2018; Al-Aasm et al., 2018; Jiang et al., 2018c; Liu et al., 2021b; Jiang et al., 2021).

Fig. 10-1 Helium porosity and permeability characterized using a logarithmic correlation for carbonate reservoir rocks from the Middle Triassic Leikoupo Formation ($T_2l^{2,\,3,4\,b}$), well CK1.

Fig. 10-2 Helium porosity and permeability characterized using a logarithmic correlation for carbonate reservoir rocks from the unconformity-related epigenetic karstification zone of the uppermost Middle Triassic Leikoupo Formation (T_2l^{4a}), wells PZ1, TS1.

Fig. 10-3 Wire-line logging interpretation of porosity and permeability characterized using a logarithmic correlation for carbonate reservoir rocks from the Middle Triassic Leikoupo Formation ($T_2l^{1\text{-}4}$), well CK1.

Fig. 11 Cross plot of sorting coefficient (X axis) and skewness (Y axis) for carbonate reservoir rocks of the Middle Triassic Leikoupo Formation (T_2l) in well CK1.

Fig. 12 Cross plots of mercury injection capillary pressure curves, pore-throat sizes, and porosity-permeability relationships for different rock types from the carbonate reservoirs of the Middle Triassic Leikoupo Formation (T_2l), well CK1, Western Sichuan Depression, China (Li et al., 2015; Zhao and Chen, 2015; Loucks and Dutton, 2019; Wen et al., 2023).

Fig. 13 Transmitted-light photomicrographs of petrography fluid inclusions, well PZ1. (A) Dolostone with brown liquid (±60%) and dark gray gas (±40%) hydrocarbon inclusions associated with calcite cements that infilled in fractures and holes during late stage diagenesis; the frequency of grains containing oil inclusions is greater than 20%, which implies that the calcite formed before fracture formation and hydrocarbon charging, 40 × (-), T_2l, 5,766.60 m; (B) yellow-gray aqueous inclusions, brown oil-bearing inclusions, and dark-gray gas hydrocarbon inclusions exhibiting necking and dendritic type networks, where the homogenization temperature of aqueous inclusions T_h = 120 ˚C, 40 × (-), T_2l, 5,766.60 m; (C) yellowish-gray aqueous inclusions and brown liquid hydrocarbon inclusions with grouped occurrences in the white calcite veins, the frequency of grains containing oil inclusions is greater than 30%, T_h = 133 ˚C, 63 × (-), T_2l, 5,814.55 m; (D) liquid-dominated aqueous fluid inclusions distributed in random populations, 63 × (-), T_2l, 5,814. 00 m; (E) dolomite with dark-gray, gas-liquid, two-phase inclusions distributed into late diagenetic calcite filling fractures and holes; the frequency of grains containing oil inclusions is greater than 20%, 40 × (-), T_2l, 5,819.50 m; (F) an assemblage of primary two-phase aqueous inclusions occurring in calcite overgrowths, T_h = 165 ˚C, 63 × (-), T_2l, 5,819.50 m.

Fig. 14 Histograms illustrating homogenization temperatures (T_h) for saline aqueous fluid inclusions in calcite crystals in the Middle Triassic Leikoupo Formation (T_2l) from wells XCS1, XQS1, and PZ1.

Fig. 15 Seismic profiles across wells PZ1-XQS1-CK1-XCS1-TS1, showing the unconformity-related paleo-karst plane (dashed red line: T_6), situated between the Middle Triassic Leikoupo (T_2l) and the Late Triassic Maantang Formations (T_3m), Western Sichuan Depression, China.

Fig. 16 Burial history, thermal evolution, and hydrocarbon generation history curves of the Middle Triassic Leikoupo marine carbonate reservoir, presented as a migration, charging and accumulation event chart showing the essential petroleum system elements and processes in the Western Sichuan Depression, China (referenced and modified from Magoon et al., 2005; Katz et al., 2016; and Sun et al., 2020).

Fig. 17 Sketch geological model showing the history of hydrocarbon migration and accumulation processes of the Middle Triassic Leikoupo (T_2l) marine carbonate reservoir in the Western Sichuan Depression, China (modified from Pu, 2014; Meng et al., 2015; Xie et al., 2015; Liu et al., 2020; and Su et al., 2022).

Tables

Table 1 Compilation of source rock parameters used for petroleum system evaluation in the Western Sichuan Depression, China.

Table 2 Criteria used to evaluate marine carbonate reservoirs of the Sichuan Basin, China (Chen et al., 2013; Li et al., 2015).

Table 3 Comprehensive evaluation of qualitative and quantitative reservoir characteristics of the Middle Triassic Leikoupo Formation (T_2l) in the Western Sichuan Depression, China.

Supplementary material data

Supplementary Material 1. Helium porosity and permeability determined for the Middle Triassic Leikoupo Formation (T_2l) from drilling cores (plugs), Wells CK1, PZ1, and TS1.

Supplementary Material 2. Quantitative petrophysical, fractal dimensional, and pore-structural parameters determined by mercury injection capillary pressure measurements of samples from the Middle Triassic Leikoupo Formation (T_2l), Well CK1.

Supplementary Material 3. Interpretation of porosity and permeability using wire-line logging for the Middle Triassic Leikoupo Formation (T_2l), Well CK1 (data collected from the China Exploration Company, SINOPEC).

Supplementary Material 4. Homogenization temperatures of saline aqueous inclusions that occur in calcite and dolomite samples of the Middle Triassic Leikoupo Formation (T_2l) from Wells XCS1, XQS1, and PZ1.

References

Ahmed, A. E., K. Mohamed A, and A. E. Abass, 2018. Reservoir characterization utilizing core and wire-line logging data for Kareem sandstone, Ashrafi oil Field, Gulf of Suez, Egypt. Egyptian Journal of Petroleum, 27: 1013–1027.

Akinlua, A., 2012. The role of analytical chemistry in Niger Delta petroleum exploration: a review. Analytica Chimica Acta, 730: 24–32.

Akintunde, O. M., C. C. Knapp, and J. H. Knapp, 2014. Tectonic significance of porosity and permeability regimes in the red beds formations of the South Georgia Rift Basin. Tectonophysics, 632: 1–7.

Al-Aasm, S. Ihsan, and Crowe Richard, 2018. Fluid compartmentalization and dolomitization in the Cambrian and Ordovician successions of the Huron Domain, Michigan Basin. Marine and Petroleum Geology, 160–178.

Al-Aasm, S. Ihsan, Mrad Carole, and Packare Jeffery, 2018. Fluid compartmentalization of Devonian and Mississippian dolostones, Western Canada Sedimentary Basin: petrologic and geochemical evidence from frature mineralization. NRC Research Press: 265–305.

Al-hasani, A., M. H. Hakimi, I. M. Saaid, A. M. A. Salim, S. Q. A. Mahat, A. A. Ahmed, and A. A. B. Umar, 2018. Reservoir characteristics of the Kuhlan sandstones from Habban oilfield in the Sabatayn Basin, Yemen and their relevance to reservoir rock quality and petroleum accumulation. Journal of African Earth Sciences, 145: 131–147.

Ali, M., M. J. Khan, M. Ali, and S. Iftikhar, 2019. Petrophysical analysis of well logs for reservoir evaluation: a case study of “Kadanwari” gas field, middle Indus basin, Pakistan. Arabian Journal of Geosciences, 12.

Alsharhan, A. S., 2003. Petroleum geology and potential hydrocarbon plays in the Gulf of Suez rift basin, Egypt. AAPG Bulletin, 87: 143–180.

Atchley, S. C., S. C. James, H. Harlow, C. Leslie, J. Jiang, G. Carrelli, W. Bindon, and J. Beal, 2018. Geologic and resource assessment of the Upper Devonian Grosmont and upper Ireton Formations, central Grosmont shelf complex, Alberta, Canada. AAPG Bulletin, 102: 731–759.

Bagrintseva, K. I., 2015. Carbonate Reservoir Rocks Wiley-Scrivener, Hoboken, New Jersey.

Baker, J. C., P. J. Havord, K. R. Martin, and K. A. R. Ghori, 2000. Diagenesis and Petrophysics of the Early Permian Moogooloo Sandstone, Southern Carnarvon Basin, Western Australia. AAPG Bulletin, 84(2): 250–265.

Barker, C., 1990. Calculated volume and pressure changes during the cracking of oil and gas in reservoirs. AAPG Bulletin, 74(8): 1254–1261.

Baur, F. and B. J. Katz, 2018. Some practical guidance for petroleum migration modeling. Marine Petroleum Geolgoy: 409–421.

Beglinger, S. E., H. Doust, and S. Cloetingh, 2012. Relating petroleum system and play development to basin evolution: West African South Atlantic basins. Marine and Petroleum Geology, 30(1): 1–25.

Blazevic, M. A., M. E. Kirby, A. D. Woods, B. L. Browne, and D. D. Bowman, 2019. A sedimentary facies model for glacial-age sediments in baldwin lake, southern California. Sedimentary Geology, 219(14): 151–168.

Cai, X., J. Liu, Y. Zhang, P. Zhao, C. Liu, Z. Cheng, T. Zhu, and H. Xu, 2021. Oil and gas exploration progress of Sinopec during the 13th Five-year plan period and prospect forecast for the 14th Five-year plan. China Petroleum Exploration, 26(1): 31–42 (in Chinese with English abstract).

Cao, Q., J. Ye, H. Qing, J. Lu, S. Huang, and D. Tang, 2011. Pressure evolution and hydrocarbon migration-accumulation in the Moliqing fault depression, Yitong basin, Northeast China. Journal of Earth Science, 22(3): 351–362.

Chen, J. P., W. Li, Y. Y. Ni, D. G. Liang, C. M. Deng, and L. Z. Bian, 2018. The Permian source rocks in the Sichuan Basin and its natural gas exploration potential (Part I): spatial distribution of source rocks. Natural Gas Industry, 38(5): 1–16 (in Chinese with English abstract).

Chen, S., C. J. L. Wilson, Z. L. Luo, and Q. D. Deng, 1994. The evolution of the Western Sichuan Foreland Basin, southwestern China. Journal of Southeast Asian Earth Sciences, 10(3/4): 159–168.

Chen, Y., Y. Hu, Y. Wang, G. Liu, H. Zeng, J. Wang, M. Deng, C. Fang, C. Zhang, and H. Guan, 2013. The study of hydrocarbon potential of the Middle Triassic Leikoupo Formation in western Sichuan depression (R), Inner Scientific Report, SINOPEC: 40–41.

Chi, G., D. Lavoie, R. Bertrand and M. K. Lee, 2010. Downward hydrocarbon migration predicated from numerical modeling of fluid overpressure in the Paleozoic Anticosti Basin, eastern Canada. Geofluids, 10: 334–350.

Chi, G., C. Xue, H. Qing, W. Xue, J. Zhang, and Y. Sun, 2012. Hydrodynamic analysis of clastic injection and hydraulic fracturing structures in the Jinding Zn-Pb deposit, Yunnan, China. Geoscience Frontiers, 3(1): 73–84.

Chi, G. X., D. R. Xu, C. J. Xue, Z. H. Li, L. Patrick, T. Deng, Y. M. Wang, and H. Song, 2022. Hydrodynamic links between shallow and deep mineralization systems and implications for deep mineral exploration. Acta Geologica Sinica (English Edition), 96(1): 1–25.

Craig, J., N. Hakhoo, G. M. Bhat, M. Hafiz, M. R. Khan, R. Misra, S. K. Pandita, B. K. Raina, J. Thurow, and B. Thusu, 2018. Petroleum systems and hydrocarbon potential of the North-West Himalaya of India and Pakistan. Earth-Science Reviews, 187: 109–185.

Demaison, G., and B. J. Huizinga, 1994. Genetic classification of petroleum systems using three factors: charge, migration, and entrapment. The petroleum system—from source to trap. AAPG Memoir 60. P. 73–89.

Deming, D., 1994. Overburden rock, temperature, and heat flow. The petroleum system—from source to trap. AAPG Memoir 60. P. 165–186.

Downey, M. W., 1994. Hydrocarbon seal rocks. In: Magoon, L. B. and Dow, W. G., Eds, The petroleum system—from source to trap. AAPG Memoir 60. P. 159–164.

Demirel, I. H., 2004. Petroleum systems in the eastern and central Taurus region, Turkey. Marine and Petroleum Geology, 21(8): 1061–1071.

Ehrenberg, S. N. and Nadeau P. H., 2005. Sandstone vs. Carbonate petroleum reservoirs: A global perspective on porosity-depth and porosity-permeablity relationships. AAPG Bulletin, 89(4): 435–445.

Erdman, N., R. Campbell, and S. Asahina, 2006. Precise SEM Cross Section Polishing Via Argon Beam Milling. Microscopy Today: 22–25.

Eysa, E. A., F. S. Ramadan, M. M. El Nady, and N. M. Said, 2016. Reservoir characterization using porosity–permeability relations and statistical analysis: a case study from North Western Desert, Egypt. Arabian Journal of Geosciences, 9(5): 403–412.

Fang, C., H. Ji, J. Zhou, J. Zhang, H. Jia, and Z. Liu, 2016. The influences of sea-level changes on the quality of bank reservoirs of the Lower Cambrian Longwangmiao Formation, in the Gaoshiti-Moxi area, Sichuan Province, China. Journal of Natural Gas Science and Engineering, 32: 292–303.

Feng, D., T. Zhu, and H. Li, 2013. Geological features and control factors of reservoir forming in Middle Triassic Leikoupo Formation in western Sichuan basin. Journal of Xi'an Shiyou Univerisity (Natural Science Edition), 28(6): 1–7 (in Chinese with English abstract).

Feng, M. Y., Z. Zeng, X. Z. Wang, F. Zhang, Y. Z. Li, and K. Li, 2015. Implication of sedimentary facies and shale gas accumulation in the Lower Silurian Longmaxi Formation, eastern Sichuan Basin, China. Acta Geologica Sinica (English Edition), 89: 188–190.

Feng, M. Y., Z. T. Qiang, P. Shen, J. Zhang, Y. Z. Tao, and M. L. Xia, 2016. Evidences for hydrothermal dolomite of Sinian Dengying Formation in Gaoshiti-Moxi area, Sichuan Basin. Acta Petro Sinica, 37(5): 586–598 (in Chinese with English abstract).

Feng, M. Y., P. C. Wu, Z. T. Qiang, X. H. Liu, Y. Duan, and M. L. Xia, 2017. Hydrothermal dolomite reservoir in the Precambrian Dengying Formation of central Sichuan Basin, Southwestern China. Marine Petroleum Geology, 82: 206–219.

Fernández-Ibáñez, F., P. J. Moore, and G. D. Jones, 2019. Quantitative assessment of karst pore volume in carbonate reservoirs. AAPG Bulletin, 103(5): 1111–1131.

Figueiredo e Silva, R. C., S. Hagemann, L. M. Lobato, C. A. Rosière, D. A. Banks, G. J. Davidson, T. Vennemann, and J. Hergt, 2013. Hydrothermal fluid processes and evolution of the giant Serra Norte Jaspilite-Hosted iron ore deposits, Carajás Mineral Province, Brazil. Economic Geology, 108(4): 739.

Frolov, S. V., G. G. Akhmanov, E. A. Bakay, N. V. Lubnina, N. I. Korobova, E. E. Karnyushina, and E. V. Kozlova, 2015. Meso-Neoproterozoic petroleum systems of the Eastern Siberian sedimentary basins. Precambrian Research, 259: 95–113.

Fu, G., Y. F. Lv, and X. F. Fu, 2003. Evolutional stages of hydrocarbon concentration seal in mudstone caprock. Chinese Journal of Geology, 38(2): 165–171 (in Chinese with English abstract).

Fu, Q., and H. Qing, 2010. Medium and coarsely crystalline dolomites in the Middle Devonian Ratner Formation, southern Saskatchewan, Canada: origin and pore evolution. Carbonates and Evaporites, 26(2): 111–125.

Fu, Q., H. Qing, K. M. Bergman, and C. Yang, 2008. Dedolomitization and calcite cementation in the Middle Devonian Winnipegosis Formation in central Saskatchewan, Canada. Sedimentology, 55(6): 1623–1642.

Fuller M. L., 1919. Explorations in China. AAPG Bulletin, 3(1): 99–116.

Garland, J., J. Neilson, S. E. Laubach, and K. J. Whidden, 2012. Advances in carbonate exploration and reservoir analysis. Geological Society Special Publication, 370(1): 1–15.

Ghalayini, R., F. H. Nader, S. B. Daher, N. Hawie, and W. E. Chbat, 2018. Petroleum systems of Lebanon: An update and review. Journal of Petroleum Geology, 41(2): 189–214.

Gomez, C. T., J. Dvorkin, and T. Vanorio, 2010. Laboratory measurements of porosity, permeability, resistivity, and velocity on Fontainebleau sandstones. Geophysics, 75(6): 191–204.

Guerriero, V., S. Mazzoli, A. Iannace, S. Vitale, A. Carravetta, and C. Strauss, 2013. A permeability model for naturally fractured carbonate reservoirs. Marine Petroleum Geology, 40: 115–134.

Guo, C., D. Chen, H. Qing, S. Dong, G. Li, D. Wang, Y. Qian, and C. Liu, 2016. Multiple dolomitization and later hydrothermal alteration on the Upper Cambrian-Lower Ordovician carbonates in the northern Tarim Basin, China. Marine and Petroleum Geology, 72: 295–316.

Guo, J., X. Pang, F. Guo, X. Wang, C. Xiang, F. Jiang, P. Wang, J. Xu, T. Hu, W. Peng, and G. Dix, 2014. Petroleum generation and expulsion characteristics of

Lower and Middle Jurassic source rocks on the southern margin of Junggar Basin, northwest China: implications for unconventional gas potential. Canadian Journal of Earth Sciences, 51(6): 537–557.

Guo, X., D. Hu, R. Liu, X. Wei, and F. Wei, 2018. Geological conditions and exploration potential of Permian marine-continent transitional facies shale gas in the Sichuan Basin. Natural Gas Industry, 38(10): 11–18 (in Chinese with English abstract).

Guo, T., 2020. Dialectical materialist thinking and method in the discovery of Puguang, Yuanba and Fuling Gas Fields, China. Journal of Chengdu University of Technology (Science & Technology Edition), 47(6): 641–644.

Guo, X., X. Cai, J. Liu, C. Liu, Z. Cheng, B. Gao, and L. Shi, 2021. Natural gas exploration progress of Sinopec during the 13th Five-year plan period and prospect forecast for the 14th Five-year plan. Nature Gas Industry B, 41(8): 12–22 (in Chinese with English abstract).

Guo, X., Z. Huang, L. Zhao, W. Han, C. Ding, X. Sun, R. Yan, T. Zhang, X. Yang, and R. Wang, 2019. Pore structure and multi-fractal analysis of tight sandstone using MIP, NMR and NMRC methods: A case study from the Kuqa depression, China. Journal of Petroleum Science and Engineering, 178: 544–558.

Hackley, P. C., and A. W. Karlsen, 2014. Geologic assessment of undiscovered oil and gas resources in Aptian carbonates, onshore northern Gulf of Mexico Basin, United States. Cretaceous Research, 48: 225–234.

Hakimi, M. H., W. H. Abdullah, and M. R. Shalaby, 2012. Madbi-Biyadh/Qishn (!)

petroleum system in the onshore Masila Basin of the Eastern Yemen. Marine and Petroleum Geology, 35(1): 116–127.

Hao, F., T. Guo, Y. Zhu, X. Cai, H. Zou, and P. Li, 2008. Evidence for multiple stages of oil cracking and thermochemical sulfate reduction in the Puguang gas field, Sichuan Basin, China. AAPG Bulletin, 92(5): 611–637.

Hao, F., 2022. Enrichment mechanism and prospects of deep oil and gas. Acta Geologica Sinica, 96(3): 742–756.

He, D., Y. Ma, X. Cai, J. Zhang, and Y. Zhang, 2017. Comparison study on controls of geologica structural framework upon hydrocarbon distribution of marine basins in western China. Acta Petrologica Sinica, 33(4): 1037–1057 (in Chinese with English abstract).

Higgs, K. E., H. Zwingman, A. G. Reyes, and R. H. Funnell, 2007. Diagenesis, porosity evolution, and petroleum emplacement in tight gas reservoirs, Taranaki Basin, New Zealand. Journal of Sedimentary Research, 77(12): 1003–1025.

Hill, R. J., Y. C. Tang, and I. R. Kaplan, 2003. Insights into oil cracking based on laboratory experiments. Organic Geochemistry, 1651–1672.

Hill, R. J., E. Zhang, B. J. Katz, and Y. C. Tang, 2007. Modeling of gas generation from the Barnett Shale, Fort Worth Basin, Texas. AAPG Bulletin: 91 (4): 501–521.

Hu, Q., Y. Zhang, X. Meng, Z. Zheng, Z. Xie, and M. Li. 2017. Characterization of micro-nano pore networks in shale oil reservoirs of Paleogene Shahejie

Formation in Dongying Sag of Bohai Bay Basin, East China. Petroleum Exploration and Development, 44(5): 681–690 (in Chinese with English abstract).

Hu, Q. H., G. Mann, and J. H. Zhao, 2019. Pore structure and fluid uptake of the Yeso, Abo, and Cisco Formations in the Permian Basin in southeast New Mexico, USA. Interpretation: S1–17.

Hu, Q. H., R. P. Quintero, H. F. El-Sobky, J. H. Kang, and T. Zhang, 2020. Coupled nano-petrophysical and organic-geochemical study of the Wolfberry Play in Howard County, Texas U.S.A. Marine and Petroleum Geology: 1–15.

Hu, Z., S. Huang, Z. Li, H. Qing, M. Fan, and Y. Lan, 2012. Temperatures of dolomitizing fluids in the Feixianguan Formation from the Northeastern Sichuan Basin. Science China Earth Sciences, 55(10): 1627–1640.

Hu, Z., S. Huang, H. Qing, Q. Wang, C. Wang, and X. Gao, 2008. Evolution and global correlation for strontium isotopic composition of marine Triassic from Huaying Mountains, eastern Sichuan, China. Science in China Series D: Earth Sciences, 51(4): 540–549.

Huang, D., X. Dai, Y. Dai, Y. Zhu, Y. Yang, and S. Pei, 2011. Geochemical behaviors and gas origins in the Hewanchang Gas Field, northern part of the Western Sichuan Basin. Natural Gas Industry, 31(3): 37–40.

Huang, W., S. Lu, and S. H. Osman, 2017. Quality grading system for tight sandstone reservoirs in the Quantou 4 Member, southern Songliao Basin, Northeast China. Interpretation, 5(4): T503–T522.

Jiang, L., R. H. Worden, and C. F. Cai, 2014. Thermochemical sulfate reduction and fluid evolution of the Lower Triassic Feixianguan Formation sour gas reservoirs, northeast Sichuan Basin, China. AAPG Bulletin, 98(5): 947–973.

Jiang, L., C. F. Cai, R. H. Worden, S. F. Crowley, L. Q. Jia, K. Zhang, and I. J. Dunca, 2016. Multiphase dolomitization of deeply buried Cambrian petroleum reservoirs, Tarim Basin, north-west China. Sedimentology, 63: 2130–2157.

Jiang, L., R. H. Worden, and C. B. Yang, 2018a. Thermochemical sulphate reduction can improve carbonate petroleum reservoir quality. Geochimia et Cosmochimica Acta, 223: 127–140.

Jiang, L., R. H. Worden, C. F. Cai, A. J. Shen, X. Y. He, and L. Y. Pan, 2018b. Contrasting diagenetic evolution patterns of platform margin limestones and dolostones in the Lower Triassic Feixianguan Formation, Sichuan Basin, China. Marine and Petroleum Geology, 92: 332–351.

Jiang, L., S. Y. Hu, W. Z. Zhao, Z. H. Xu, S. Y. Shi, Q. L. Fu, H. L. Zeng, W. Liu and A. Fall, 2018c. Diagenesis and its impact on a microbially derived carbonate reservoir from the Middle Triassic Leikoupo Formation, Sichuan Basin, China. AAPG Bulletin, 102: 2599–2628.

Jiang, L., Z. H. Xu, S. Y. Shi, and W. Liu, 2019. Multiphase dolomitization of a microbialite-dominated gas reservoir, the Middle Triassic Leikoupo Formation, Sichuan Basin, China. Journal of Petroleum Science and Engineering, 180: 820–834.

Jiang, W. M., Q. Q. Luo, K. B. Shi, B. Liu, Y. C. Wang, and X. Q. Gao, 2021. Origin of a microbial-dominated carbonate reservoir in the Lower Cambrian Xiaoerbulake Formation, Bachu-Tazhong area, Tarim Basin, NW China. Marine and Petroleum Geology, 1–27.

Jiang, Y., D. Bao, W. Zhang, Z. Ye, S. Li, Z. Yong, and B. Li, 2021. Transport conductors and its combination characteristics of Leikoupo Formation in western Sichuan Depression, China. Journal of Chengdu University of Technology (Science & Technology edition), 48(2): 196–205.

Jin, X., Q. Dou, J. Hou, Q. Huang, Y. Sun, Y. Jiang, T. Li, P. Sun, C. Sullivan, H. Adersokan, and Z. Zhang, 2017. Rock-physics-model-based pore type characterization and its implication for porosity and permeability qualification in a deeply-buried carbonate reservoir, Changxing Formation, Lower Permian, Sichuan Bain, China. Journal of Petroleum Science and Engineering, 153: 223–233.

Jin, Z., J. Zhang, and X. Tang, 2021. Unconventional natural gas accumulation system. Natural Gas Industry, 41(8): 58–68 (in Chinese with English abstract).

Jones, D. J. R., D. J. McCarthy, and T. J. H. Dodd, 2019. Tectonostratigraphy and the petroleum systems in the Northern sector of the North Falkland Basin, South Atlantic. Marine and Petroleum Geology, 103: 150–162.

Jordan, C. F., and J. L. Wilson, 1994. Carbonate Reservoir Rocks. In: Magoon, L. B. and Dow, W. G., Eds, The petroleum system—from source to trap. AAPG Memoir 60. P. 141–157.

Karakitsios, V., 2013. Western Greece and Ionian Sea petroleum systems. AAPG

Bulletin, 97(9): 1567–1595.

Katz, B. J., E. I. Dittmar, and G. E. Ehret, 2000. A geochemical review of carbonate source rocks in Italy. Journal of Petroleum Geology, 23(4): 399–424.

Katz, B. J., E. A. Mancini, and A. A. Kitchka, 2008. A review and technical summary of the AAPG Hedberg Research Conference on “Origin of petroleum—Biogenic and/or abiogenic and its significance in hydrocarbon exploration and production”. AAPG Bulletin, 92(5): 549–556.

Katz, B. J. and F. Lin, 2014. Lacustrine basin unconventional resource plays: Key differences. Marine and Petroleum Geology: 255–265.

Katz, B. J. and M. A. Everett, 2016. An overview of pre-Devonian petroleum systems-Unique characteristics and elevated risks. Marine and Petroleum Geology, 73: 492–516.

Katz, B. J. and I. Arango, 2018. Organic porosity: A geochemist's view of the current state of understanding. Organic Geochemistry: 1–16.

Kotarba and Nagao, 2008. Composition and origin of natural gases accumulated in the Polish and Ukraninian parts of the Carpathian region: Gaseous hydrocarbons, noble gases, carbon dioxide and nitrogen. Chemical Geology, 255(3): 426–438.

Lai, J., G. Wang, Y. Ran, and Z. Zhou, 2015. Predictive distribution of high-quality reservoirs of tight gas sandstones by linking diagenesis to depositional facies: Evidence from Xu-2 sandstones in the Penglai area of the central Sichuan basin, China. Journal of Natural Gas Science and Engineering, 23: 97–111.

Lash, G. G., and T. Engelder, 2011. Thickness trends and sequence stratigraphy of the Middle Devonian Marcellus Formation, Appalachian Basin: Implications for Acadian foreland basin evolution. AAPG Bulletin, 95(1): 61–103.

Li, J., and Z. X. Cai, 2022. The role of seal and source rocks in fluid-rock interactions and their reservior effects within the carbonate deep burial realm. Acta Geologica Sinica, 96(4): 1353–1361.

Li, P., F. Hao, X. Guo, H. Zou, X. Yu, and G. Wang, 2015. Processes involved in the origin and accumulation of hydrocarbon gases in the Yuanba gas field, Sichuan Basin, southwest China. Marine and Petroleum Geology, 59: 150–165.

Li, R., H. Hu, G. Xu, Q. Wang, X. Song, and K. Long, 2017. Influcences of dolomitization on resevoirs of upper T_2l^4 of Leikoupo Formation in western Depression, Sichuan Basin. Xinjiang Petroleum Geology, 38(2): 149–154 (in Chinese with English abstract).

Li, Y., Z. K. Yan, D. C. Su, S. G. Liu, J. X. Cao, H. B. Li, W. Sun and S. L. Dong, 2014. The advance of Longmen shan orogenic wedge and migration of the foreland reef and shoal during the indosinian orogeny, China. Acta Petrologica Sinica, 30(3): 641–654 (in Chinese with English abstract).

Li, Y., Z. Kang, Z. Xue, and S. Zheng, 2018. Theories and practices of carbonate reservoirs development in China. Petroleum Exploration and Development, 45: 152–162 (in Chinese with English abstract).

Li, Y., X. Z. Wang, M. Y. Feng, D. M. Zeng, S. Y. Xie, R. Fan, L. J. Wang, T. Zeng, and X. F. Yang, 2019. Reservior characteristics and genetic differences between the second and fourth members of Sinian Dengying Formation in northern Sichuan Basin and its surrounding areas. Petroleum Exploration and Development, 46(1): 52–64 (in Chinese with English abstract).

Li, Z., S. Liu, and J. Lin, 2009. Structural configuration and its genetic mechanism of the West Sichuan depression in China. Journal of Chengdu University of Technology (Science & Technology Edition), 36(6): 645–653 (in Chinese with English abstract).

Liao, F., X. Wu, S. Huang, and C. Yu, 2013. Geochemical characteristics and gas-source correlation of Leikoupo Formation in Zhongba field, northwest Sichuan Basin. Natural Gas Geoscience, 24(1): 108–115 (in Chinese with English abstract).

Ling, T., Y. Song, Q. Li, X. Pang, Z. Jiang, Z. Li, X. Tang, H. Yu, Y. Sun, S. Fan, and L. Zhu, 2019. A Quantitative evaluation of shale gas content in different occurence states of the Longmaxi Formation: a new insight from well JY-A in the Fuling shale gas field, Sichuan basin. Acta Geologica Sinica (English Edition), 93(2): 400–419.

Liu, C. C., Y. Y. Wang, S. Zhao, Y. Duan, Y. Zhang and Y. Xia, 2020. Study on fluid inclusion charateristics and hydrocarbon accumulation periods of Leikoupo Formation in Pengzhou Gasfield. Journal of Xi'an Shiyou University (Natural Science Edition), 35(6): 17–21 (in Chinese with English abstract).

Liu, D. R., 1981. A study on the age of natural gas development in ancient China.

Social Sicence Research (in Chinese), 3(5): 67–112.

Liu, J. C., and B. J. Katz, 2013. Integration of basin modeling, uncertainty analysis, hydrocarbon charge volume assessment in petroleum exploration risk evaluation. International Petroleum Technology Conference. P. 1–20.

Liu, S., J. M. Song, P. Luo, H. R. Qing, T. Lin, W. Sun, Z. W. Li, H. Wang, H. L. Peng, Y. Q. Yu, Y. Long, and Y. B. Wan, 2016a. Characteristics of microbial carbonate reservoir and its hydrocarbon exploring outlook in the Sichuan Basin, China. Journal of Chengdu University of Technology (Science & Technology Edition), 43(2): 130–151 (in Chinese with English abstract).

Liu, S., Y. Yang, B. Deng, Y. Zhong, L. Wen, W. Sun, Z. Li, L. Jansa, J. Li, J. Song, X. Zhang and H. Peng, 2021a. Tectonic evolution of the Sichuan Basin, Southwest China. Earth-Science Reviews, 213: 1–18.

Liu, W., T. Borjigin, X. Wang, M. Li, G. Hu, J. Wang, L. Lu, H. Zhao, Q. Chen, and H. Luo, 2017. New knowledge of hydrocarbon generating theory of organic matter in Chinese marine carbonates. Petroleum Exploration and Development Online, 44(1): 159–169 (in Chinese with English abstract).

Liu, X. H., Z. J. Shi, M. Y. Feng, L. J. Wang, and X. Z. Wang, 2021b. Pore-infillings in stratiform siliceous rocks of the Dengying Formation in Wangcang Area, Northern Sichuan Basin. Journal of Southwest Petroleum University (Science & Technology Edition), 43(3): 1–11 (in Chinese with English abstract).

Liu, Y., N. Qiu, Z. Xie, Q. Yao, and C. Zhu, 2016b. Overpressure compartments in the central paleo-uplift, Sichuan Basin, southwest China. AAPG Bulletin, 100(5):

867–888.

Lønøy, A., 2006. Making sense of carbonate pore systems. AAPG Bulletin, 90(9): 1381–1405.

Lucia, F. J., and R. G. Loucks, 2013, Micropores in carbonate mud: Early development and petrophysics. Transactions / Gulf-Coast Association of Geological Societies, 63: 691–692.

Loucks, R. G., and S. P. Dutton, 2019. Insights into deep, onshore Gulf of Mexico Wilcox sandstone pore networks and reservoir quality through the integration of petrographic, porosity and permeability, and mercury injection capillary pressure analyses. AAPG Bulletin, 103(3): 745.

Lokier, S.W., and M. Al., Junaibi, 2016. The petrographic description of carbonate facies: are we all speaking the same language? Sedimentology, 63: 1843–1885.

Lu, L., 1989. The metamorphic series and crustal evolution of the basement of the Yangtze platform. Journal of Southeast Asian Earth Sciences, 3: 293–301.

Lu, Z., H. Chen, H. Qing, G. Chi, Q. Chen, D. You, H. Yin, and S. Zhang, 2017. Petrography, fluid inclusion and isotope studies in Ordovician carbonate reservoirs in the Shunnan area, Tarim basin, NW China: Implications for the nature and timing of silicification. Sedimentary Geology, 359: 29–43.

Machel, H. G., 2001. Bacterial and thermochemical sulfate reduction in diagenetic settings — old and new insights. Sedimentary Geology, 140(1): 143–175.

Machel, H. G., and J., Lonnee, 2002. Hydrothermal dolomite—a product of poor definition and imagination. Sedimentary Geology: 163–171.

Marek, Stadtműller, 2019. Well logging interpretation methodology for carbonate formation fracture system properties determination. Acta Geophysica, 67: 1933–1943.

Ma, X., Y. Yang, L. Wen, and B. Luo, 2019. Distribution and exploration direction of medium-and large-sized marin carbonate gas fields in Sichuan Basin, SW China. Petroleum Exploration and Development, 46(1): 1–13.

Ma, Y., X. Guo, T. Guo, R. Huang, X. Cai, and G. Li, 2007. The Puguang gas field: New giant discovery in the mature Sichuan Basin, southwest China. AAPG Bulletin, 91(5): 627–643.

Ma, Y., Z. He, P. Zhao, H. Zhu, J. Han, D. You, and J. Zhang, 2019. A new progress in formation mechanism of deep and ultra-deep carbonate reservior. Acta Petrolei Sinica, 40(12): 1415–1425 (in Chinese with English abstract).

Magoon, L. B., and Dow W. G., 1994. The petroleum system—from source to trap.

Magoon, L. B., T. L. Hudson, and H. E. Cook, 2001. Pimienta-Tamabra(!)—A Giant Supercharged Petroleum System in the Southern Gulf of Mexico, Onshore and Offshore Mexico, in C. Bartolini, R.T. Buffler, and A. Cantú-Chapa, eds., The Western Gulf of Mexico Basin: Tectonics, Sedimentary Basins, and Petroleum Systems: AAPG Memoir 75, P. 83–125.

Magoon, L. B., T. L. Hudson and K. E. Peters, 2005. Egret-Hibernia(!), a significant petroleum system, northern Grand Banks area, offshore. AAPG Bulletin, 89(9): 1203–1237.

Makeen, Y. M., W. H. Abdullah, M. J. Pearson, M. H. Hakimi, H. A. Ayinla, O. M. A. Elhassan, and A. M. Abas, 2016. History of hydrocarbon generation, migration and accumulation in the Fula sub-basin, Muglad Basin, Sudan: Implications of a 2D basin modeling study. Marine and Petroleum Geology, 77: 931–941.

Mancini, E. A., P. Li, D. A. Goddard, V. Ramirez, and S. C. Talukdar, 2008. Mesozoic (Upper Jurassic–Lower Cretaceous) deep gas reservoir play, central and eastern Gulf coastal plain. AAPG Bulletin, 92(3): 283–308.

Mani, D., B. Ratnam, M. S. Kalpana, D. J. Patil, and A. M. Dayal, 2016. Elemental and organic geochemistry of Gondwana sediments from the Krishna–Godavari Basin, India. Chemie der Erde - Geochemistry, 76(1): 117–131.

Mansurbeg, H., D. Morad, R. Othman, S. Morad, A. Ceriani, I. Al-Aasm, K. Kolo, P. Spirov, J. N. Proust, A. Preat, and H. Koyi, 2016. Hydrothermal dolomitization of the Bekhme formation (Upper Cretaceous), Zagros Basin, Kurdistan Region of Iraq: Record of oil migration and degradation. Sedimentary Geology, 341: 147–162.

Medici, G., L. Smeraglia, A. Torabi, and C. Botter, 2021. Review of modeling approaches to groundwater flow in deformed carbonate aquifers. Groundwater, 59(3): 334–351.

Meng, Y. Z., G. Xu, C. Yang, H. Yuan, and J. Liang, 2015. Hydrocarbon accumulation conditions of the weathering crust paleokarst gas reservoir of Leikoupo Formation, West Sichuan, China. Journal of Chengdu University of Technology, 42(1): 70–79 (in Chinese with English abstract).

Neilson, J. E., N. H. Oxtoby, M. D. Simmons, I. R. Simpson, and N. K. Fortunatova, 1998. The relationship between petroleum emplacement and carbonate reservoir quality: examples from Abu Dhabi and the Amu Darya Basin. Marine Petroleum Geology, 15: 57–72.

Nesheim, T. O., 2019. Examination of downward hydrocarbon charge within the Bakken-Three Forks petroleum system – Williston Basin, North America. Marine and Petroleum Geology, 104: 346–360.

Ning, M., S. Liu, and W. Gong, 2015. Prediction of dolomite reservoir distribtuion on top of Triassic Leikoupo Formation in Chuanxi depression. China Petroleum Exploration, 20(3): 31–37 (in Chinese with English abstract).

Okolo, G. N., R. C. Everson, H. W. J. P. Neomagus, M. J. Roberts, and R. Sakurovs, 2015. Comparing the porosity and surface areas of coal as measured by gas adsorption, mercury intrusion and SAXS techniques. Fuel, 141: 293–304.

Osorno, J., and A. Rangel, 2015. Geochemical assessment and petroleum systems in the Sinú-San Jacinto Basin, northwestern Colombia. Marine and Petroleum Geology, 65: 217–231.

Pang, X., C. Jia, W. Wang, C. Chen, M. Li, F. Jiang, T. Hu, K. Wang, and Y. Wang, 2021. Buoyance-driven hydrocarbon accumulation depth and its implication for unconventional resource prediction. Geoscience Frontiers, 1–17.

Peters, K. E., and M. R. Cassa, 1994. Applied Source Rock Geochemistry. The petroleum system—from source to trap. AAPG Memoir 60. P. 93–120.

Peters, K. E., L. B. Magoon, K. J. Bird, Z. C. Valin and M. A. Keller, 2006. North slope, Alaska: Source rock distribution, richness, thermal maturity, and petroleum charge. AAPG Bulletin, 90(2): 261–292.

Pontes, C., F. Bezerra, G. Bertotti, V. L. Bruna, P. Audra, J. D. Waele, A. S. Auler, F. Balsamo, S. D. Hoop, and L. Pisani, 2021. Flow pathways in multiple-direction fold hinges: Implications for fractured and karstified carbonate reservoirs. Journal of Structural Geology, 146(1): 1–19.

Qin, H., L. Pan, F. Yin, and J. Shen, 2016. Discuss on source of natural gas and causation of reversed orders of $\delta^{13}C$ in alkane gas from Leikoupo Formation in Yuanba, Sichuan basin, China. Journal of Chengdu University of Technology (Sciences & Technology Edition), 43(5): 1671–9727 (in Chinese with English abstract).

Qin, S., G. Zhou, Z. Zhou, and Y. Yang, 2018. Geochemical characteristics of natural gases from different petroleum systems in the Longgang gas field, Sichuan Basin, China. Energy Exploration and Exploitation, 36(6): 1376–1394.

Qing, H., and A. R. Nimegeers, 2008. Lithofacies and depositional history of Middle carbonate-evaporite cycles in a Mississippian ramp setting, Steelman-Bienfait area, southeastern Saskatchewan, Canada. Bulletin of Canadian Petroleum Geology, 56(3): 209–234.

Rankey, E. C., 2020. Eustatic, climatic, and oceanogrphic influences on geomorphology and architecture of isolated carbonate platforms: Miocene, northwest shelf, Australia. Lithosphere: 1–33.

Regnet, J. B., C. David, P. Robion, and B. Menéndez, 2019. Microstructures and physical properties in carbonate rocks: A comprehensive review. Marine and Petroleum Geology, 103: 366–376.

Rosales, I., L. Pomar, and S. F. Al-Awwad, 2018. Microfacies, diagenesis and oil emplacement of the Upper Jurassic Arab-D carbonate reservoir in an oil field in central Saudi Arabia (Khurais Complex). Marine and Petroleum Geology, 96: 551–576.

Ruppel, S. C., and W. B. Ward, 2013. Outcrop-based characterization of the Leonardian carbonate platform in west Texas: Implications for sequence-stratigraphic styles in the Lower Permian. AAPG Bulletin, 97(2): 223–250.

Sachan, H. K., A. Kharya, P. C. Singh, F. Rolfo, C. Groppo, and S. K. Tiwari, 2017. A fluid inclusion study of blueschist-facies lithologies from the Indus suture zone, Ladakh (India): Implications for the exhumation of the subduction related Sapi-Shergol ophiolitic mélange. Journal of Asian Earth Sciences, 146: 185–195.

Sachse, V. F., A. Wenke, R. Littke, H. Jabour, O. Kluth, and R. Zühlke, 2016. 2D petroleum system analysis of the Tarfaya Basin, on-offshore Morocco, North Africa. Marine and Petroleum Geology, 77: 1108–1124.

Saller, A. H., D. Pollitt, and J. A. D. Dickson, 2014. Diagenesis and porosity development in the First Eocene reservoir at the giant Wafra Field, Partitioned Zone, Saudi Arabia and Kuwait. AAPG Bulletin, 98(6): 1185–1212.

Schmitt, M., C. P. Fernandes, J. A. B. da Cunha Neto, F. G. Wolf, and V. S. S. dos

Santos, 2013. Characterization of pore systems in seal rocks using Nitrogen gas adsorption combined with Mercury Injection Capillary Pressure techniques. Marine and Petroleum Geology, 39: 138–149.

Schoell, M., 1983. Genetic characterization of natural gases. AAPG Bulletin, 67(12): 2225–2238.

Shalaby, M. R., M. H. Hakimi, and W. H. Abdullah, 2013. Petroleum system analysis of the Khatatba Formation in the Shoushan Basin, north Western Desert, Egypt. Arabian Journal of Geosciences, 7(10): 4303–4320.

Shen, A., A. Hu, L. Pan, and M. She, 2017. Origin and distribution of grain dolostone reservoirs in the Cambrian Longwangmiao Formation, Sichuan Basin, China. Acta Geologica Sinica (English Edition), 91(1): 204–218.

Shen, Z., T. Liu, Z. Lv, and S. Liu, 2008. A comparison study on the gas source of Jurassic natural gas in the western Sichuan depression. Geological Journal of China Universities, 14(4): 577–582 (in Chinese with English abstract).

Sonnenberg, S. A., and A. Pramudito, 2009. Petroleum geology of the giant Elm Coulee field, Williston Basin. AAPG Bulletin, 93(9): 1127–1153.

Su, C. P, Y. He, X. B. Song, B. Dong, and X. Q. Wu, 2022. Reinterpretation of gas sources in the Middle Triassic Leikoupo Formation in western Sichuan gas field, Sichuan Basin. Oil & Gas Geology, 43(2): 342–352.

Sun, W., S. G. Liu, J. X. Cao, B. Deng, J. M. Song, G. Z.Wang, Y. Yuan, and H. Wang, 2017. Analysis on the formation conditions of large-scale marine deep and super-deep strata gas fields in the middle-northern segments of western

Sichuan Superimposed Basin, China. Acta Petrologica Sinica, 33(4): 1171–1188 (in Chinese with English abstract).

Sun, T., X. Luo, H. Qing, X. Kou, Z. Sheng, G. Xu, and Y. Zuo, 2020. Characteristics and Natural Gas Origin of Middle–Late Triassic Marine Source Rocks of the Western Sichuan Depression, SW China. Acta Geologica Sinica, 94(2): 376–398.

Sutton, S. J., F. G. Ethridge, W. R. Almon, W. C. Dawson, and K. K. Edwards, 2004. Textural and sequence-stratigraphic controls on sealing capacity of Lower and Upper Cretaceous shales, Denver basin, Colorado. AAPG Bulletin, 88(8): 1185–1206.

Tang, P., D. Z. Chen, Y. X., Qian, Y. Z., Wang, and Bo Yang, 2022. Types, petrophysical properties and pore evolution of Late Ediacaran microbial carbonates, Tarim Basin, NW China. Acta Geologica Sinica, 96(4): 1362–1375.

Tang, Y., 2013. Characterization of the sedimentation of the Leikoupo Formation and the weathering crust reservoirs at the top of the formation in the western Sichuan Basin. Oil & Gas Geology, 34(1): 008 (in Chinese with English abstract).

Tian, Z., 1990. The formation and distribution of Mesozoic-Cenozoic sedimentary basins in China. Journal of Petroleum Geology, 13(1): 19–34.

Tian, H., S. Tang, J. Zhang, Y. Xin, X. Wang, and W. Li, 2018. Characteristics and formation conditions of carbonate reservoir in Leikoupo Formation of western

Sichuan Basin. Nature Gas Geoscience, 29(11): 1585–1594 (in Chinese with English abstract).

Wang, C., J. Dai, X. Zhao, Y. Li, S. A. Graham, D. He, B. Ran, and J. Meng, 2014. Outward-growth of the Tibetan Plateau during the Cenozoic: A review. Tectonophysics, 621: 1–43.

Wang, C., Z. Feng, H. Wu, P. Wang, F. Kong, Z. Feng, Y. Ren, G. Yang, X. Wang, Y. Huang, and S. Zhang, 2008. Preliminary Achievement of the Chinese Cretaceous Continental Scientific Drilling Project-SK-1. Acta Geologica Sinica, 82(1): 9–20 (in Chinese with English abstract).

Wang, X. Z., B. Li, X. Y. Yang, L. Wen, L. Xu, S. Y. Xie, Y. Du, M. Y. Feng, X. F. Yang, Y. P. Wang, and S. Q. Pei, 2021. Characteristics of “Guangyuan-Wangcang” through during Late Middle Permian and its petroleum geological significance in northern Sichuan Basin, SW China. Petroleum Exploration and Development, 48(3): 562–574 (in Chinese with English abstract).

Wang, Y., K. E. Peters, J. M. Moldowan, K. J. Bird, and L. B. Magoon, 2018. Cracking, mixing, and geochemical correlation of crude oils, North Slope, Alaska. AAPG Bulletin, 98(6): 1235–1267.

Wang, Z., W. Zhao, S. Hu, A. Xu, Q. Jiang, H. Jiang, S. Huang, and Q. Li, 2017. Control of tectonic differentiation on the formation of large oil and gas fields in craton basins: A case study of Sinian–Triassic of the Sichuan Basin. Natural Gas Industry, 4(2): 141–155.

Wang, J., Z. W. Wang, X. G. Fu, C. Y. Song, F. W. Tan and H. Y. Wei, 2022. New discoveries on the first petroleum scientific drilling (QK-1) of the Qiangtang Basin, Tibetan Plateau. Science China Press: 321–328 (in Chinese with English abstract).

Wei, W., D. Chen, H. Qing, and Y. Qian, 2017. Hydrothermal dissolution of deeply buried Cambrian dolomite rocks and porosity generation: Integrated with geological studies and reactive transport modeling in the Tarim Basin, China. Geofluids. P1–19.

Wen, J., M. D. Sun, Z. Cui, J. Wang, H. Zhang, Z. X. Cai, M. Ostadhassan, Q. Wang, and Q. Hu, 2023. Characterization of crude oil charging of Xiaoerbulake dolomite in the Tarim basin: Insights from bitumen distribution. Marine and Petroleum Geology, P. 1–11.

Whiticar, M. J., 1994. Correlation of natural gases with their sources. The petroleum system—from source to trap. AAPG Memoir 60. P. 261–283.

Wilson, M. E. J., M. J. Evans, N. H. Oxtoby, D. S. Nas, T. Donnelly, and M. Thirlwall, 2007. Reservoir quality, textural evolution, and origin of fault-associated dolomites. AAPG Bulletin, 91(9): 1247–1272.

Woods, A. D., P. D. Alms, P. M. Monarrez, and S. Mata, 2019. The interaction of recovery and environmental conditions: An analysis of the outer shelf edge of western North America during the early Triassic. Palaeogeography, Palaeoclimatology, Palaeoecology, 513: 52–64.

Wu, X., Y. Chen, G. Liu, H. Zeng, Y. Wang, Y. Hu, and W. Liu, 2017a. Geochemical characteristics and origin of natural gas reservoired in the 4th Member of the Middle Triassic Leikoupo Formation in the Western Sichuan Depression, Sichuan Basin, China. Journal of Natural Gas Geoscience, 2(2): 99–108.

Wu, X., Q. Liu, G. Liu, P. Wang, H. Li, Q. Meng, Y. Chen, and H. Zeng, 2017b. Geochemical characteristics and genetic types of natural gas in the Xinchang gas field, Sichuan Basin, SW China. Acta Geologica Sinica (English Edition), 91(6): 2200–2213.

Wu, Y., P. Tahmasebi, C. Lin, M. A. Zahid, C. Dong, A. N. Golab, and L. Ren, 2019. A comprehensive study on geometric, topological and fractal characterizations of pore systems in low-permeability reservoirs based on SEM, MICP, NMR, and X-ray CT experiments. Marine and Petroleum Geology, 103: 12–28.

Xiang, B., N. Zhou, W. Ma, M. Wu, and J. Cao, 2015. Multiple-stage migration and accumulation of Permian lacustrine mixed oils in the central Junggar Basin (NW China). Marine and Petroleum Geology, 59: 187–201.

Xu, J., and Z. Zhao, 2010. Causative mechanism and related tectonic movement of the 2008 Wenchuan M8 Earthquake. Geology in China, 37(4): 967–977 (in Chinese with English abstract).

Xu, C., J. M. Gehenn, D. Zhao, G. Xie, and M. K. Teng, 2015. The fluvial and lacustrine sedimentary systems and stratigraphic correlation in the Upper Triassic Xujiahe Formation in Sichuan Basin, China. AAPG Bulletin, 99(11): 2023–2041.

Xu, G., X. Feng, L. Zhu, and Q. X. Wang, 2011. Exploration suggerstions on

Leikoupo to Maantang formations in Xinchang Structural Belt, west Sichuan basin. Natural Gas Technology and Economy, 5(5): 16–21 (in Chinese with English abstract).

Xu, G., X. Song, X. Feng, K. Long, Q. Wang, G. Shi, and L. Zhu, 2013. Gas potential of the Middle Triassic Leikoupo Formation in the western Sichuan basin. Natural Gas Industry, 33(8): 8–14 (in Chinese with English abstract).

Xu, H., G. Wei, C. Jia, Y. Wei, T. Zhou, W. Xie, C. Li, and B. Luo, 2012. Tectonic evolution of the Leshan-Longnüsi paleo-uplift and its control on gas accumulation in the Sinian strata, Sichuan Basin. Petroleum Exploration and Development, 39(4): 436–446.

Xu, X., J. Zhu, X. Jiang, Y. Chen and Y. Chen, 2017. Principle of TSM basin simulation system and its application. Petroleum Geology and Experiment, 39(6): 730–737 (in Chinese with English abstract).

Xu, Q., Y. Ma, B. Liu, X. Song, J. Su, and Z. Chen, 2019. Characteristics and control mechanism of nanoscale pores in lacustrine tight carbonates: Examples from the Jurassic Da’anzhai member in the central Sichuan Basin, China. Journal of Asian Earth Sciences, 178: 156–172.

Ye, J., 2003. Assessment of hydrocarbon source rocks in Xu-2 Member, Ma'antang formation, Gas system in west Sichuan basin depression. Natural Gas Industry, 23(1): 21–25.

Yin, H., S. Xie, J. Yan, C. Hu, J. Huang, W. Qie, and X. Qiu, 2011. Geobiological approach to evaluating marine carbonate source rocks of hydrocarbon. Science

China Earth Sciences, 54(8): 1121–1135.

Zeng, H., J. Wang, G. Zhang, and H. Guan, 2008. Hydrocarbon resource evaluation of upper combination marine in western Sichuan basin. Inner Scientific Report, SINOPEC, 1–150.

Zhang, N., M. He, B. Zhang, F. Qiao, H. Sheng, and Q. Hu, 2016. Pore structure characteristics and permeability of deep sedimentary rocks determined by mercury intrusion porosimetry. Journal of Earth Science, 27(4): 670–676.

Zhang, S., K. He, G. Hu, J. Mi, Q. Ma, K. Liu, and Y. Tang, 2018. Unique chemical and isotopic characteristics and origins of natural gases in the Paleozoic marine formations in the Sichuan Basin, SW China: Isotope fractionation of deep and high mature carbonate reservoir gases. Marine and Petroleum Geology, 89: 68–82.

Zhang, X., S. Long, S. Liu, and S. Wu, 2008. The study of main factors of marine strata hydrocarbon accumulation in western Sichuan depression. Inner Scientific Report, SINOPEC: 1–100.

Zhang, Y., Z. Ma, K. Yang, G. Wang, S. Wu, L. Tang, S. Long, and K. Zhang, 2007. The forecast of natural oil and gas potential in marine strata, western sichuan basin, southwest China. Acta Geologica Sinica, 81(8): 1041–1047 (in Chinese with English abstract).

Zhao, L., and M. Chen, 2015. A discussion on the interrelationships between five properties in reservoir evaluation. Natural Gas Industry B, 2(3): 136–143.

Zhao, M., W., H. J. Behr, H. Ahrendt, K. Wemmer, Z. Ren and Z. Zhao, 1996.

Thermal and tectonic history of the Ordos Basin, China: Evidence from Apatite Fission Track Analysis, Vitrinite Reflectance, and K-Ar Dating. AAPG Bulletin, 80(7): 1110–1133.

Zhao, W., S. Hu, L. Wei, T. Wang, and Y. Li, 2014. Petroleum geological features and exploration prospect of deep marine carbonate rocks in China onshore: A further discussion. Natural Gas Industry, 1(1): 14–23 (in Chinese with English abstract).

Zhao, W. Z., C. S. Bian, C. C. Xu, H. J. Wang, T. S. Wang, and Z. S. Shi, 2011. Assessment on gas accumualtion potential and favorable plays within the Xu-1, 3 and 5 Members of Xujiahe Formation in Sichuan Basin. Petroleum Exploration and Development, 38(4): 385–393.

Zheng, M., C. Jia, W. Wang, P. Li, J. Li, X. Wu, and Y. Zhang, 2015. The relationship between tectonic evolution and oil-cracking gas accumulation in late stage for marine superimposed basins. Natural Gas Geoscience, 26(2): 277–291 (in Chinese with English abstrat).

Zhu, C. Q., N. S. Qiu, Q. Jiang, S. Hu, and S. Zhang, 2015. Thermal history reconstruction based on multiple paleo-thermal records of the Yazihe Area, Western Sichuan Depression, SW China. Chinese Journal of Geophysics, 58(6): 3660–3670 (in Chinese with English abstract).

Zhu, G., Y. Cao, L. Yan, H. Yang, C. Sun, Z. Zhang, T. Li, and Y. Chen, 2018. Potential and favorable areas of petroleum exploration of ultra-deep marine strata more than 8000 m deep in the Tarim Basin, Northwest China. Journal of

Natural Gas Geoscience, 3(6): 321–337.

Zhu, G. Y., J. F. Li, Z. Y. Zhang, M. Wang, N. Xue, T. He, and K. Zhao, 2020. Stability and cracking threshold depth of crude oil in 8000 m ultra-deep reservoir in the Tarm Basin. Fuel, 1–15.

Zhu, X., Y. Dong, C. Liu, L. Ye, and M. Zhang, 2021. Major challenges and development in Chinese sedimentological research on petroliferous basins. Earth Science Frontiers, 28(1): 1–11 (in Chinese with English abstract).

Figures

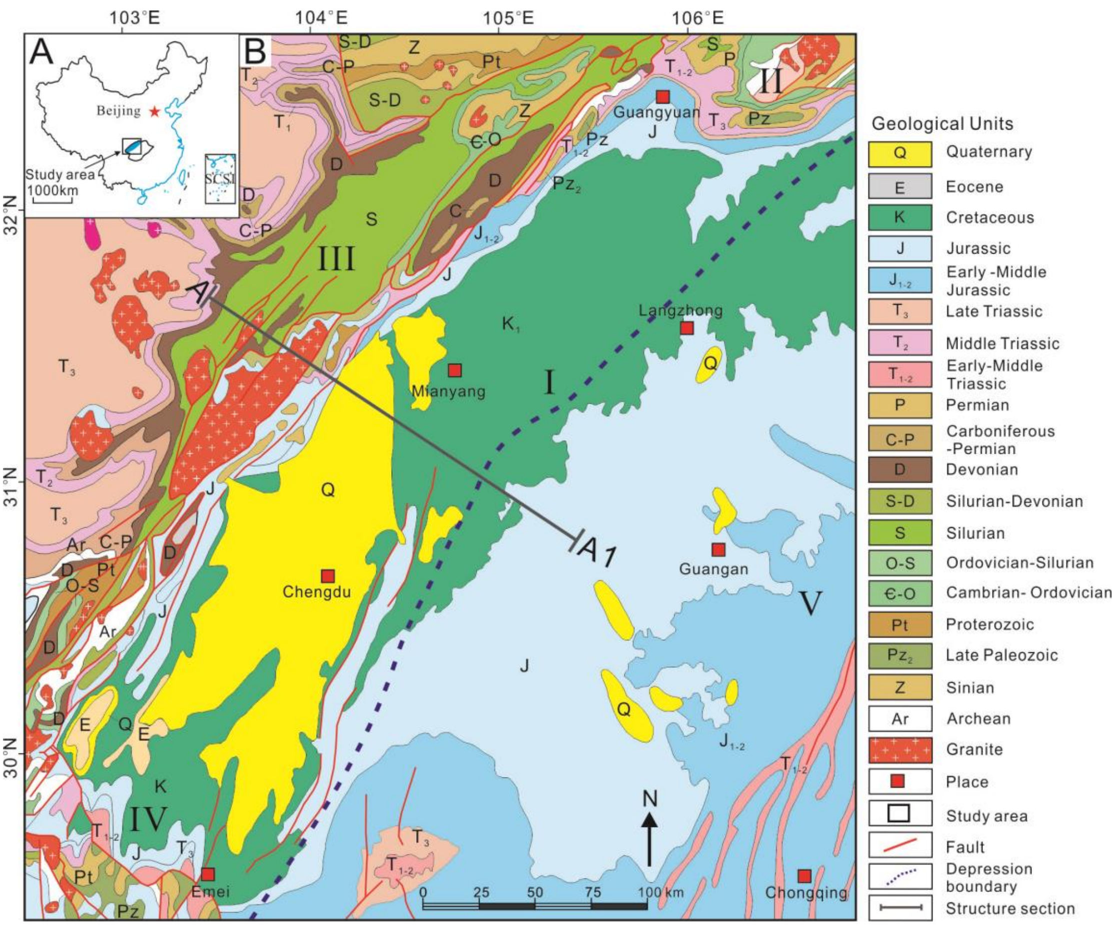

Sun et al., Fig. 1

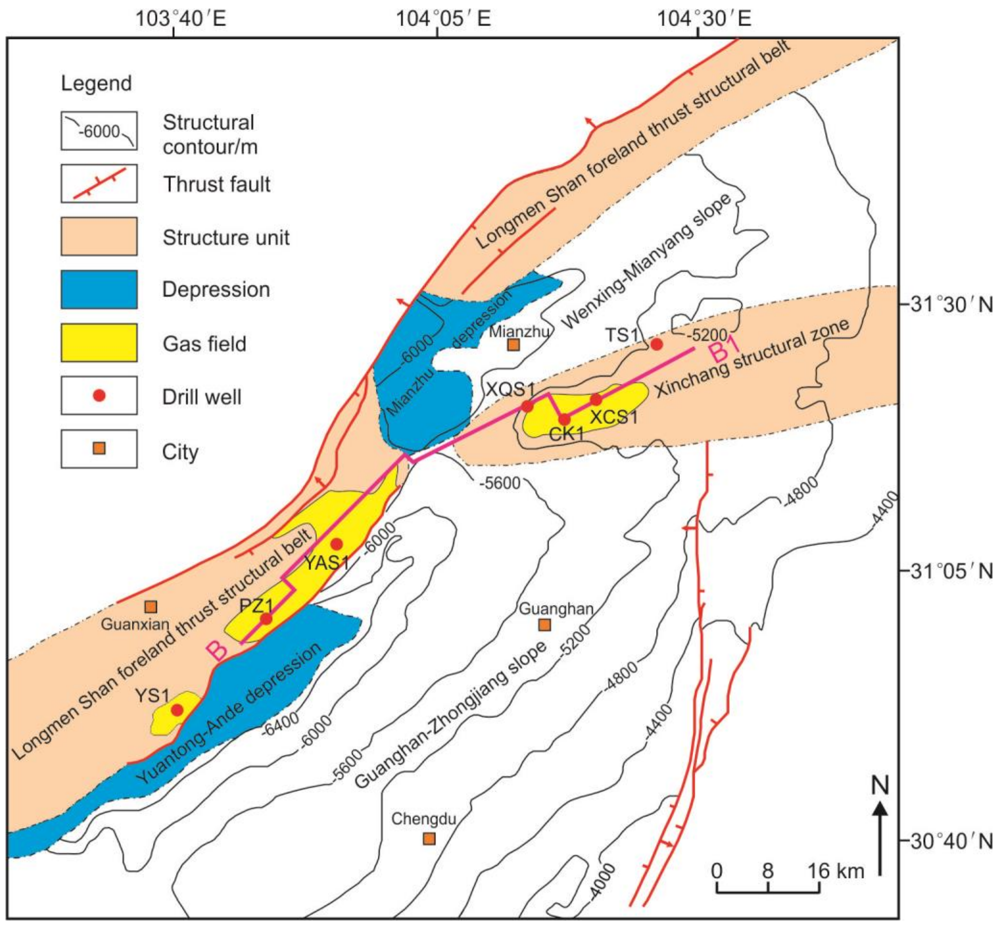

Sun et al., Fig. 2

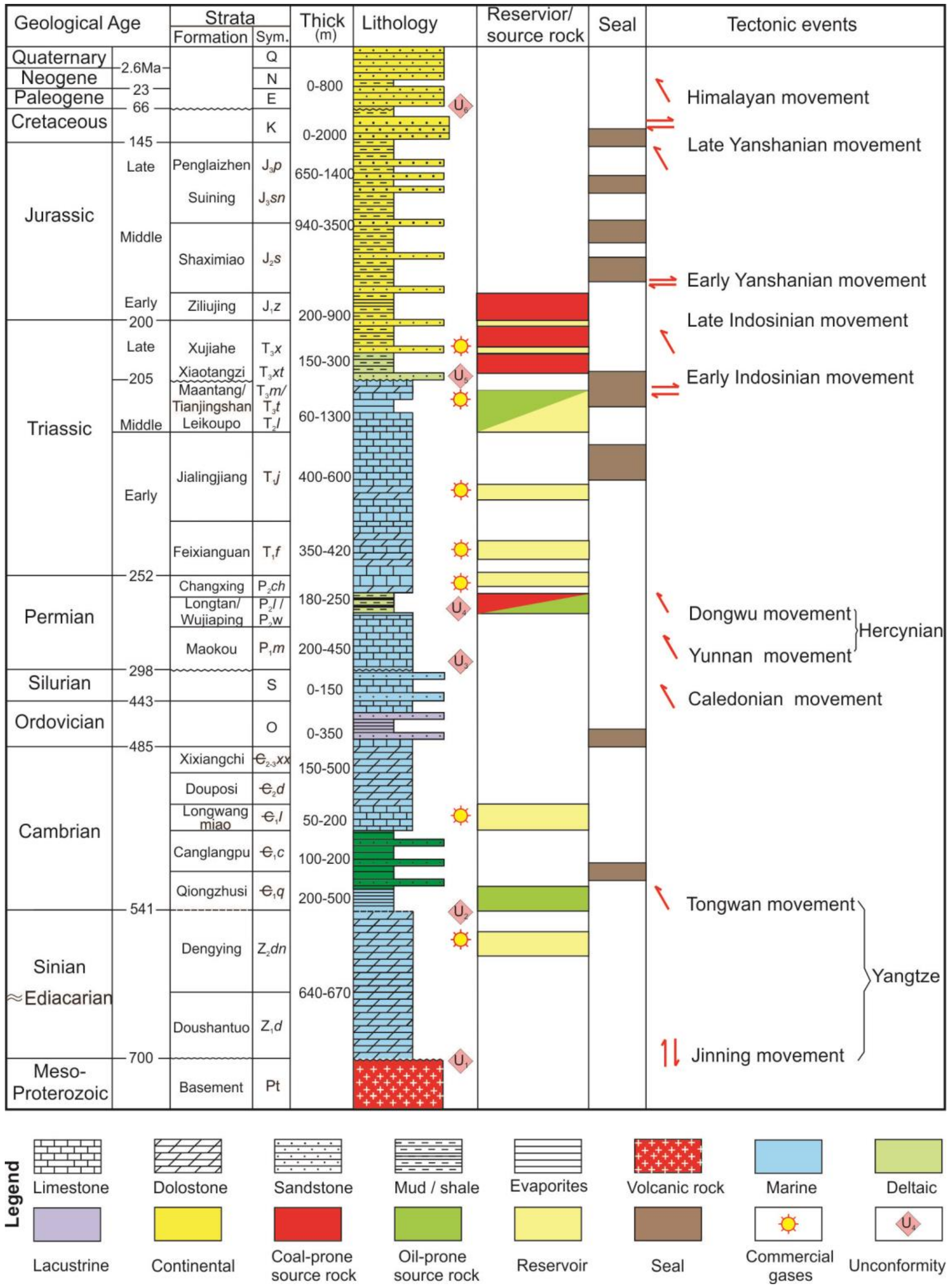

Sun et al., Fig. 3

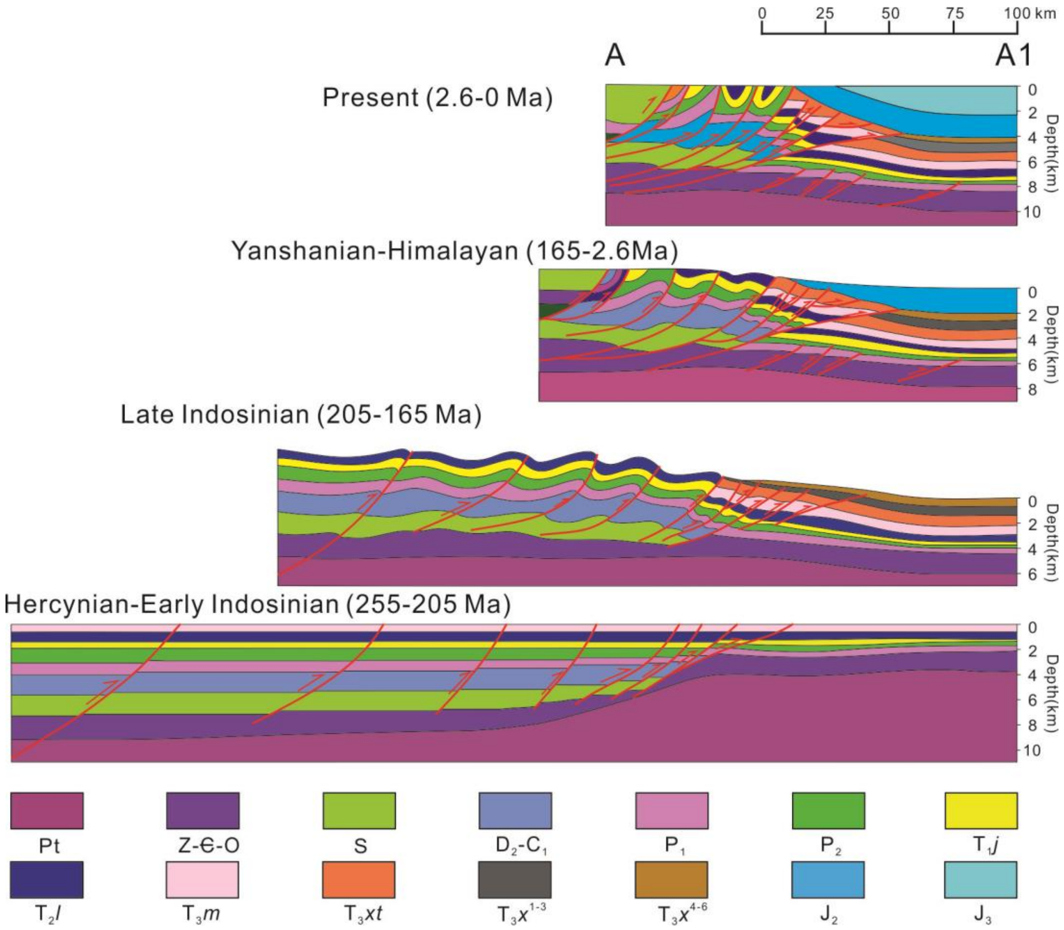

Sun et al., Fig. 4

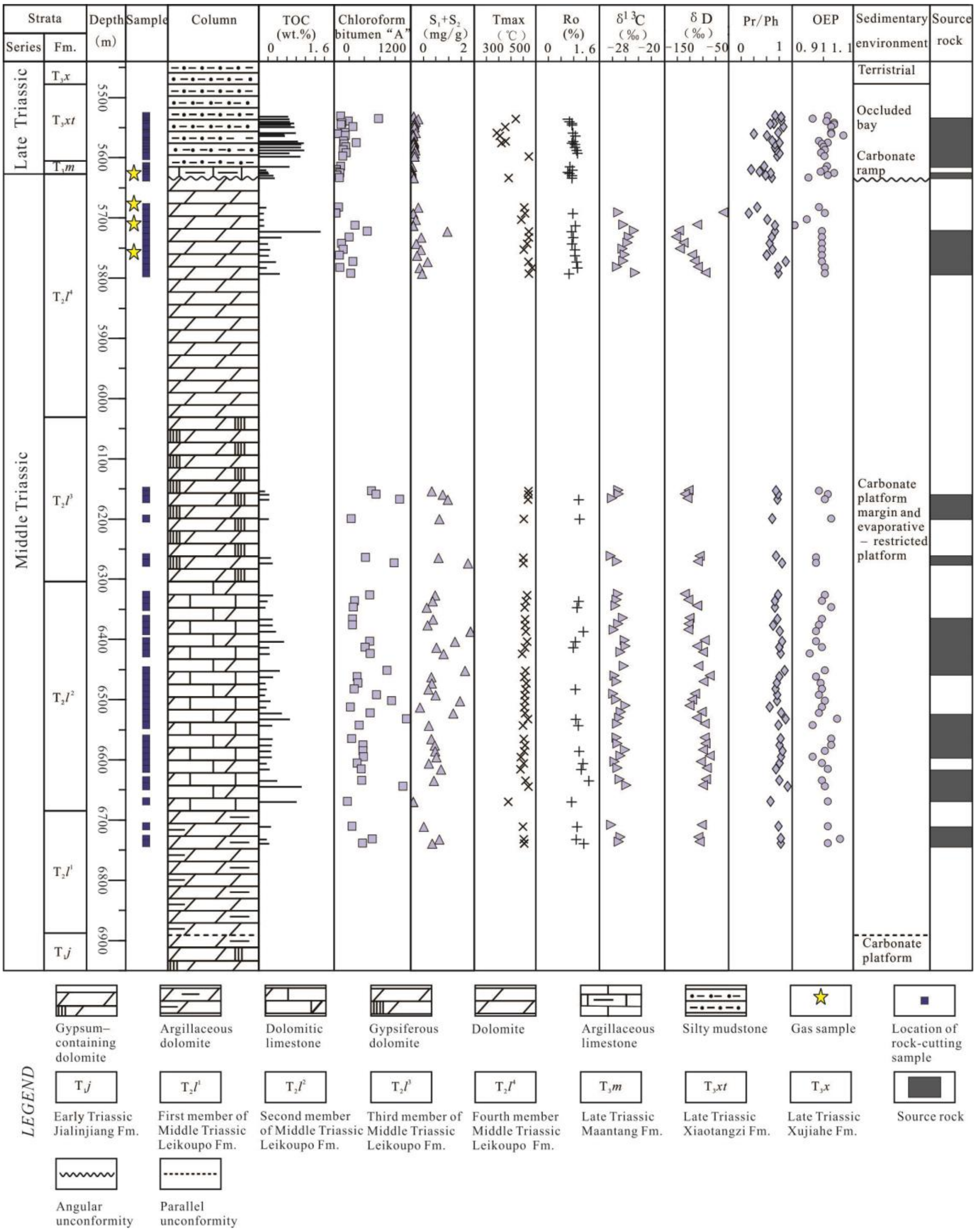

Sun et al., Fig. 5

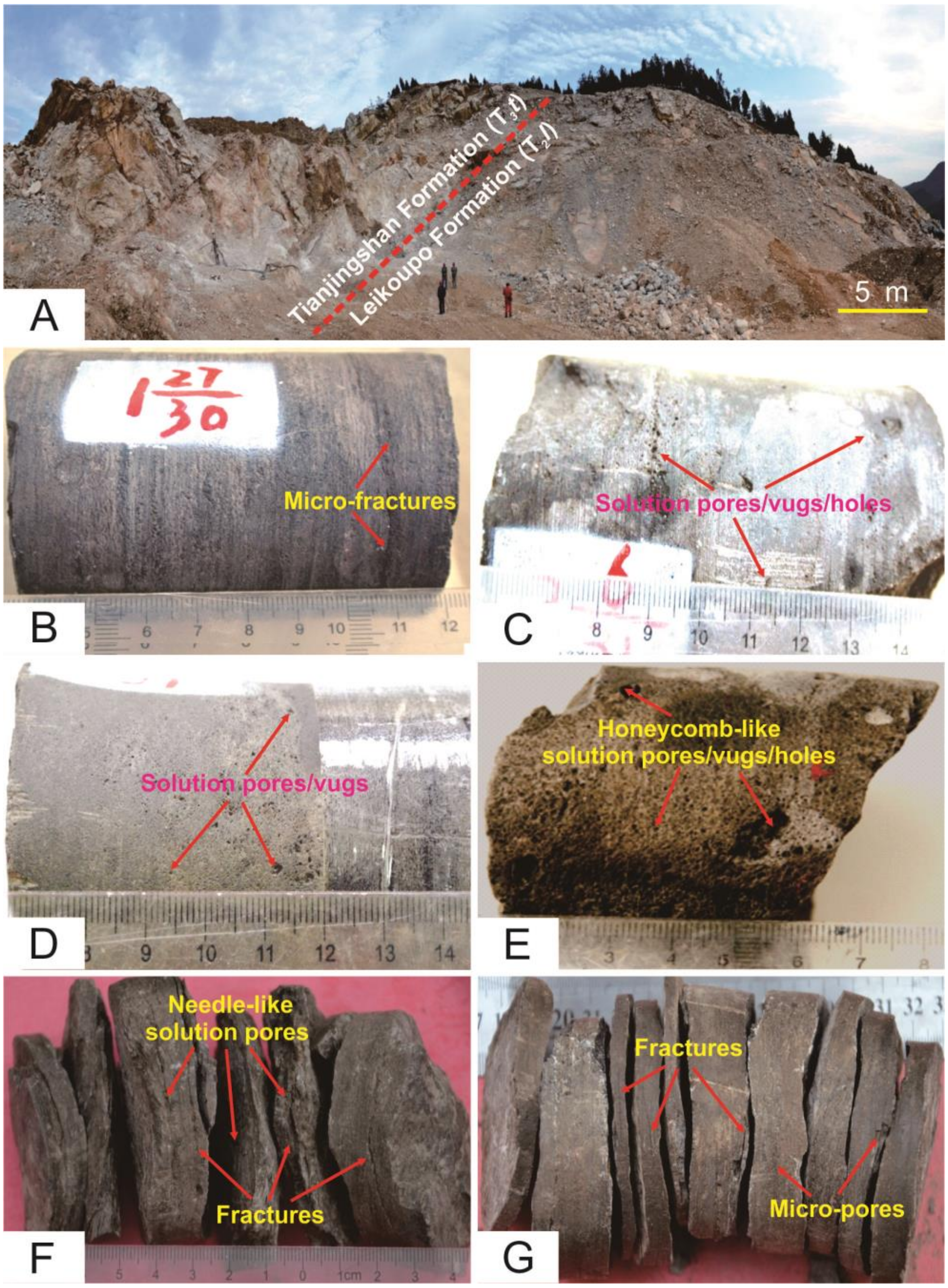

Sun et al., Fig. 6

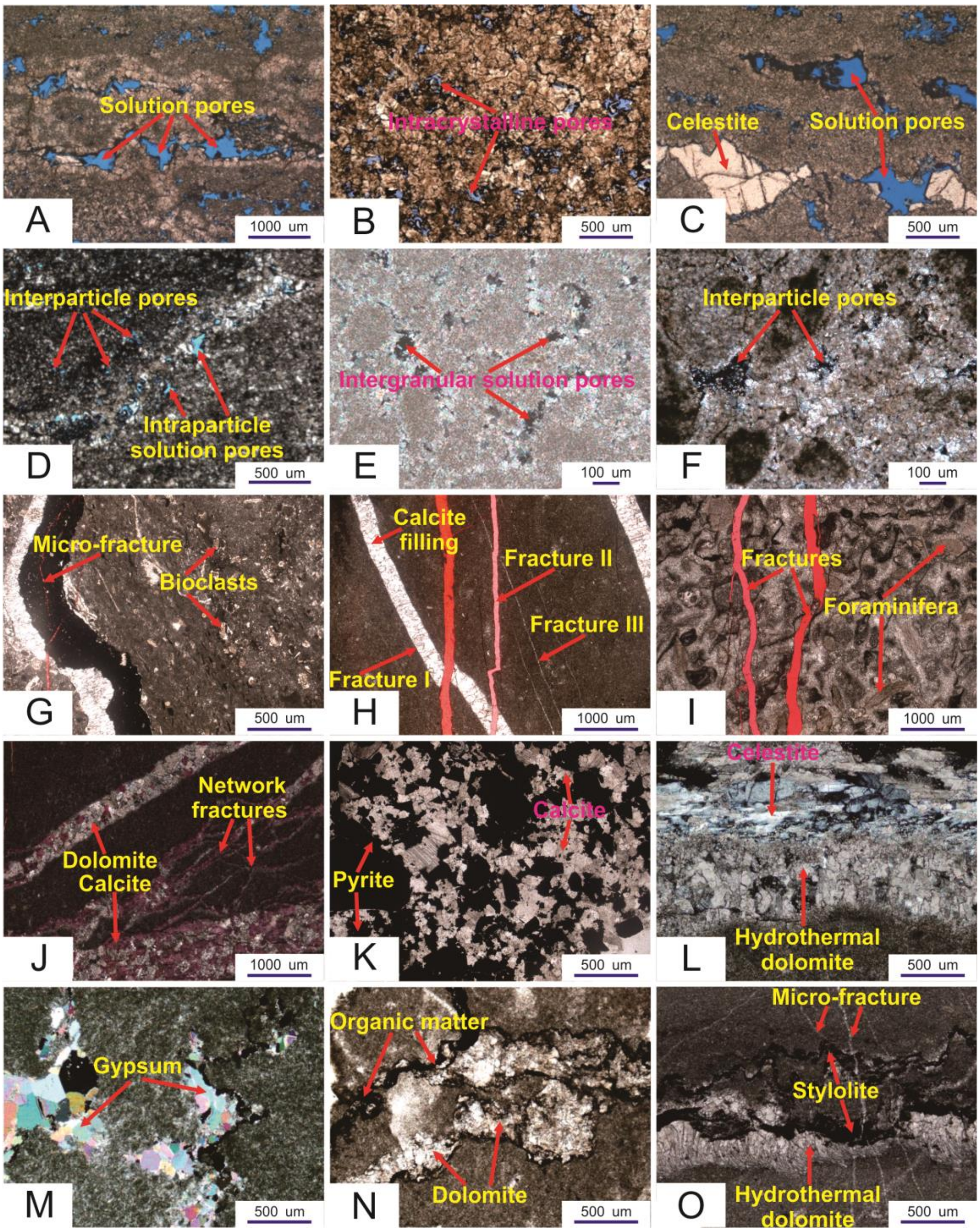

Sun et al., Fig. 7-1

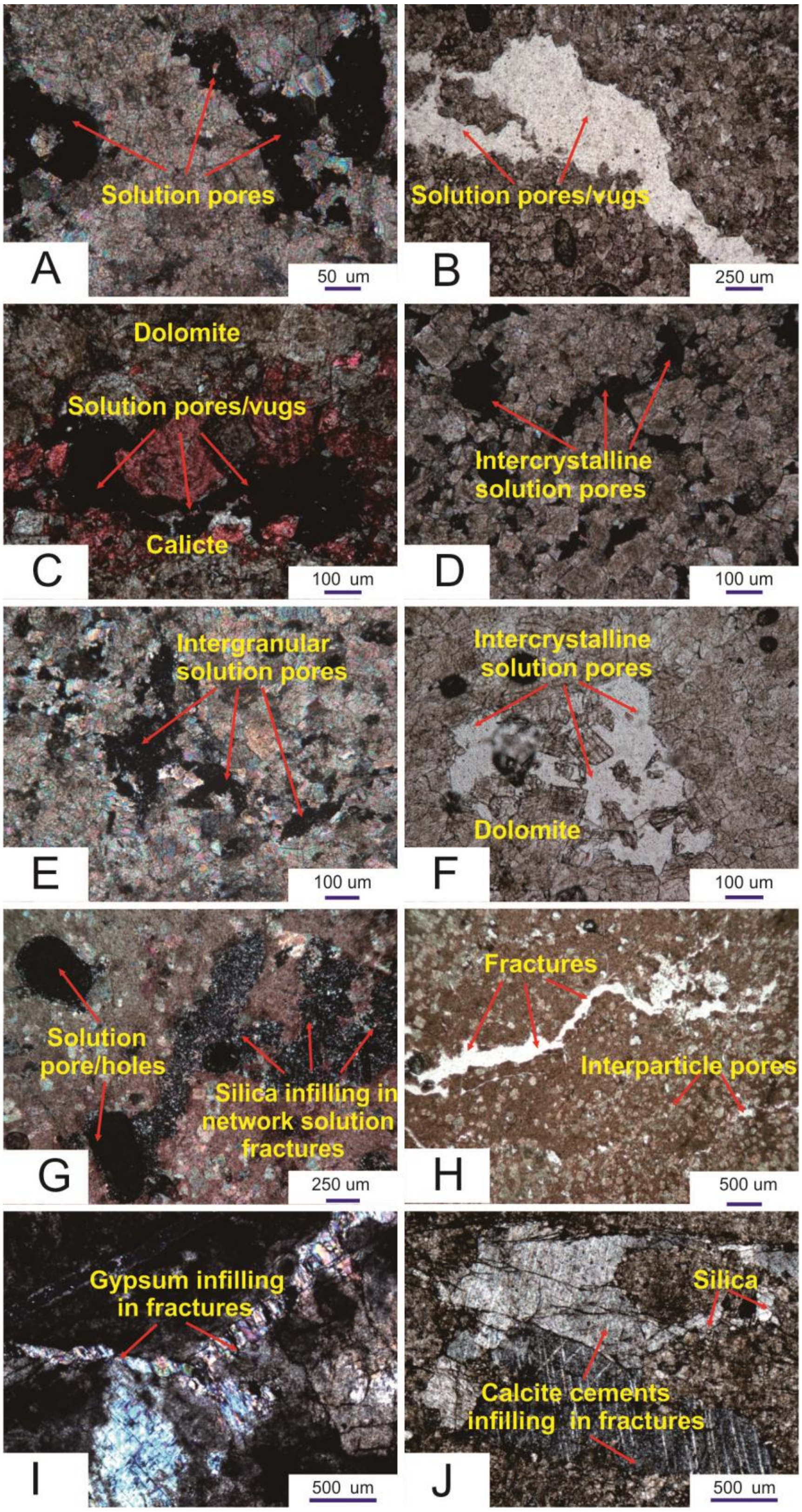

Sun et al., Fig. 7-2

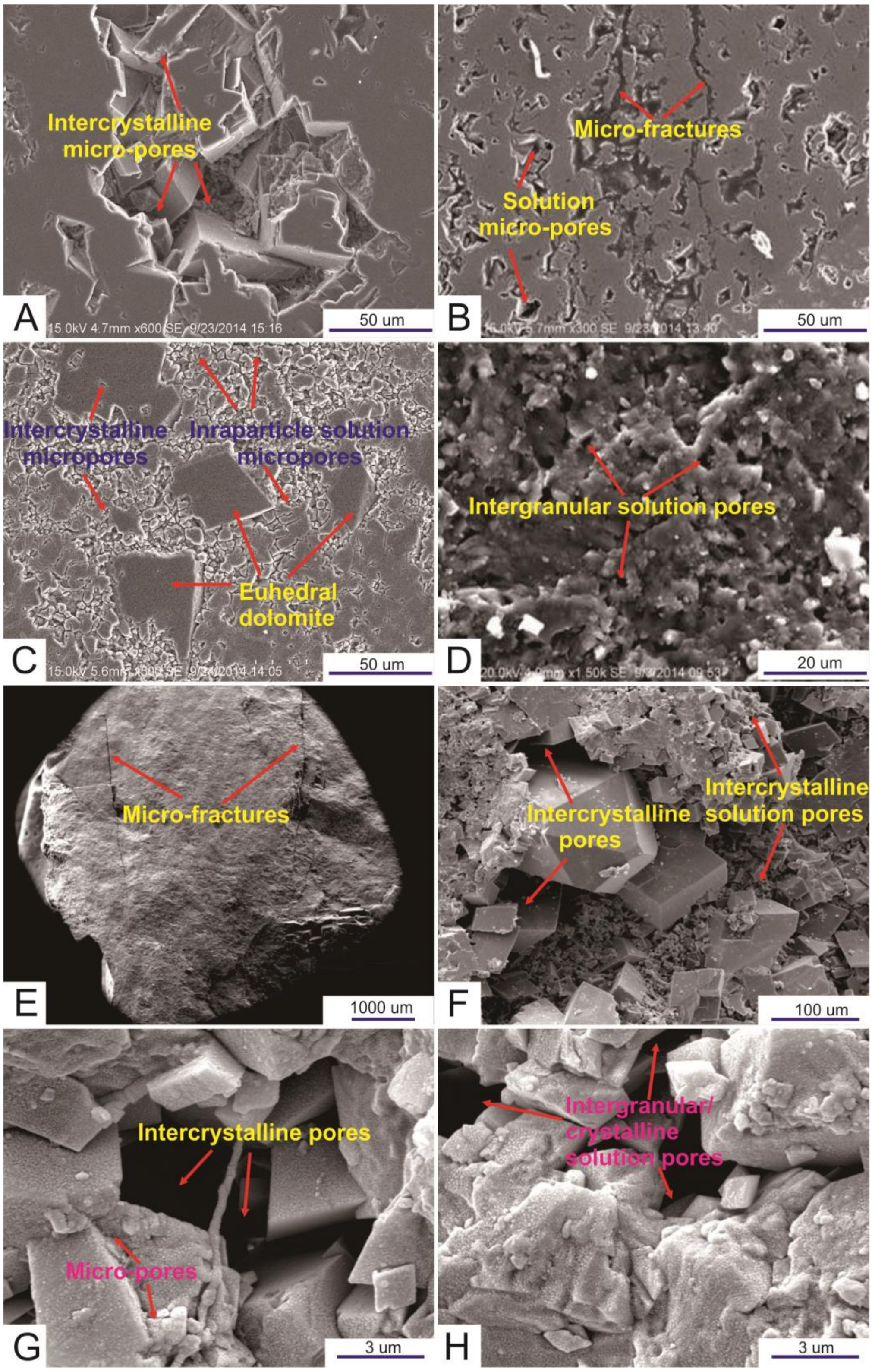

Sun et al., Fig. 8-1

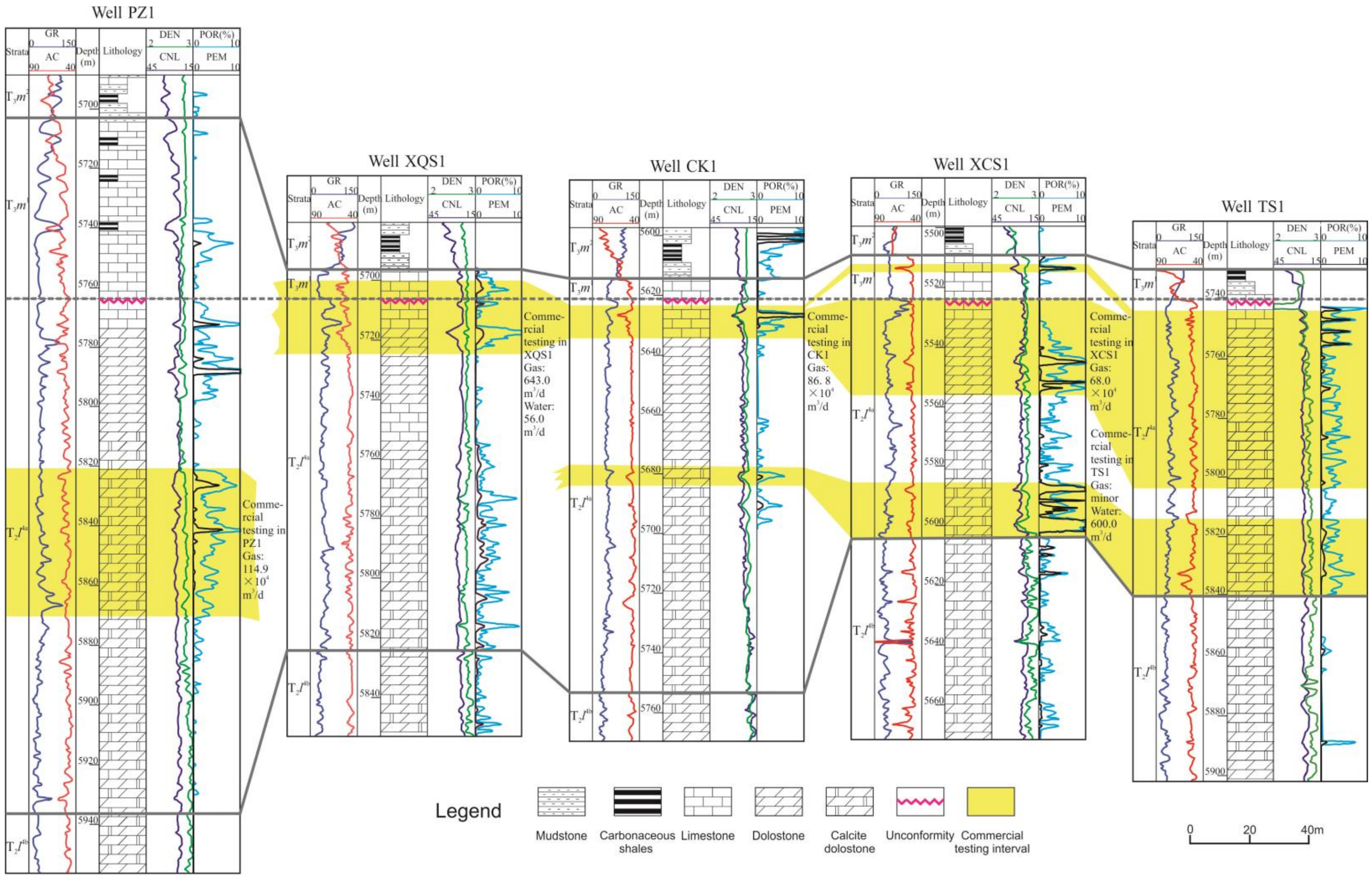

Sun et al., Fig. 8-2

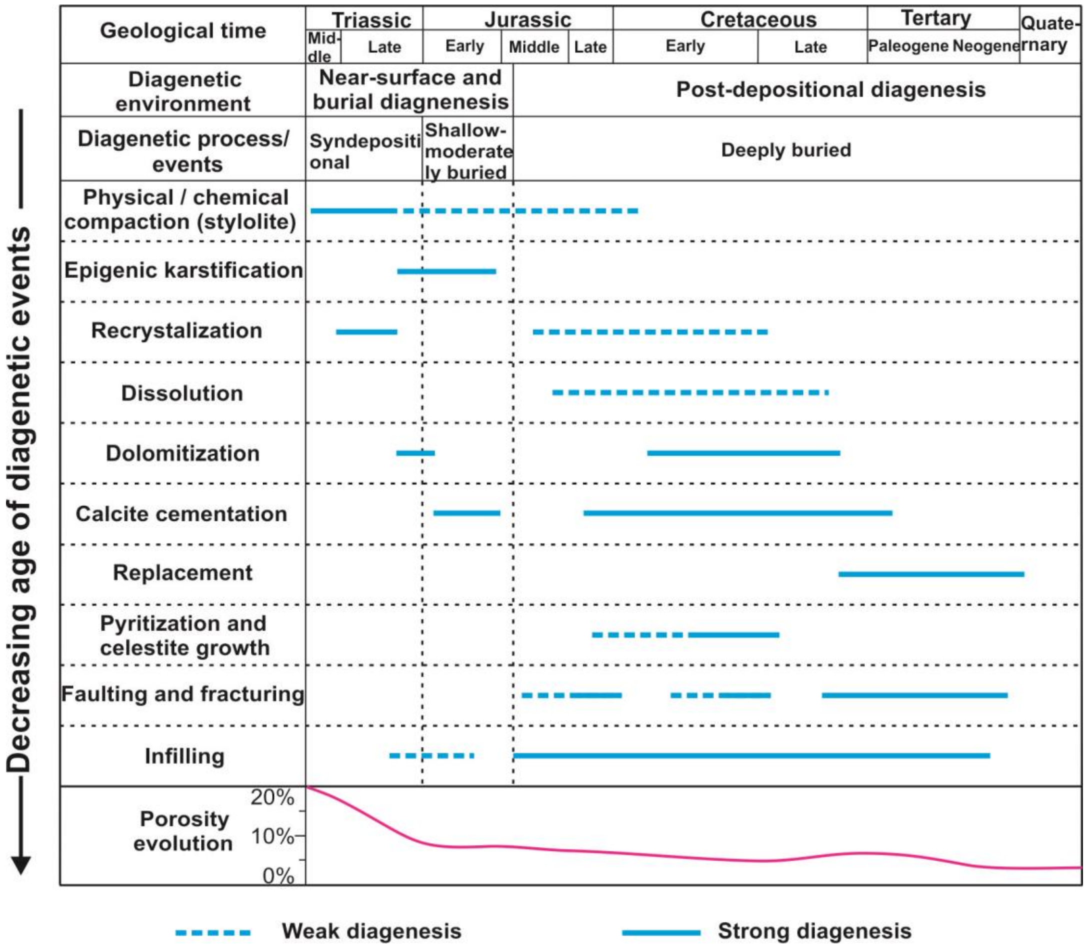

Sun et al., Fig. 9

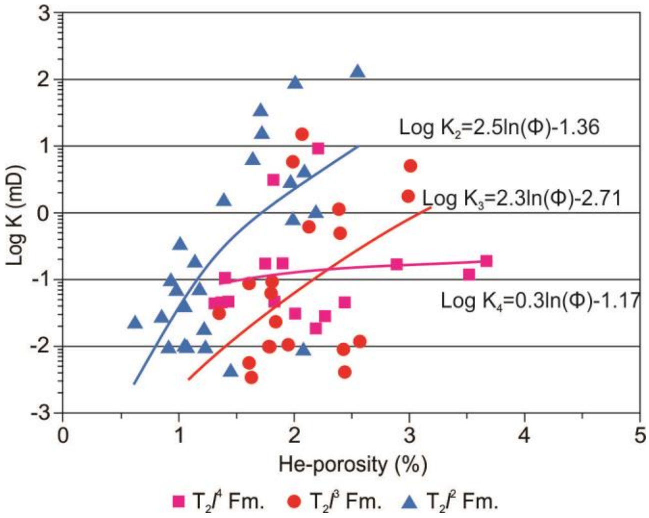

Sun et al., Fig. 10-1

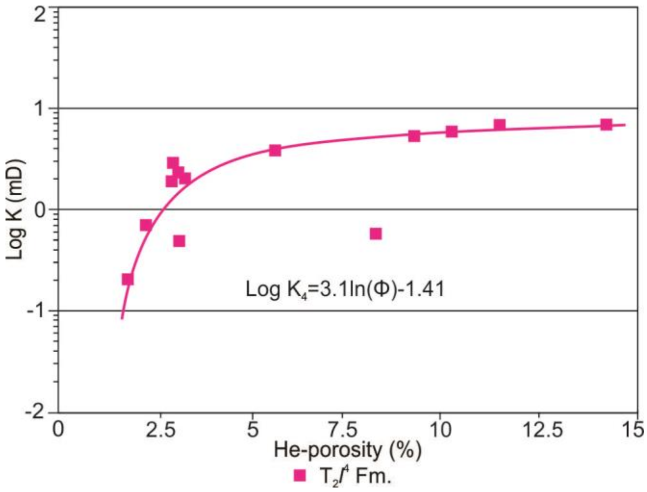

Sun et al., Fig. 10-2

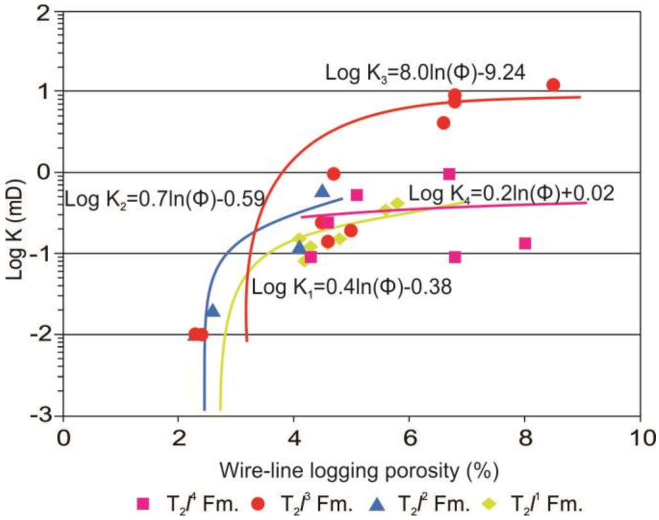

Sun et al., Fig. 10-3

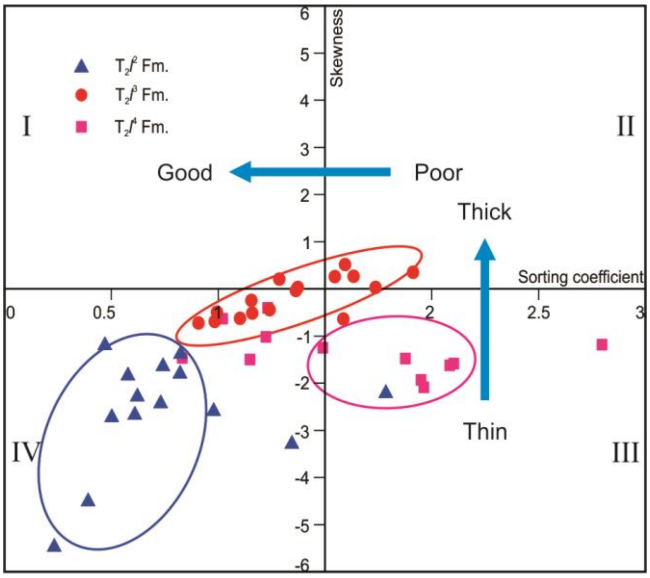

Sun et al., Fig. 11

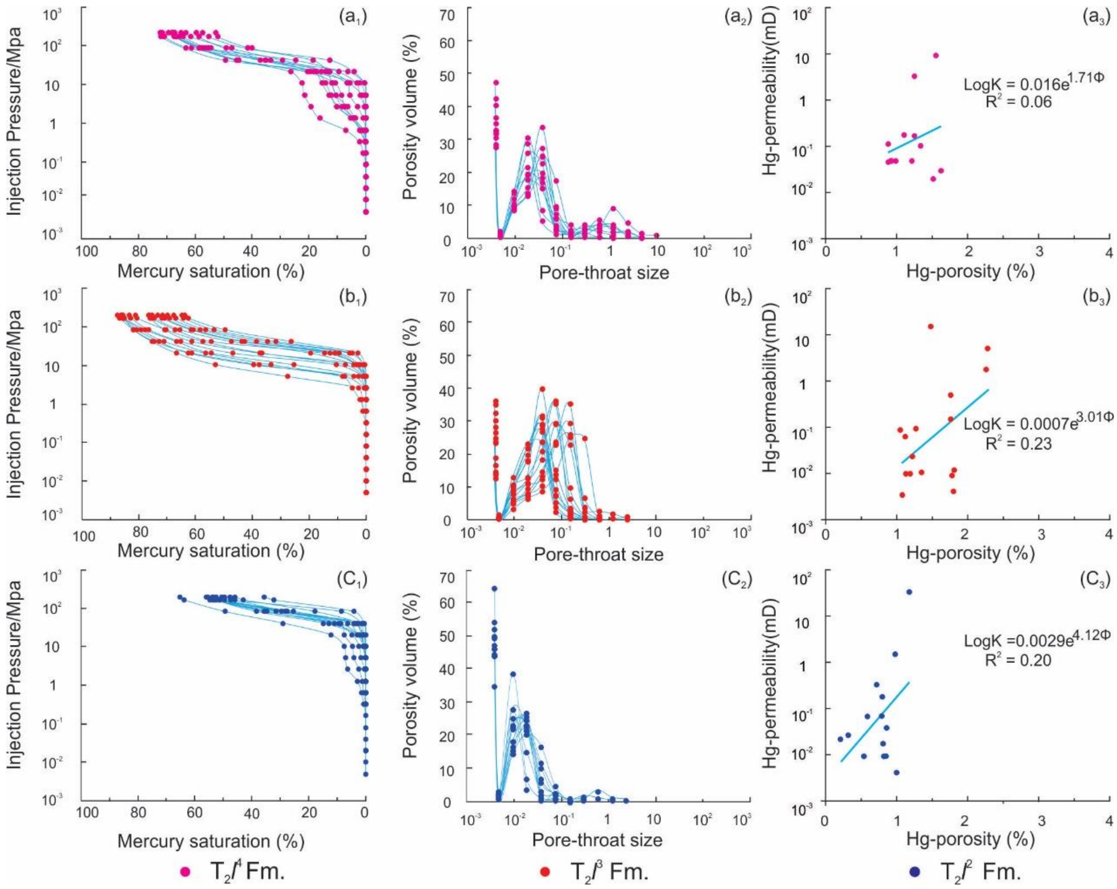

Sun et al., Fig. 12

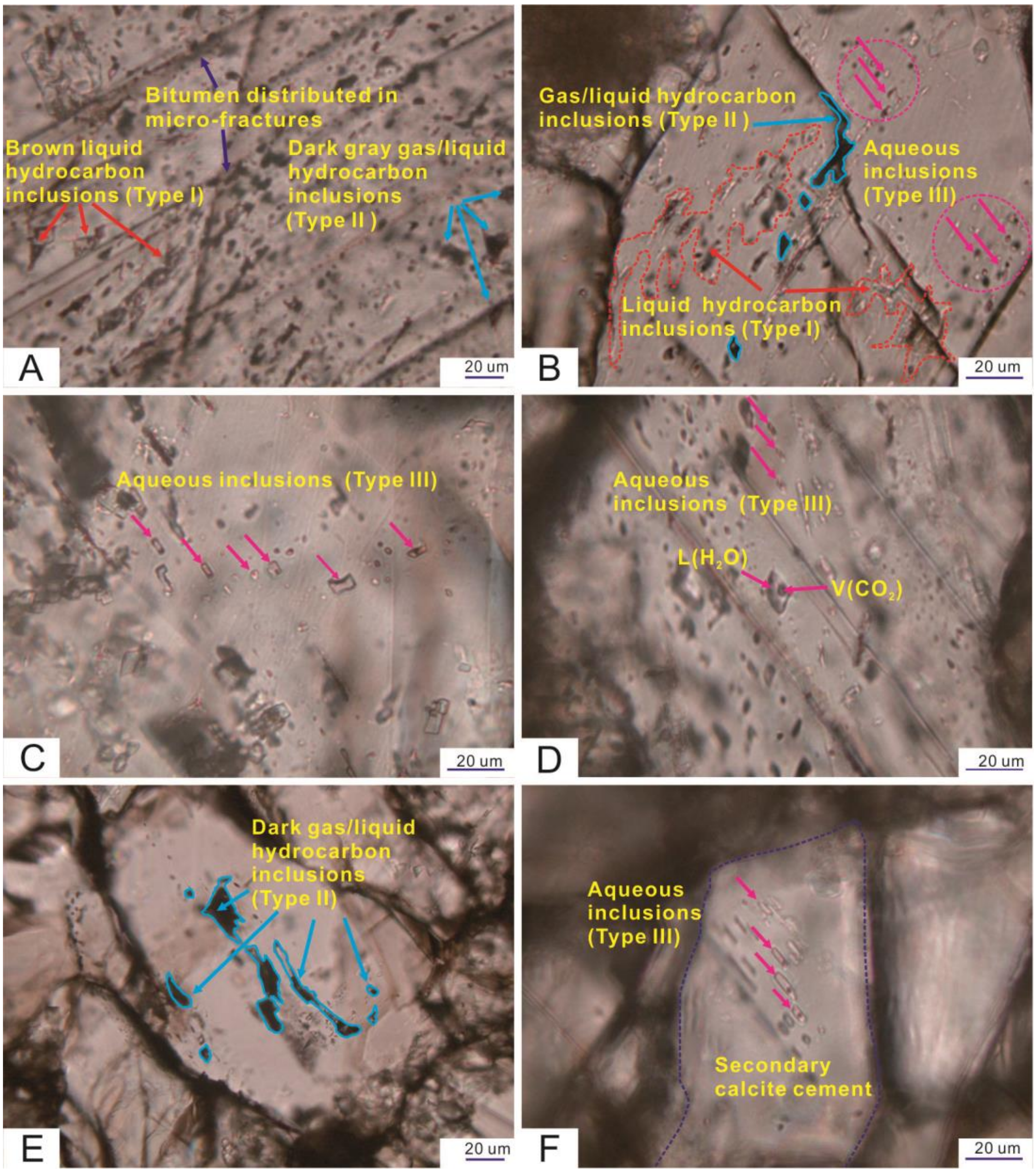

Sun et al., Fig. 13

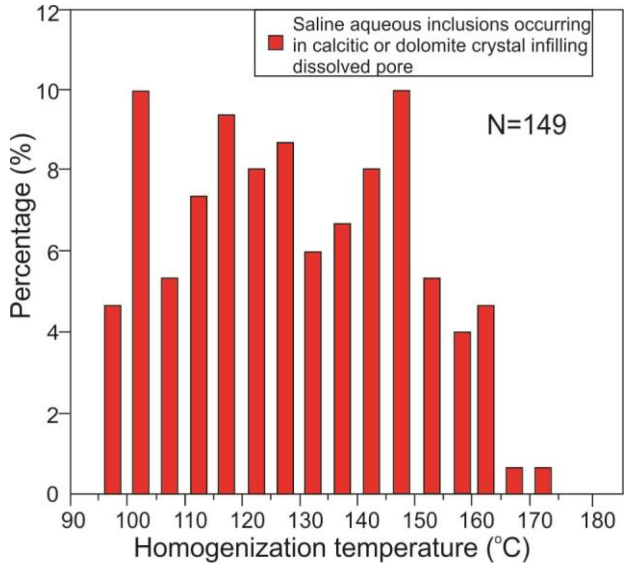

Sun et al., Fig. 14

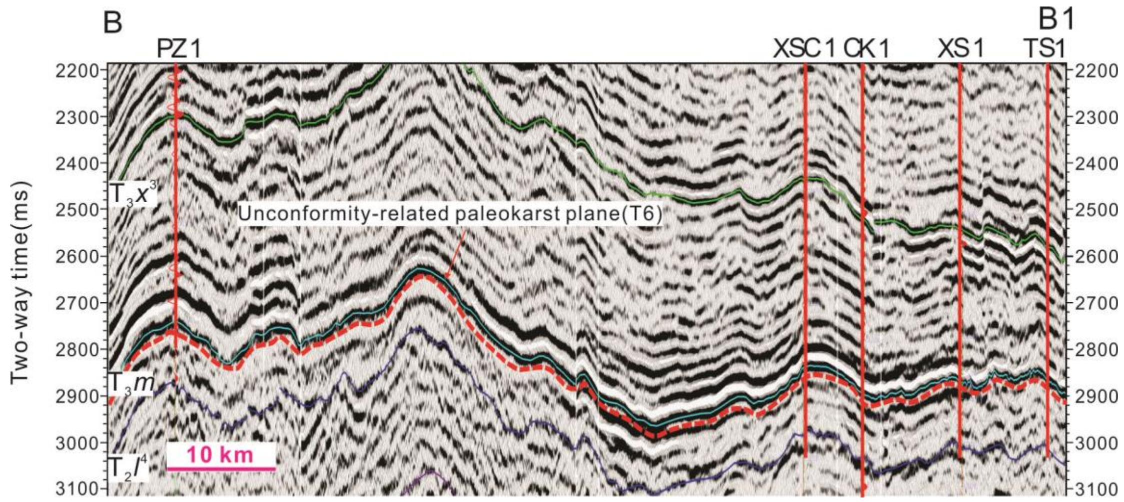

Sun et al., Fig. 15

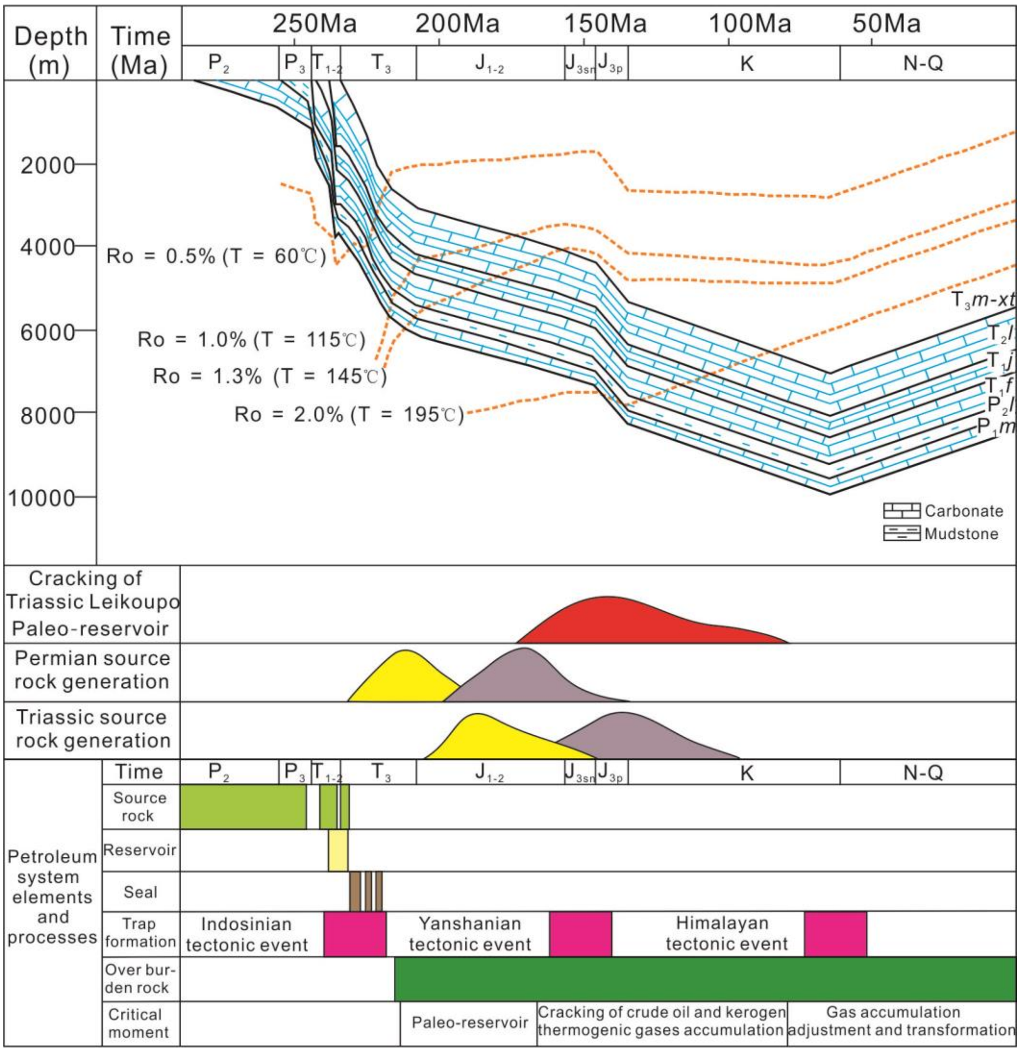

Sun et al., Fig. 16

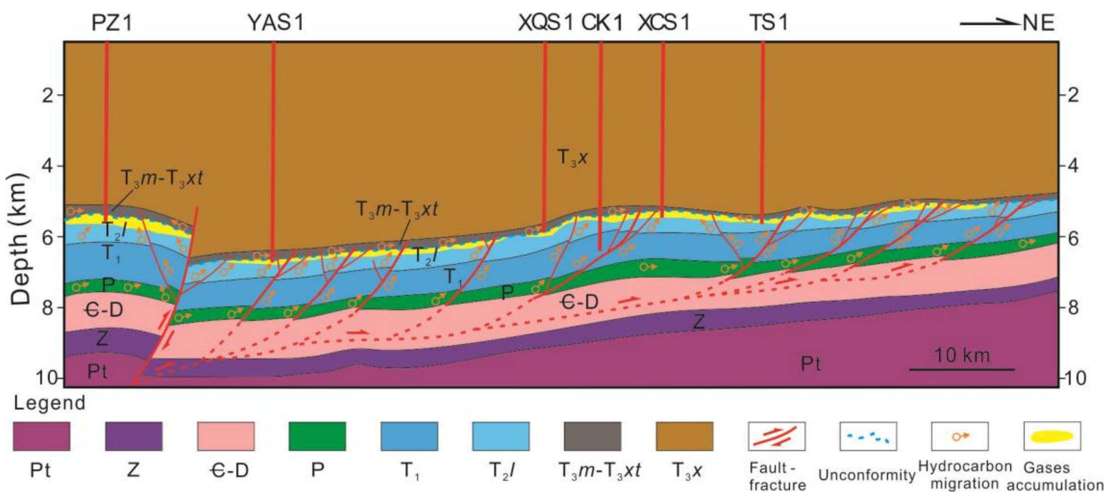

Sun et al., Fig. 17

Table 1 Compilation of source rock parameters used for petroleum system evaluation in the Western Sichuan Depression, China.

Formation	Lithology	TOC (wt. %)	S_1+S_2 (mg/g)	HI (mgHC/gTOC)	Vitrinite reflectance (Ro)	Kerogen Type	Classification	Thickness (m)	References
Longtan/Wujiaping Formation (P_2l/P_2w)	Coal-bearing, bedded shales, dark-gray muddy limestone	0.5–18.37	Carbonaceous mudstone: 15–110 Coal: ~40	Carbonaceous mudstone 36 Coal: ~150	1.0%–3.0%	II–III	Good to excellent	30–120 m in outcrops	Hao et al., 2007; Qin et al., 2016; Guo et al., 2018; Ma et al., 2019
Leikoupo Formation (T_2l)	Gray argillaceous dolomite, gray algal dolomite	(0.21–1.31)/0.29	(0.08–2.50)/0.82	(48.90–296.40)/154.83	1.2%–1.5%	II–III	Fair to good	381–711 m (average: 505 m), 384 m in CK1	Zhang et al., 2007; Qin et al., 2016; Sun et al., 2020
Maantang Formation (T_2m)	Gray limestone	(0.21–0.30)/0.23	(0.03–0.10)/0.05	(10.00–18.10)/12.53	1.0%–1.3%	II–III	Poor to fair	~10 m in well CK1	Sun et al., 2020
Xiaotangzi Formation (T_3xt)	Gray silty shale, gray and black shale, siltstone, dark-gray shale	(0.53–0.95)/0.76	(0.04–0.25)/0.12	(4.68–20.31)/11.08	1.2%–1.3%	III	Moderate	~82 m in well CK1	Ye, 2003; Shen et al., 2008; Sun et al., 2020

Table 2 Criteria used to evaluate marine carbonate reservoir quality of the Sichuan Basin, China (Cited from Chen et al., 2013; Li et al., 2015)

Reservoir type (class)	I	II	III	IV
Porosity (%)	≥12	12–6	6–2	＜2
Permeability (mD)	≥1.0	1.00–0.25	0.250–0.002	＜0.002
Median throat width (μm)	≥1	1.0–0.2	0.200–0.024	＜0.024
Pore structure type	Macropore-large throat	Macropore-medium coarse throat	Medium pore-fine throat	Micropore-micro-throat
		Medium pore-medium coarse throat	Fine pore-fine throat	
Reservoir evaluation	Good to excellent	Medium to good	Poor	Bad

Table 3 Comprehensive evaluation of qualitative and quantitative reservoir characteristics of the Middle Triassic Leikoupo Formation (T_2l) in the Western Sichuan Depression, China

Formation	Drilling core petrographic descriptions	Pore space	Porosity and permeability (measured by helium)	Porosity and permeability (interpreted by well-logs)	Thickness (m)	Diagenetic phenomena	Quality evaluation	Wells	Data source
Uppermost fourth member of the Leikoupo Formation (unconformity-related paleo-karstification zone, T_2l^{4a})	Brecciaed dolostone, gray micritic limestone, dark-gray dolomite, gypsum and dolomitization, Fractures with muddy infilling	Solution-enhanced pores, holes, vugs and fractures, micropores	1.8%–14.2%, 0.2–7.7 mD (drilling core)	None	10–200 m	Epigenetic karstification and solution	Medium to excellent (Type I–II)	PZ1, YS1, XCS1 CK1, TS1	This study
Lower fourth member of the Leikoupo Formation (further below the unconformity, T_2l^{4b})	Gray calcarenite packstone, dark-gray to gray micritic limestone, dark-gray calcareous dolomite, dark-gray microcrystalline dolomicrite, and white gypsum beds. Sandy, finely crystalline dolomite, allochemical dolomite, micro-algal dolomite with ostracodes, microcrystalline dolomite containing celestite veins	Solution pores, intercrystalline pores, intercrystalline solution pores, intergranular solution pores, interparticle, intraparticle solution pores, microfractures, micropores	1.2%–2.5%, 0.02–9.2 mD (core plug)	6%–10.5%, 0.1–0.8 mD	~30 m	Epigenetic karstification, infilling, partial filling with celestite and solution	Medium to excellent (Type I–II)	PZ1 YS1, XQS1, CK1, XCS1	This study
Third member of the Leikoupo Formation (T_2l^3)	Thrombolitic dolomite, stromatolitic dolomite, finely crystalline and sand-bearing dolomite, and microcrystalline gypsum-bearing dolomite. Dolomicrite and	Intercrystalline pores, stylolites, and open fractures, interparticle and intraparticle solution pores, micropores	1.4%–4.1%, 0.003–15.0 mD (core plug)	4.7%–8.5%, 1.0–12.0 mD	~90 m	Calcite cementation, chemical compaction, and	Medium to excellent (Type	CK1	This study

	calcite veins occurring abundantly.					dolomitization	I−II)		
Second member of the Leikoupo Formation （T_2l^2）	Fine-grained argillaceous limestone, muddy micritic limestone, crystalline packstone, and fine to coarsely crystalline ferruginous limestone. Calcite grain size is uniform, generally between 0.02 and 0.03 mm, with a dense, intergranular mosaic. Higher mud content with a uniform distribution, a few ostracodes and pyrite crystals are distributed throughout. Average crystal diameter ranges from 0.3 mm to 0.6 mm (maximum 1.5 mm), and most are rectangular	Stylolites, micropores, and two types of macro-fractures. Fracture Type I are filled with calcite and range in width from 0.1 mm to 0.25 mm; Fractures Type II are unfilled and are interwoven with Fracture Type I, Fracture II widths range from 0.04 mm to 0.35 mm; the micro-cracks form an effective fracture network system	0.6%–2.6 %, 0.004–125.2 mD (core plug)	2.3%–8.5%, 0.04–12.0 mD	~30 m	Recrystallization, pressure-solution, pyritization, faulting, and fracturing	Medium to good (Type II)	CK1	This study
First member of the Leikoupo Formation （T_2l^1）	Argillaceous dolomite, microcrystalline to finely crystalline dolomite, and medium to coarsely crystalline saddle dolomite. Allochems are mainly bioclastic with a uniform distribution. Allochem size is uniform, with a particle size of <0.1 mm. Calcite grains are amorphous and small, generally <0.02 mm to 0.03 mm for micrite	Fractures with widths ranging from 0.01 mm to 0.02 mm; solution pores are less common, micropores	None	4.3%–8.0%, 0.09–0.95 mD	~40 m	Celestite, pyritization and hydrothermal dolomitization	Poor to good (Type II−III)	CK1	This study